FROM DYNAMICS TO STEADY STATE: COMPUTING AND PROBING PLASMONIC HOT CARRIERS

A Dissertation

by

SHENGXIANG WU

Submitted to the Office of Graduate and Professional Studies of
Texas A&M University
in partial fulfillment of the requirements for the degree of

DOCTOR OF PHILOSOPHY

Chair of Committee,	Matthew Sheldon
Committee Members,	Dong Hee Son
	Sarbajit Banerjee
	Alexey Belyanin
Head of Department,	Simon North

December 2020

Major Subject: Chemistry

ABSTRACT

The collective oscillation of conduction band electrons in metal nanostructures, known as the localized surface plasmon resonance (LSPR), can be engineered to absorb photons at desired wavelength. Plasmonic nanostructures have received significant research interests not only because this flexible optical response tailorability, but also because the hot carriers excited within plasmonic metals after the non-radiative decay of LSPR have remarkable photocatalytic performance. Therefore, the dynamics of hot carriers and the behavior of hot carriers at steady state are of great interest in the field of photodetection, photocatalysis and optical power conversion devices.

In this dissertation, my study is divided into three distinct yet connected projects. In the first project, a free-electron jellium model is used to calculate the energy distribution of non-thermal carriers. Additionally, a theoretical framework describing tunneling phenomena of carriers in a metal is derived. With the electric field provided by the full-wave optical simulation (FDTD method), an asymmetric plasmonic tunnel junction is proposed and a 20% output energy efficiency is calculated. The second project studies the Raman scattering from plasmonic metals, in which a two-temperature anti-Stokes Raman thermometry is developed. Within this thermometry, not only the material temperature but also a subpopulation of hot carriers with energy distribution described by a second temperature, electronic temperature, is accurately probed. Furthermore, we proposed that the inelastic scattering from non-thermal carriers contributes in the Stokes Raman scattering. A good agreement between theory and experiment is achieved and the plasmon dephasing time, which dictates the decay of LSPR, is extracted from steady state measurement. To prove the presence of hot carriers at steady state, an independent thermionic emission experiment is conducted in the third project. Patterned gold nanostructures are fabricated using electron-beam lithography, and a thermionic emission device consists of gold nanostructures and an ITO electrode is constructed. The current-voltage characteristics not only proves the presence of hot carriers but also tells the information about the size and energy distribution of hot carriers.

The study of hot carriers at steady state is crucial in designing hot carrier devices with bet-

ter performance. The results and analyses presented in this dissertation shall provide insightful perspective of hot carrier behavior at steady state and broaden the horizon of hot-carrier-mediated photocatalysis and light-harvesting applications.

DEDICATION

Pain is temporary. Quitting last forever.

ACKNOWLEDGMENTS

First and foremost I thank my research adviser, Dr. Matthew Sheldon, for supporting my idyllic lifestyle as a graduate student in Texas A&M University. The first time we Skype chatted , I was impressed by his motivation towards science. His generosity sharing scientific perspective, professional contacts have been an immeasurable aid in my scientific development. His great personalities, such as patience, strictness, kindness and humor, deeply influenced me and his smartness and broad knowledge let me learn a lot after five years working with him.

I also thank my committee members Dr. Dong Hee Son, Dr. Sarbajit Banerjee, and Dr. Alexey Belyanin for their time. I have always get help from Dr. Son and members from his lab, from chemicals to instruments. His knowledge in LabVIEW automation truly impressed me.

I thank Dr. Alejandro Manjavacas, Dr. Gururaj Naik for fruitful discussion. When I was stuck on the derivation of the perturbation theory as in my second year, they provided remarkable perspective and walked me through the theory.

I thank all of my past and present group members with a special thanks to Dr. Nicki Hogan, Dr. Athavan Nadarajah, Jarett Martin, Dr. A. Ryan Kutayiah, Benjamin Roman, Maelani Negrito, Hsu-Cheng (Oscar) Cheng, Je-Ruei (Ray) Wen, Freddy A. Rodriguez Ortiz, Rivi Ratnaweera, Noel Mireles, Zachary Brawley, Smriti Kumar, Kylie Lytle, Annika Lee and Boqin (Justin) Zhao. I enjoy collaborating with them and get lots of knowledge from them.

A special thank to my fiancée, Zhuotong Liu. You are the world's most wonderful girl, you have no idea how happy you make me. Thank you for loving me, and thank you for making me feel so loved.

I thank my comrades in 'the Pantheon NB': Nacericky, Julia, Kakarot, Guichuideng, Mangguo, Lina, Dalian Hank. ... The days we fight together will last forever in my memory. For the Alliance!

I thank my family, who support me during my hard time. Thank you for always being there to support me. I will forever be grateful.

CONTRIBUTORS AND FUNDING SOURCES

Contributors

This work was supervised by a dissertation committee consisting of Professor Matthew Sheldon, Professor Dong Hee Son, and Professor Sarbajit Banerjee of the Department of Chemistry, and Professor Alexey Belyanin of the Department of Physics. The electron beam lithography was performed by Dr. Nicki Hogan of the Department of Chemistry.

All other work conducted for the dissertation was completed by the student independently.

Funding Sources

This work is funded by the Air Force Office of Scientific Research under award number FA9550-16-1-0154.

NOMENCLATURE

LSPR	Localized Surface Plasmon Resonance
CID	Chemical Interface Damping
CW	Continuous Wave
NP	Nanoparticle
TTM	Two-Temperature Model
DOS	Density of States
QY	Quantum Yield
PETE	Photon-Enhanced Thermionic Emission
ω_{p}	Plasma Frequency
γ_{b}	Bulk Damping Rate
l	Mean Free Path
v_{F}	Fermi Velocity
n	Electron Density
ε	Permittivity
ε_0	Vacuum Permittivity
m	Electron Mass
$\varepsilon^{\mathrm{ib}}$	Interband Contribution
C_{e}	Electronic Heat Capacity
C_{l}	Lattice Heat Capacity
T_{e}	Electronic Temperature
T_{l}	Lattice Temperature
χ	Hot Carrier Population

g	Electron-Phonon Coupling Constant
h	Planck's Constant
$\hbar$	Reduced Planck's Constant $\hbar = \frac{h}{2\pi}$
U	Potential Barrier Height
J	Current Density
J_{sc}	Short-Circuit Current Density
V_{oc}	Open-Circuit Current Density
$\mathrm{S}(\Delta\omega)$	Spectral Intensity
k_{B}	Boltzmann Constant
$\mathrm{D}(\Delta\omega)$	Density of Optical States
$J(\hbar\omega)$	Joint Density of States
ϕ	Work Function
E_{F}	Fermi Energy

TABLE OF CONTENTS

Page

LIST OF FIGURES

FIGURE Page

1. INTRODUCTION

1.1 Overview

Similar but not the same as plasma in space, plasmon is collective movement of electrons inside metallic particles. The excitation of a localized surface plasmon resonance (LSPR) occurs when incident electromagnetic radiation couples to the coherent oscillation of conduction electrons in a nanostructured metal.[1] Because of its exceptional ability to couple far-field radiation and concentrate into sub-wavelength volumes well below the diffraction limit,[17] and produce strong near-fields which result in extreme electrical field enhancements,[18] plasmon is becoming an essential element in nanophotonics. These excellent properties boost the novel applications including ultrasensitive sensing,[19–21] photothermal cancer therapy[22,23] and improved photovoltaic devices.[24]

The lifetime of the coherent LSPR oscillation is very short, on the order of femtoseconds.[25] LSPR oscillations dephase (decay) either radiatively, observed as photon scattering, or nonradiatively, observed as photon absorption.[26,27] Recently, it has been proposed that the creation of a chemical interface (i.e., chemical bonds between the metal surface and another species) also influences the optical properties of plasmonic nanoparticles, which has been referred as chemical interface damping (CID).[28–33] The electronic states associated with the interfacial bonds can be involved in the coherent LSPR oscillation and decrease the coherent LSPR lifetime.[34–37] The dominant LSPR dephasing pathway is sensitive to the composition, size, geometry and environment of the metal nanostructure.

The radiative decay channel was extensively utilized in the past years for optimization, and has been explicitly explored for improved photovoltaic devices.[24] Recently, a lot of research efforts have been made to explore the hot carriers generated through the nonradiative decay in many experiments.[3,38] Through nonradiative decay channel, the LSPR decayed into excited electrons or holes. In the situation where the energy difference between the excited electrons or holes and the Fermi level is larger than the energy of the relevant thermal excitation, these carriers are referred to as

hot electrons or holes. These hot carriers can be used to induce chemical reactions on the surfaces of plasmonic nanostructures which will otherwise be very energetically demanding.[39] Various experiments including hydrogen dissociation,[40,41] water splitting[42–45] and ammonia decomposition[46] have been demonstrated, thus boost the growth of this new area of plasmon-mediated photocatalysis.[47,48] Not only hot carrier through non-radiative decay but also the near field effect (CID) promotes demanding photocatalytic reactions. Experiments have been conducted to distinguish these two effect.[49] Additionally, plasmon-mediated hot carriers also offer a novel mechanism to convert optical energy directly to electric current,[50,51] which can be used for developing alternative solar energy harvesting device,[9,16,52] or for designing efficient photo-detectors.[53,54]

Despite fruitful experiments of plasmon-mediated hot carrier devices, several limitations have been identified. For efficient emission, the hot carriers are required to possess sufficient energy compared to the potential barrier between metal nanoparticles and surrounding media, i.e., adsorbed molecules or semiconductors.[55,56] In addition to the injection-barrier limitation, the escape cone restriction states that only a small amount of hot carriers with correct momentum are injected, and the overall efficiency is strongly depended on the momentum matching criteria.[5,57] Furthermore, in order to optimize the performance of plasmon-mediated hot carrier devices, it is critical to fully appreciate the energy distribution and lifetime of hot carriers. Though the lifetime of hot carriers is extensively studied through ultra-fast studies such as transient absorption spectroscopy, the understanding of plasmonically generated hot carriers under conditions of steady state at relatively low power continuous wave (CW) optical excitation that is more directly comparable to sunlight are rarely explored.

In this dissertation, I adopted and modified a free-electron jellium model to calculate the hot carrier energy distribution.[7,58] The model is based on exploring the conduction electrons of the metal as free moving electrons and then analyzing the plasmon-induced dynamics using Fermi's golden rule. By using this model, we calculated the number of hot carriers generated per unit time and we found out that the number and the energy distribution of these hot carriers strongly depend on the size of plasmonic nanostructures and the material temperature. Additionally, by introducing

quantum tunneling phenomena, we proposed a novel strategy to utilize the hot carriers even though their energy is not sufficient to overcome the surface potential barrier.

Furthermore, we developed a Raman spectroscopy technique to quantify the size and energy distribution of plasmonic hot carriers at steady state. An anomaly relationship between the size and energy distribution of hot carriers is observed by this Raman thermometry. Interestingly, we established an unambiguous connection between hot carriers and the full-range Raman spectra of plasmonic metals. We then proposed that the inelastic light scattering is from the non-thermal carriers after LSPR dephasing. At last, we designed a thermionic emission devices utilizing plasmonic hot carriers. The highly energetic hot carriers are thermionic emitted from metal nanostructures and collected from a transparent ITO electrode. The $J - V$ characteristics of thermionic emission proved the presence of plasmonic hot carriers. Further collaborated with Raman spectroscopy, the photophysics of hot carriers at steady state is revealed.

1.2 Metal Nanoparticles and Localized Surface Plasmon Resonance

Metal nanoparticle (NP) has received significant research interest for decades as the concept of nanophotonics thrive. The potential benefits provided by metal NPs are due to the strong sub-wavelength optical field concentration that results from the coupling of resonant oscillations of free electrons in the metal, termed plasmons, with the incident light field. This coupling is due to the unique dielectric constant of coinage metals. In the Drude model the conduction electrons are treated as a free electron gas.[59,60] The response to an electric field is obtained by solving the equation of motion for a single electron, and multiplying by the number of electrons per unit volume, This yields the following expression for the dielectric constant:[59,60]

$$\varepsilon(\omega) = 1 - \frac{\omega_{\mathrm{p}}^2}{\omega(\omega + i\gamma_b)} \qquad (1.1)$$

where ω_{p} is the plasma frequency and γ_{b} is the bulk damping rate that is related to the mean free path l of the electron by $\gamma_b = v_{\mathrm{F}}/l$ where v_{F} is the Fermi velocity. And the plasma frequency is given by $\omega_{\mathrm{P}} = (ne^2/\varepsilon_0 m)^{1/2}$, where n is the electron density, ε_0 is the vaccum permittivity, and m

is the effective mass of the electrons.

For noble metals like Ag and Au, the Drude model gives a good description of the dielectric constants in the near-IR region of the spectrum, but it breaks down in the visible to near-UV region because of interband transition.[61,62] The onset of the interband transitions is at 2.4 eV for gold and 3.9 eV for silver.[63] The interband transitions gives a frequency dependent damping, and can be included in the dielectric constant by adding an extra term.[62,64]

$$\varepsilon(\omega) = \varepsilon^{\mathrm{ib}} + 1 - \frac{\omega_{\mathrm{p}}^2}{\omega(\omega + i\gamma_{\mathrm{b}})} \qquad (1.2)$$

where $\varepsilon^{\mathrm{ib}}(\omega)$ is the interband contribution. Figure 1.1 shows a plot of the real (ε_1) and imaginary (ε_2) components of the dielectric constant for bulk Au, where the low frequency response has been fit to the Drude model using eq 1.1.[62] It is noted that the imaginary component of the dielectric constant is related to damping, and the presence of interband transitions causes a significant increase in damping at energies greater than 2.4 eV.[62,63]

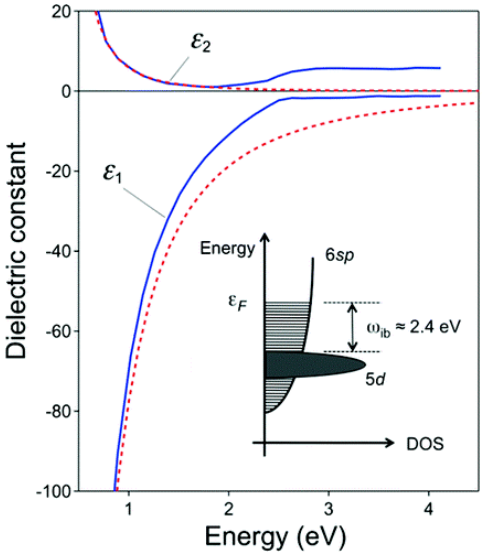

Figure 1.1: Real and imaginary dielectric constant data for gold. The dashed lines show a fit to the data using the Drude model (eq 1.1). The insert shows a cartoon of the band structure of gold. Adapted with permission from Hartland[1]. Copyright 2011 by ACS Publications.

One of the most extensively exploited features of metallic NPs is the LSPR, which refers to the collective oscilaltion of electrons in the metallic NPs excited by the incident photons at the resonant frequency.[1] LSPR is a unique properties of coinage metals and many metal nitrides, which can be understood from dielectric constants. If we treat materials as components in an electric circuit (Figure 1.2), then materials with positive real dielectric constant behave as capacitors and materials with negative real dielectric constant are inductors.[2] Since the imaginary dielectric constant of coinage metals is not zero, the loss is represented by a resistor. Therefore, the plasmonic material which usually has negative real dielectric constant along with its surroundings (surroundings usually have positive dielectric constant) may be treated as a nano LC-circuit, and the LSPR is the resonance frequency of the nano-circuit.

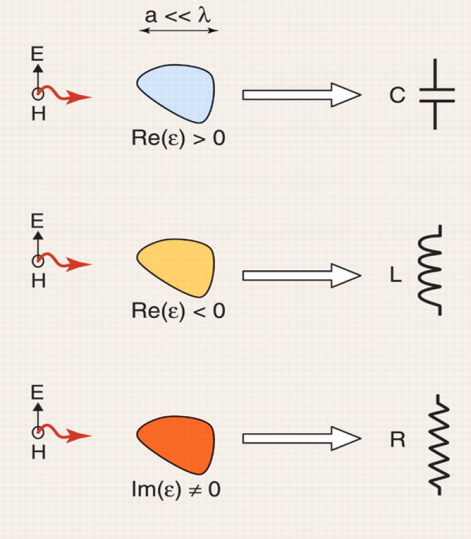

Figure 1.2: A nanoparticle, with subwavelength size, when illuminated by a monochromatic optical signal, can effectively play the role of a lumped optical circuit element, depending on the dielectric constant of its material. Adapted with permission from Engheta[2]. Copyright 2007 by AAAS.

Therefore, plasmonic NPs also offer the ability to tune their optical properties based on composition, shape, and size.[65] The tunable light-matter interactions offer possibilities for photon har-

vesting applications such as photodetection,[23] photovoltaics,[24] artificial photosynthesis,[66] photoelectrochemistry,[67] and photocatalysis.[68]

1.3 Dephase of LSPR and Plasmon-Mediated Hot Carriers

The lifetime of the coherent LSPR oscillation is very short, on the order of femtoseconds.[25] LSPR oscillations dephase (decay) either radiatively, observed as photon scattering, or nonradiatively, observed as photon absorption which is followed by the generation of hot carriers (Figure 1.3).[3] Carriers not in thermal equilibrium with the lattice phonons in a material are frequently referred to as hot carriers. The dominant LSPR dephasing pathway is sensitive to the composition, size, geometry, and local environment of the metal nanostructure.

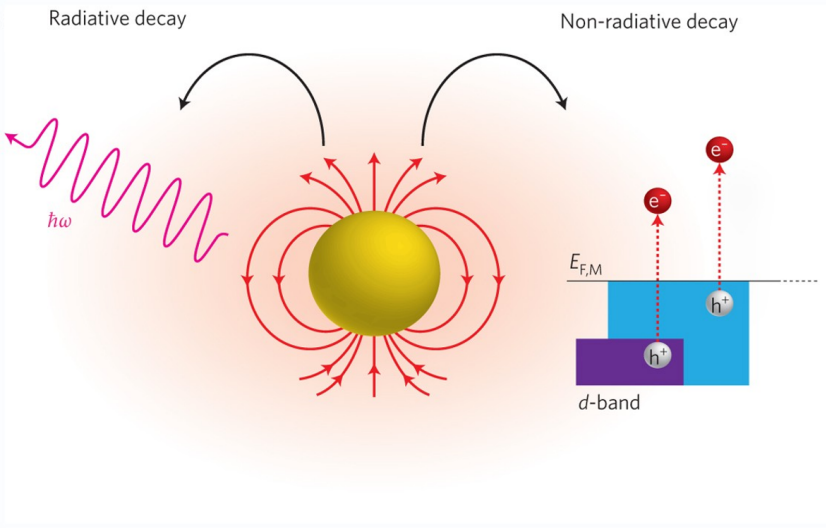

Figure 1.3: Localized surface plasmons can decay radiatively via re-emitted photons or nonradiatively via excitation of hot electrons. Adapted with permission from Clavero[3]. Copyright 2014 by Springer Nature.

In many plasmon-mediated energy conversion technologies, it has been hypothesized that surface plasmons dephase to produce hot carriers in the metal, which migrate to interfaces and then transfer to the surrounding environment. Based on this hypothesis, it has been suggested that small plasmonic nanoparticles should be more efficient than large nanoparticles for certain plasmon-

mediated photon energy conversion processes.[45,69–71] This is because smaller plasmonic nanostructures primarily extinct light through photon absorption, resulting in a higher density of hot carriers compared to larger plasmonic nanostructures, where plasmon dephasing occurs primarily due to radiative decay (Figure 1.4).[8]

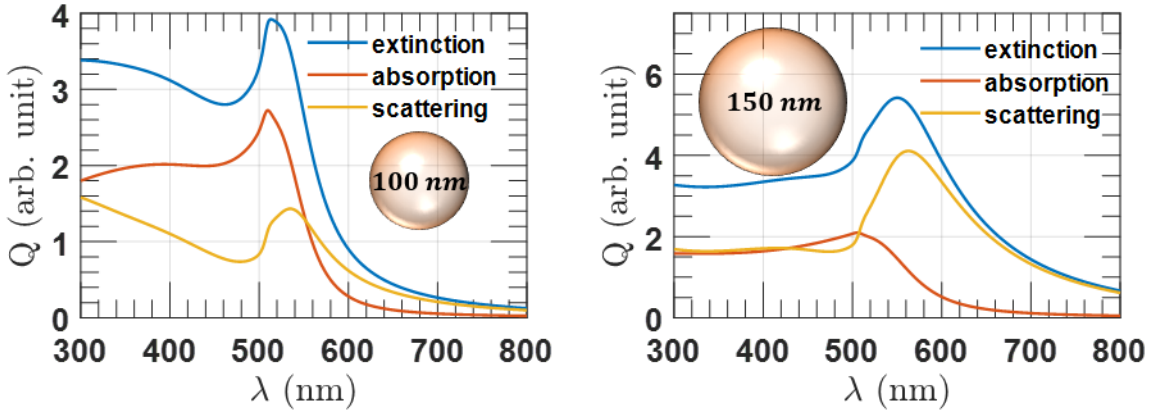

Figure 1.4: Mie efficiency of (left) 100 nm diameter gold NP and (right) 150 nm diameter gold NP.

The dynamic of hot carriers is commonly investigated using ultrafast pump-probe studies. Ultrafast pump-probe measurements of plasmonic nanostructures use a high-intensity laser pulse to excite a large number of electrons and measure the optical response as a function of time using a delayed probe pulse.[1,72] The typical signal observed in these experiments is an initial fast rise ($10 - 100$ fs) attributed to electron-electron scattering that converts fewer high-energy excited carriers into several more lower-energy carriers, followed by a slower decay (100 fs to 1 ps) attributed to electron-phonon scattering.

Figure 1.5 schematically shows the typical electron distributions as a function of time in such ultrafast experiments.[4] This is phenomenologically described by a "two-temperature model" (TTM) that tracks the time dependence of electronic and lattice temperatures, T_e and T_l respectively (eq 1.3). It should be noted that the initial excitation generates an non-thermal carrier distri-

bution that is far from equilibrium for which temperature is not well-defined.

$$C_{\mathrm{e}}(T_{\mathrm{e}})\frac{\mathrm{d}T_{\mathrm{e}}}{\mathrm{d}t} = -g(T_{\mathrm{e}} - T_{\mathrm{l}}) \qquad (1.3a)$$

$$C_{\mathrm{l}}\frac{\mathrm{d}T_{\mathrm{l}}}{\mathrm{d}t} = g(T_{\mathrm{e}} - T_{\mathrm{l}}) \qquad (1.3b)$$

where C_{l} is the lattice heat capacity, $C_{\mathrm{e}}(T_{\mathrm{e}}) = \gamma T_{\mathrm{e}}$ is the temperature dependent electronic heat capacity,[59,60] and g is the electron-phonon coupling constant.[73,74]

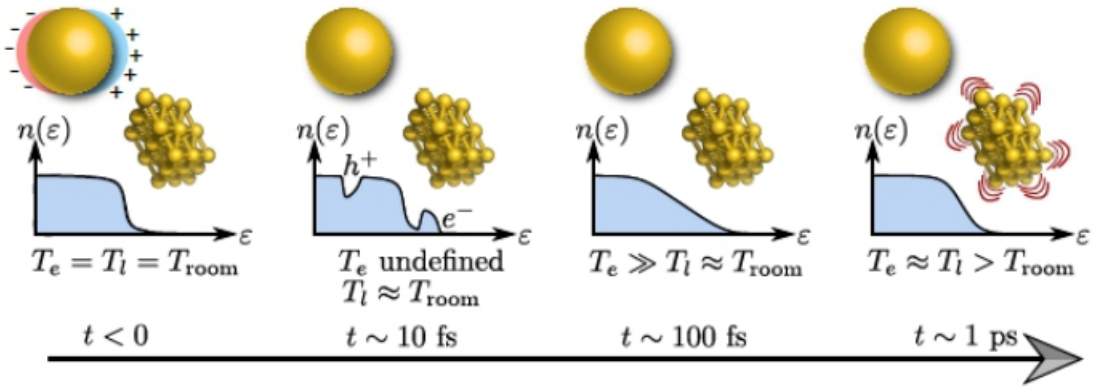

Figure 1.5: Typical time scales for the excitation of hot carriers and their subsequent relaxation. Adapted from Prineha et al.[4].

1.4 Plasmon-Mediated Hot Carrier Applications

As discussed in section 1.3 that hot carrier generation through non-radiative dephase of LSPR is a very promising energy conversion process. The final step of plasmon-mediated hot carrier applications is the injection of the carriers into molecules or adjacent semiconductors to drive chemical reactions. In this section, I review two major hot carrier injection process: solid-state collection (metal-semiconductor interface) and molecular injection (metal-adsorbates interface).

1.4.1 Solid-State Collection

The collection of photo-excited hot carriers over a metal-semiconductor Schottky junction, has been studied extensively and is well-described by the Fowler theory for internal photoemission.[75] The Fowler yield estimate results from a semiclassical model of electrons overcoming an energy barrier as shown in Figure 1.6.[5] Carriers with energy less than the barrier height are reflected. For carriers that cross the barrier, only the normal component of the momentum changes at the interface, which implies that the tangential momentum must be small enough that its kinetic energy contribution in the semiconductor must be less than the excess energy over the barrier; carriers with greater tangential momentum will be reflected (analogous to total internal reflection of light). Therefore, only carriers in an "escape cone" around normal incidence can cross the barrier, and the angle of this cone increases with carrier energy starting from zero for carriers with the threshold energy to cross the barrier.

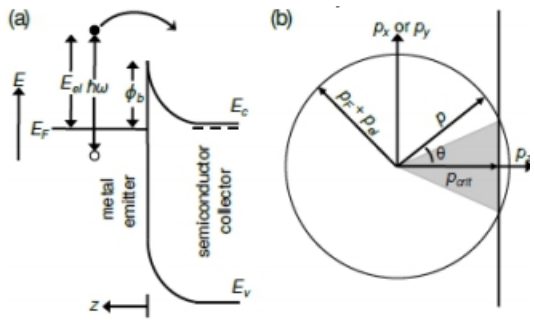

Figure 1.6: (a) Internal photoemission band diagram for hot electrons emitted from a metal into an n-type semiconductor. (b) Schematic of isotropic distribution of hot electron momentum on a sphere in momentum space with a limited escape cone. Adapted with permission from Leenheer et al.[5]. Copyright 2014 by AIP Publishing.

The collection of plasmonics hot carriers has been demonstrated in insulators as well as semiconductors, and the built-in electric fields in the Schottky junction assist in the collection of the emitted hot carriers.[23,76,77] Fowler theory remains qualitatively valid regardless of the band structure of the semiconductor or insulator,[78,79] but the magnitudes can differ substantially for materials

with high density-of-states (DOS) near the band edges. Experimentally, roughened surfaces can overcome "escape-cone" restrictions by providing tangential momentum for the carrier injection.[54]

1.4.2 Molecular Injection: Plasmon-Enhanced Catalysis

Hot carriers generated by plasmon decay can also inject directly into molecules adsorbed at the surface, directly driving chemical reactions for photochemical energy conversion. Surface photochemistry, chemical reactions driven by photoexcited carriers at metal surfaces, has been well studies in many contexts including solar energy conversion and atmospheric chemistry.[80,81] In particular, "semiconductor-free" water-splitting devices using only plasmonic hot carriers have been demonstrated recently.[82]

The basic proposed mechanism for plasmon-driven chemistry involves the injection of an electron from the metal into an anti-bonding state of an adsorbed molecule, causing either desorption or the dissociation of a bond in the adsorbate as shown in Figure 1.7.[83,84] Variants of this mechanism can explain the observed chemical activity of various metal nanostructures, as discussed in detail in a recent review article.[6] The adsorbate forms a transient ion strongly coupled to the plasmonic particle, and the relevant potential energy surface is that of an excited state of the adsorbate-plasmonic particle complex. Theoretical calculations of the excited-state energy landscape using first-principles beyond-ground-state electronic structure methods are therefore essential for predicting such mechanisms.

A second class of possible mechanisms involves plasmonic enhancement of transitions between states localized on the adsorbate.[85,86] Here, the involved excited states are primarily those of the adsorbate, and the metal nanostructure serves to enhance the matrix element for the transition by plasmonic enhancement of the surface electric field. Both types of mechanisms require low-lying molecular orbitals on the adsorbate, but the second class does not rely on alignment of adsorbate levels with those of the metal or on hot carrier transport in the metal.

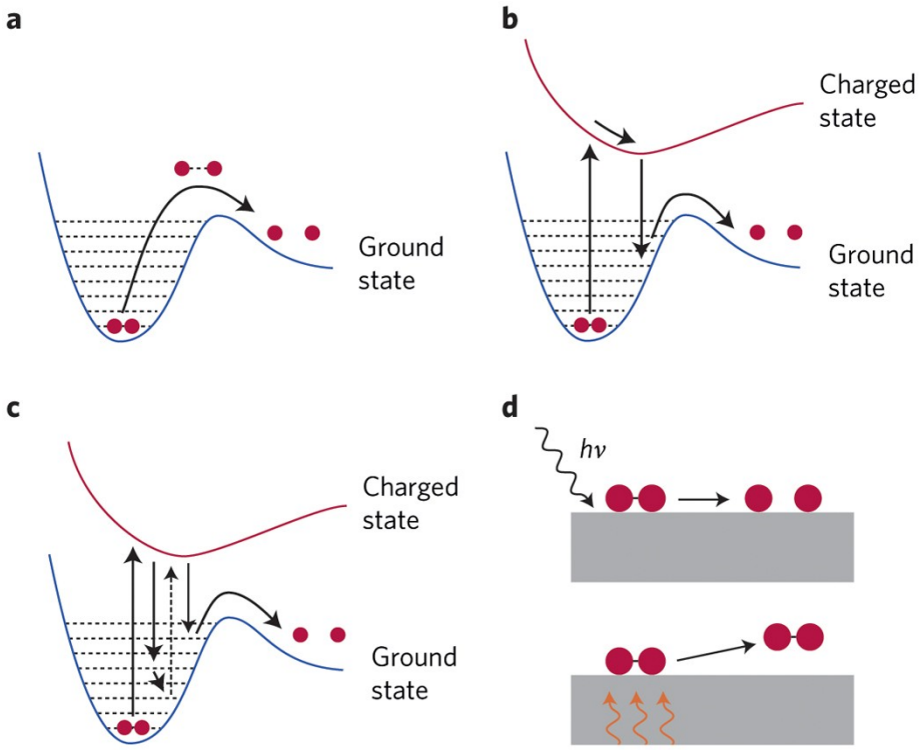

Figure 1.7: (a) Thermal activation for the dissociation of a diatomic molecule. (b) Electron-driven dissociation of a diatomic molecule. (c) At high photon flux, subsequent electron injections can occur before the molecular vibration has fully dissipated. (d) Electron-driven reactions (top), for example on plasmonic metal nanoparticles, can potentially target certain chemical reaction pathways that are otherwise unselective in purely thermal reactions (bottom). Adapted with permission from Linic et al.[6]. Copyright 2015 by Springer Nature.

1.4.3 Outlook

Generation of hot carriers in plasmonic nanostructures is a very promising energy conversion mechanism, and it has found interesting applications in photovoltaic and photocatalytic devices. Four steps are identified in a plasmonic hot carrier driven processes: plasmon excitation, hot carrier generation (non-radiative decay), carrier transport and collection, which builds a complete microscopic picture.

Hot carriers generated by plasmon decay are limited by the photon energy. A given energy-conversion process is usually associated with a characteristic energy, for instance, semiconductor band gap in photovoltaics, such that lower-energy photons are incapable of driving the process,

while the excess energy of higher-energy photons is wasted. The efficiency of solar energy conversion could be improved by harvesting the energy of these higher and lower energy photons. The important link between hot carrier dynamics and the overall performance of hot carrier devices is the energy distribution of hot carriers at steady-state, which is rarely explored. The development of new techniques to investigate the energy distribution of hot carriers at steady-state is therefore important to optimize plasmon-mediated hot carrier applications.

2. QUANTUM TUNNELING PHENOMENON OF NON-THERMAL CARRIERS

2.1 Plasmon-Mediated Non-Thermal Carrier Generation

As discussed in Chapter 1 that hot carriers are generated through non-radiative decay of LSPR. Although direct excitation of hot carriers on metal surfaces is possible and has since long been exploited in the field of surface femotochemistry,[87] the utilization of surface plasmon decay to increase the efficiency of the hot carrier generation process is relatively novel. The basis for this dramatic enhancement is the large plasmon-induced field enhancement and the dramatically enhanced light harvesting capability of the collective plasmon excitation.[18] However, in order to exploit these advantages we need to understand the physical process of plasmon-induced hot carrier generation. In this section, we will review a simple model that describes the generation of plasmon-induced hot carriers in metal NPs.[7,69] *

The theoretical framework previously developed by Manjavacas et al.[7] and Govorov et al.[69] is a jellium model which described the conduction electrons of the metals as free particles and then analyzed the plasmon-induced dynamics using Fermi's golden rule.[88]

$$\Gamma_{\mathrm{e}}(\varepsilon_{\mathrm{f}},\omega)=\frac{4}{\tau}f(\varepsilon_{\mathrm{i}})[1-f(\varepsilon_{\mathrm{f}})]\{\frac{|M_{\mathrm{fi}}(\omega)|^2}{(\hbar\omega-\varepsilon_{\mathrm{f}}+\varepsilon_{\mathrm{i}})^2+\hbar^2\tau^{-2}}+\frac{|M^*_{\mathrm{if}}(\omega)|^2}{(\hbar\omega+\varepsilon_{\mathrm{f}}-\varepsilon_{\mathrm{i}})^2+\hbar^2\tau^{-2}}\} \tag{2.1}$$

where f is the Fermi-Dirac distribution function, in which for simplicity is commonly assumed at zero temperature, τ is the plasmon dephasing time, $M_{\mathrm{fi}}=\int drV(r,\omega)\rho_{\mathrm{fi}}(r)$ is the transition matrix element, and a factor of 2 to account for the spin is included. $\rho_{\mathrm{fi}}(r)=e\Psi^*_{\mathrm{f}}(r)\Psi_{\mathrm{i}}(r)$ where e is the elementary charge, subscript i and f stand for initial and final states, and $V(r,\omega)$ is the plasmon-induced potential. It is noted that eq 2.1 contains two Lorentzian functions of width τ^{-1}, which is further discussed in Chapter 3.

The model presented here involves two approximations: (i) the electrons are assumed to remain

*Section 2.3 is adapted with permission from Wu, S.; Sheldon, M. T., Optical Power Conversion Via Tunneling of Plasmonic Hot Carriers. *ACS Photonics* **2018**, 5 (6), 2516-2523. Copyright 2018 ACS Publications.

in their ground state even when a plasmon is excited; and (ii) the plasmon is assumed to lose only a single plasmon quantum during each hot carrier generation process. These assumptions are realistic given the short lifetime ($\approx 10\,\mathrm{fs}$) of the plasmon excitation, the large cross section for plasmon excitation that results in plasmons being excited to high quantum numebrs n, and the sequential nature of nonradiative plasmon decay.

Figure 2.1(b) shows the total number of hot electrons generated per unit of time and volume as a function of the frequency of the external illumination. As expected, the generation rate follows the absorption profile of silver nanosphere (Figure 2.1(c)). The results plotted with red lines in Figure 2.1(b) have been obtained using the free electron wave functions and energies (eq 2.1). Interestingly, the inclusion of many-body interactions (blue lines) using density functional theory (DFT) only has a minor impact. Therefore, the exchange-correlation effects can be ignored at the present level of approximation. One expects to find even better aggrement in materials with larger workfunctions and smaller plasmonic energies, for which the relevant electronic states lay deeper in the potential well.

Keep in mind that in order to optimize the hot carrier applications, it is equally important to investigate the total number of carriers generated at a certain frequency, but also their energy distribution. This is shown in Figure 2.2, where the energy of the hot carriers generated in gold nanoparticles with different diameters are analyzed.[8] It turns out that the size of nanoparticles plays a crucial role in hot carrier generation. In this case, larger diameters produce less energetic carriers and vice versa. The origin of this behavious can be traced to the density of electronic states of these systems. Specifically, systems with a finite number of electrons have a finite number of energy levels and therefore, a discrete density of states.

Furthermore, since the total amount of energy dissipated in the carrier generation is fixed by the optical absorption of the nanoparticle, situations in which hot carriers are generated with energies close to the Fermi level must be associated with larger production rates. Similarly, high energy non-thermal carriers are generated in smaller numbers. This is clearly corroborated by the results shown in Figure 2.2.

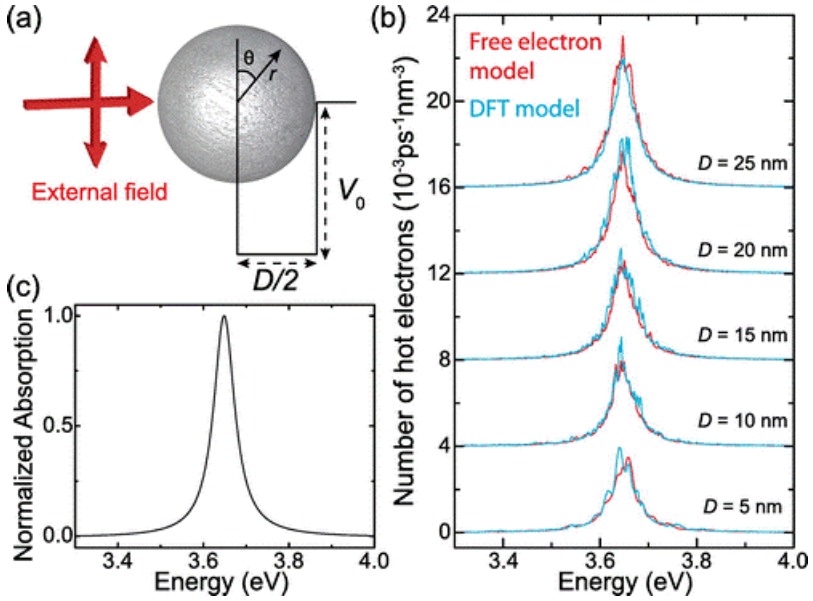

Figure 2.1: Plasmon-induced hot electron production in a silver nanoparticle. (a) Schematic representation of the system under study. (b) Number of hot electrons generated per unit of time and volume as a function of the frequency of the external illumination. (c) Normalized absorption for the silver nanoparticle calculated in the quasi-static limit. Adapted with permission from Manjavacas et al.[7]. Copyright 2014 by ACS Publications.

2.2 Modeling Non-Thermal Carrier Generation in Gold Nanocubes and Films

2.2.1 Modeling Framework

Since the jellium model discussed in previous section is a free-electron model, the wavefunction of electrons in gold nanocubes is approximated as particles in 3D box. The Schrödinger equation of electron state is described by three quantum numbers $(n_{\mathrm{x}}, n_{\mathrm{y}}, n_{\mathrm{z}})$ and the corresponding energy is written as

$$\Psi(x,y,z) = (\frac{2^3}{L_{\mathrm{x}}L_{\mathrm{y}}L_{\mathrm{z}}})^{1/2}\sin(\frac{\pi n_{\mathrm{x}}x}{L_{\mathrm{x}}})\sin(\frac{\pi n_{\mathrm{y}}y}{L_{\mathrm{y}}})\sin(\frac{\pi n_{\mathrm{z}}z}{L_{\mathrm{z}}}) = \psi_{n_{\mathrm{x}}}(x)\psi_{n_{\mathrm{y}}}(y)\psi_{n_{\mathrm{z}}}(z) \qquad (2.2a)$$

$$E(n_{\mathrm{x}}, n_{\mathrm{y}}, n_{\mathrm{z}}) = \frac{\hbar^2\pi^2}{2m}(\frac{n_{\mathrm{x}}^2}{L_{\mathrm{x}}^2} + \frac{n_{\mathrm{y}}^2}{L_{\mathrm{y}}^2} + \frac{n_{\mathrm{z}}^2}{L_{\mathrm{z}}^2}) \qquad (2.2b)$$

where L_{x}, L_{y} and L_{z} are dimensions of plasmonic nanocubes in x, y and z directions.

Before we move to the jellium model (eq. 2.1), we need to closely investigate the density of

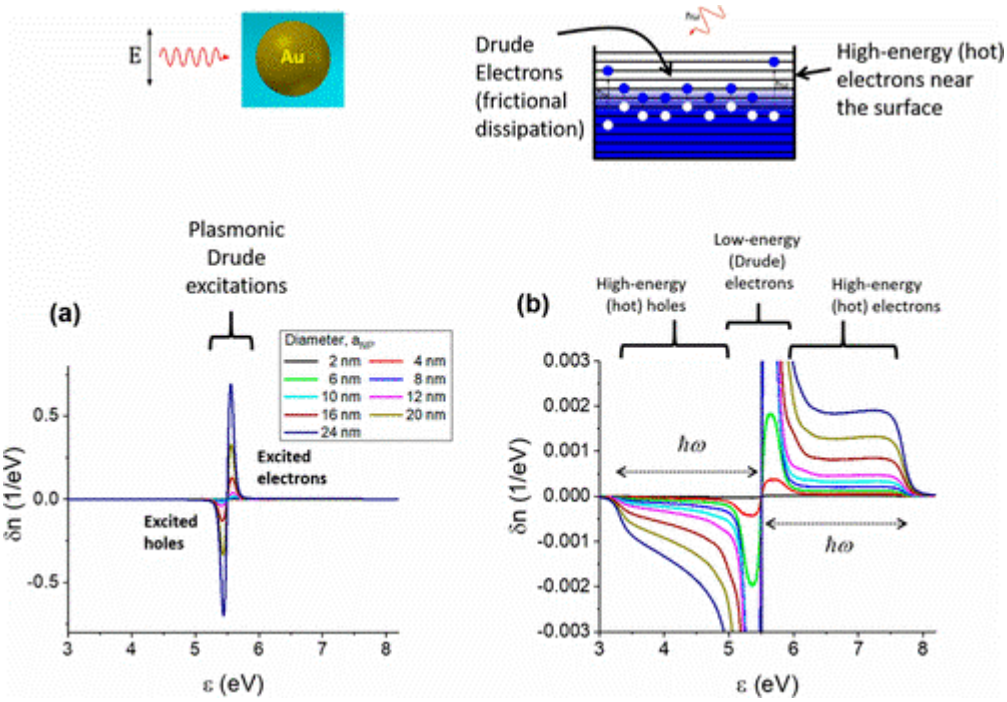

Figure 2.2: (a) Calculated distribution of excited electrons and holes in the Fermi sea of a nanoparticle. (b) Closer look at the plateau region with the hot electrons generated by quantum surface-assisted transitions. Adapted with permission from Hartland et al.[8]. Copyright 2017 by ACS Publications.

states (DOS) simulated from eq. 2.2, which is shown as blue bars in Figure 2.3. Expectedly, the quantized DOS (blue bars) for $D = 10\,\mathrm{nm}$ gold nanocube agrees well with the classical-calculated DOS (red line).[60] One may imagine that as the dimension of gold nanostructures increases, the quantized DOS shall approach the classical result, which is another example of *Bohr correspondence principle*. Additionally, the Fermi energy of $D = 10\,\mathrm{nm}$ gold cube is slightly greater than bulk gold ($5.5\,\mathrm{eV}$),[89] which is due to the discreteness nature of quantum mechanics.

Keep in mind that the key component in eq 2.1 is the transition matrix $M_{\mathrm{fi}} = \int \mathrm{d}r V(r,\omega)\rho_{\mathrm{fi}}(r)$. Since the dimension of plasmonic nanocube under study is smaller compared to the wavelength of incident illumination, we can assume the quasi-static condition that the induced electric field is uniform and does not vary spatially inside the plasmonic nanocube. Therefore, the induced potential V can be found by $\overrightarrow{E}(\omega) = -\nabla V(r,\omega)$ or $V = r\overrightarrow{E}$.

With the information of induced potential, either calculated using the quasi-static assumption

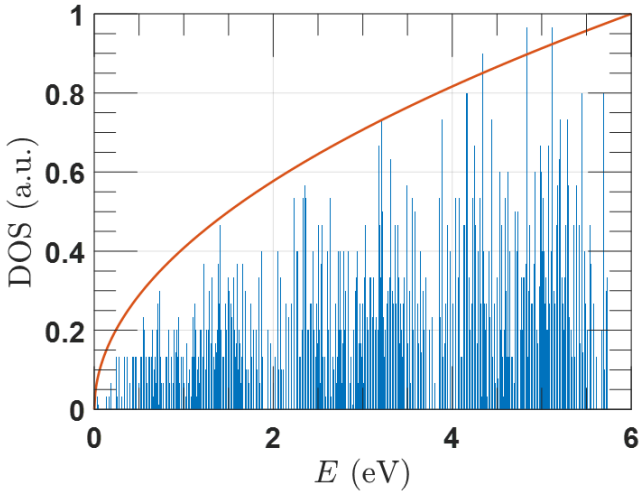

Figure 2.3: Quantized DOS (blue bars) of $D = 10\,\mathrm{nm}$ gold nanocube and Classical DOS of bulk gold.

or simulated through a electromagnetic solver (*Finite Element Method* or *Finite-Difference-Time-Domain* method), one may find the non-thermal carrier generation rate of plasmonic nanocubes is (see Appendix for details):

$$\langle \Psi_{\mathrm{f}}^{*} | eV(r) | \Psi_{\mathrm{i}} \rangle = \frac{2n_{\mathrm{x,i}} L_{\mathrm{x}} \overrightarrow{E}}{\pi^2 (n_{\mathrm{x,f}}^2 - n_{\mathrm{x,i}}^2)} \delta_{n_{\mathrm{y,i}}, x_{\mathrm{y,f}}} \delta_{n_{\mathrm{z,i}}, x_{\mathrm{z,f}}}$$

$$[\frac{1}{(n_{\mathrm{x,f}} + n_{\mathrm{x,i}})}(1 - \cos(\pi(n_{\mathrm{x,f}} + n_{\mathrm{x,i}}))) + \frac{1}{(n_{\mathrm{x,f}} - n_{\mathrm{x,i}})}(1 - \cos(\pi(n_{\mathrm{x,f}} - n_{\mathrm{x,i}})))] \qquad (2.3)$$

It should be noted that the selection rule states that $\Delta n_{\mathrm{x}} = n_{\mathrm{x,f}} - n_{\mathrm{x,i}}$ must be an odd number, otherwise eq 2.3 returns a zero production rate.

2.2.2 Size-Dependence and Temperature-Dependence of Non-Thermal Carrier Generation

In this section, we choose to investigate the non-thermal carrier production in gold nanocubes under $532\,\mathrm{nm}\,(2.3\,\mathrm{eV})$ CW illumination to ensure most of excitation is intraband transition. The Au cube has a permittivity adopted from Johnson and Christy[61] and the dephasing time τ can be different from the Drude damping rate $\hbar\gamma$, however with an upper bound of $\hbar\gamma$.[89] Since its value is not known from experiments, we make a conservative choice of τ being equal to the Drude

damping rate of bulk gold.

Figure 2.4 shows the major results of non-thermal carrier production rate of two gold nanocubes with $D = 5\,\mathrm{nm}$ and $D = 10\,\mathrm{nm}$. As expected, we found the same size-dependence in agreement with Manjavacas et al.[7] that larger nanosystems produce less energetic carriers and vice versa (Figure 2.4(c,d)). The 'kinks' in Figure 2.4 is due to the discreteness nature of quantized states. Therefore, it is a "win-win" situation to exploit smaller plasmonic nanostructures for hot carrier application: (i) Smaller nanoparticles favors non-radiative decay which excite hot carriers more efficiently, (ii) Non-thermal carriers have greater energy and thus have the potential to drive more energy-demanding chemical reactions.

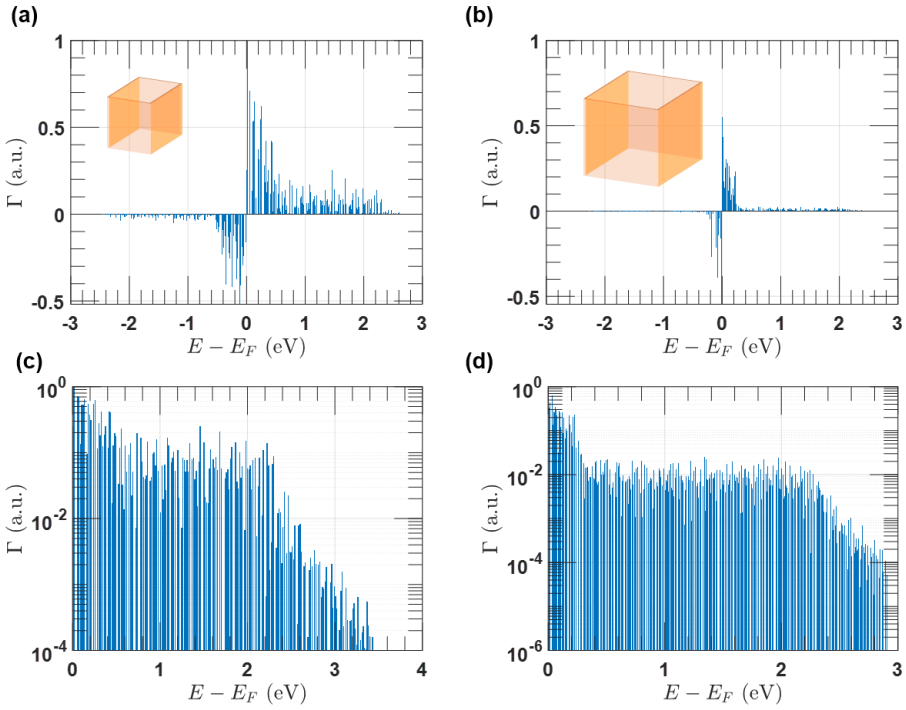

Figure 2.4: Non-thermal carrier production rate of gold nanocubes with (a) $D = 5\,\mathrm{nm}$, (b) $D = 10\,\mathrm{nm}$ and corresponding zoom-in view of hot electrons in (c), (d).

The jellium model eq 2.1 has been applied in many plasmonic nanostructures, including nanosphere, nano-star, nanorod, etc.[90,91] However, since the exact wavefunction of the jellium model is re-

quired, the computation cost increase cubically with the size of nanosystem. Realistically, it is more interested to investigate the non-thermal carrier generation in film-like structure, i.e. quantum well which only one dimension is restricted. If we assume the restricted dimension is x (Figure 2.5 inset), the state energy ε is then written as $\varepsilon = \varepsilon_{\mathrm{y,z}} + \varepsilon_{\mathrm{x}}$ where $\varepsilon_{\mathrm{y,z}}$ is the state energy in y and z directions. By using smallest energy step $\hbar^2\pi^2/2m$ as defined in eq 2.2b, we are able to capture the non-thermal carrier production rate of film-like structure. Figure 2.5 presents the calculated results of non-thermal carrier generation in gold film under $532\,\mathrm{nm}\,(2.3\,\mathrm{eV})$ illumination.

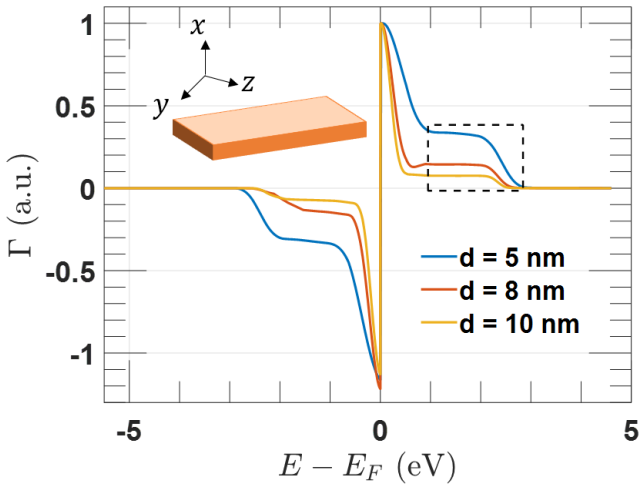

Figure 2.5: Non-thermal carrier production rate of gold films with different thickness d.

Agreed with Govorov and Zhang[89], the non-thermal carrier production of gold film contains two components: Drude like carriers (close to Fermi level) and high-energy excited carriers (dashed rectangle). It is noted that even only x axis is restricted, the same size-dependence is observed. Thinner gold film produce more high-energy excited carriers and vice versa. One can imagine that as the thickness d increases, the energy of non-thermal carrier distribution approaches a Lorentzian function.

To simplify calculation, many researchers assumes absolute zero when using eq 2.1 to calculate the energy of non-thermal carriers. In real world, however, materials are measured far above

absolute zero given that photo-thermal effect of external illumination is inevitable. Thus we further investigate the temperature-dependence of non-thermal carrier generation to complete the puzzle. Figure 2.6(a) shows the temperature-dependence non-thermal carrier generation rate of $d = 5\,\mathrm{nm}$ gold film under $532\,\mathrm{nm}\,(2.3\,\mathrm{eV})$. It is noted that the area under curve in Figure 2.6(a) is constant for each temperature to ensure energy conservation. Interestingly, we found that the number of high-energy excited carriers decreases as the ratio of Drude-like carrier (blue region) and high-energy excited carriers (green region) increases with temperature (Figure 2.6(b)).

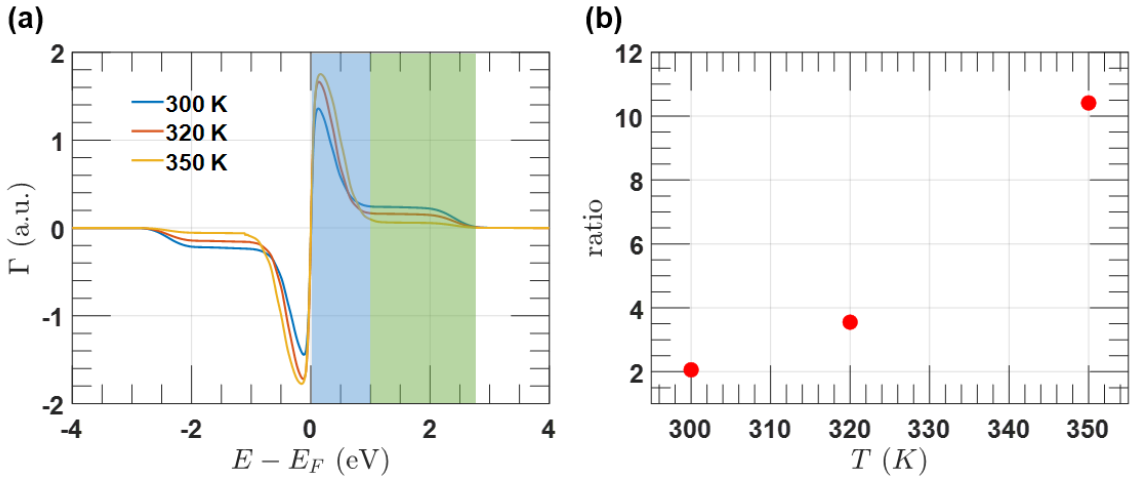

Figure 2.6: (a) Non-thermal carrier production rate of gold films calculated assumed different temperature and (b) Temperature-dependence of ratio of Drude-like carrier (blue region) and high-energy excited carriers (green region).

To recapitulate, we have used the jellium model to calculate the energy distribution of non-thermal carriers in plasmonic nanocubes. We have also expanded the model to a more realistic scenario: larger nanosystem and finite temperature. The insight provided in this section is believed to provide essential guidence in plasmon-mediated hot carrier photocatalysis under steady state.

2.3 Quantum Tunneling of Plasmon-Mediated Non-Thermal Carriers

Though the lifetime of non-thermal carrier is extremely short that they exchange energy quickly through electron-electron scattering $(10 - 100\,\mathrm{fs})$,[25] it is believed that a small fraction of non-

thermal carriers are present under steady state. Recently, Reddy et al.[92] conducted a single-molecule transport measurement and confirmed the presence of plasmon-mediated non-thermal carriers under steady state. It is therefore possible to extract the highly energetic non-thermal carriers before they annihilated with each other to drive chemical reactions.

As discussed in Chapter 1 that a major limitation of plasmon-mediated hot carriers devices is that carriers are required to possess sufficient energy compared to the potential barrier between metal nanoparticles and surrounding media. Several strategies have been investigated to address this challenge, i.e. surface engineering by introducing low workfunction material to reduce potential barrier.[16] In this section, we exploit a novel strategy, named quantum tunneling, to address the injection-barrier limit and improve the injection efficiency of plasmon-mediated carriers.

The central idea of quantum tunneling is summarized in Figure 2.7. Classically, an electron with smaller energy compared to barrier height is reflected. Quantum mechanically, however, the wavefunction is not diminished inside the classically forbidden region. Therefore, there is a probability for an electron to 'tunnel' through the barrier and be injected into surrounding media.

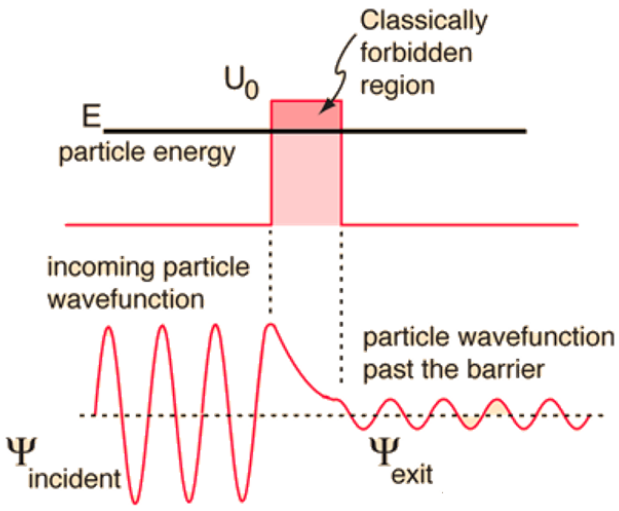

Figure 2.7: Scheme of quantum tunneling.

Tunneling will occur with a probability defined by the transmission coefficient $\mathrm{P}(E)$ when the

energy E is less than the barrier height U (see appendix for details).

$$\mathrm{P}(E) = e^{-(2/\hbar)s\sqrt{2m(U-E)}} \qquad (2.4)$$

Here, s is the thickness of barrier and m is the electron mass. It is noted that thermionic emission (discussed in Chapter 4) and photo emission occur with unity efficiency, $\mathrm{P}(E) = 1$, when electrons have sufficient thermal energy or energy from absorbed photons, respectively, to overcome the barrier height.

To illustrate how it is possible to more fully utilize the electrical carriers excited in a metal during optical absorption by taking advantage of tunneling transport phenomena, we envisioned a plasmonic tunneling junction (Figure 2.8(a)) with a strong asymmetry in the optical response on opposite sides of a junction. This asymmetry can promote optical absorption that results in both uneven photothermal heating and unbalanced optically excited electron distributions on opposite sides of a nanoscale gap.

To tell the story, we first modeled the electron distribution in a metal as:[60]

$$n(v)\mathrm{d}v_\mathrm{x}\mathrm{d}v_\mathrm{y}\mathrm{d}v_\mathrm{z} = \frac{2m^3}{h^3} f(E)\mathrm{d}v_\mathrm{x}\mathrm{d}v_\mathrm{y}\mathrm{d}v_\mathrm{z} \qquad (2.5)$$

Here, n is the electron density, v is electron velocity, v_x, v_y, v_z are electron velocity in the x, y, z directions, respectively, m is electron mass, h is Planck's constant, and $f(E)$ is the Fermi-Dirac distribution function at energy E.

For simplicity, we consider electron transport in the x direction and we rewrite eq 2.5 in terms of v_x:

$$n(v_\mathrm{x}) = \frac{2m^3}{h^3} \int \int_{-\infty}^{\infty} f(E)\mathrm{d}v_\mathrm{y}\mathrm{d}v_\mathrm{z} = \frac{2\pi m^2}{h^3} \int_0^{\infty} f(E)dE_\mathrm{r} \qquad (2.6)$$

where $v_\mathrm{r}^2 = v_\mathrm{y}^2 + v_\mathrm{z}^2$, $E_\mathrm{x} = \frac{1}{2}mv_\mathrm{x}^2$ and $E_\mathrm{r} = E - E_\mathrm{x} = \frac{mv_\mathrm{r}^2}{2}$.

The electron flux, $N_{\mathrm{l}\to\mathrm{r}}$, from left to right, can be calculated by integrating the product of eq

2.6 with electron velocity v_{x} and emission probability $\mathrm{P}(E)$ for all possible electron energies.

$$N_{\mathrm{l}\to\mathrm{r}} = \int_0^\infty v_{\mathrm{x}} n(v_{\mathrm{x}}) \mathrm{P}(E_{\mathrm{x}}) \mathrm{d}v_{\mathrm{x}} = \frac{1}{m} \int_0^\infty n(v_{\mathrm{x}}) \mathrm{P}(E_{\mathrm{x}}) \mathrm{d}E_{\mathrm{x}} \qquad (2.7)$$

In this section, we analyzed a $\mathrm{Au} - \mathrm{Vacuum} - \mathrm{Au}$ junction, where the barrier height $U = 4.6\,\mathrm{eV}$ corresponds to the work function of gold.[89] We also considered an $\mathrm{Au} - \mathrm{TiO_2} - \mathrm{Au}$ with $U = 1\,\mathrm{eV}$ based on the interfacial metal-semiconductor Schottky barrier height.[93]

Since electrons can be transmitted across the plasmonic junction from left to right and vice versa, the net current density J needs to account for electron transport in both directions.

$$J = e(N_{\mathrm{l}\to\mathrm{r}} - N_{\mathrm{r}\to\mathrm{l}})/S \qquad (2.8)$$

Here, e is elementary charge, S is the active area of the junction interface, and we defined positive current flowing from left to right. Eq 2.8 indicates that if the plasmonic tunneling junction has identical electron distributions on both sides, the electron flux transmitted from left to right would cancel out the electron flux transmitted from right to left, resulting in zero net current density.

We consider how plasmonic absorption in the metal can break the symmetry of the junction in order to promote a net current density. We analyze electron transport that results from temperature differences across the junction due to uneven photothermalization and, separately, uneven non-thermal carrier generation via differences in photoexcitation on opposite sides of the junction. Both effects redistribute electron density $n(v_{\mathrm{x}})$ asymmetrically across the junction, thus resulting in a net current density. A temperature variation results in a different Fermi-Dirac distribution for electrons on either side of the junction. The hot side of the junction has more electrons occupying higher energy states and thus has greater probability for tunneling, even if the thermal energy is too small to provide a significant current for thermionic emission.

Optical absorption is a local quantity that can be calculated by integrating the product of frequency ω, the electric field strength $|\overrightarrow{E}|^2$, and the imaginary part of the dielectric permittivity over the full volume of the nanostructure. During steady-state illumination, uneven optical absorption

on opposite sides of the plasmonic tunneling junction can be promoted by tailoring the optical response of each metallic nanoelectrode. This uneven absorption can provide a temperature gradient across the junction affecting all electrons, as well as a steady-state subpopulation of photoexcited electrons, which are in the process of thermalizing via electron-electron and electron-phonon scattering. Although both effects correspond to different stages of the same microscopic relaxation process, for simplicity we first analyze the transport behavior of the thermally distributed electrons separated from the transport behavior of photoexcited electrons. Both consequences of optical absorption can significantly modify the electron distribution on one side of the junction compared to the other, and both thermal and non-thermal electrons are expected to contribute to the net electrical current across an illuminated tunnel junction.

Once a thermal gradient is established, electrons that are not photoexcited are distributed in energy based on Fermi-Dirac distribution described by the local temperature. More electrons occupy higher energy states on the hot side of the junction and thus have greater tunneling probability. Figure 2.8 shows a summary of the transport calculations of plasmonic junctions with $1\,\mathrm{nm}$ tunneling gap subject only to a temperature gradient. Our calculation probed temperature differences that were varied between 0 and $10\,\mathrm{K}$ (Figure 2.8(a)), which is consistent with temperature differences that were experimentally maintained in similar nanoscale thermophotovolatic power generator devices.[94,95]

A nonzero short-circuit current density, J_{sc}, is observed that flows from the hot to the cold nanoelectrode. In addition, a voltage V_{bias} is calculated that was applied opposite the current direction, corresponding to a circuit load. The output power density P_{output} provided by the junction is determined by the product of the applied voltage and the current density. The minimum applied voltage that completely canceled the tunneling current corresponds to the open-circuit voltage, V_{oc}, of the illuminated junction. In addition to modeling a $\mathrm{Au}-\mathrm{Vacuum}-\mathrm{Au}$ junction, we also calculated the transport behavior of a $\mathrm{Au}-\mathrm{TiO_2}-\mathrm{Au}$ junction. Titanium dioxide ($\mathrm{TiO_2}$) is a thermally stable, transparent, wide band gap insulator that is commonly used as an electrode for plasmonic hot electron devices, because fast electron injection over the interface Schottky barrier

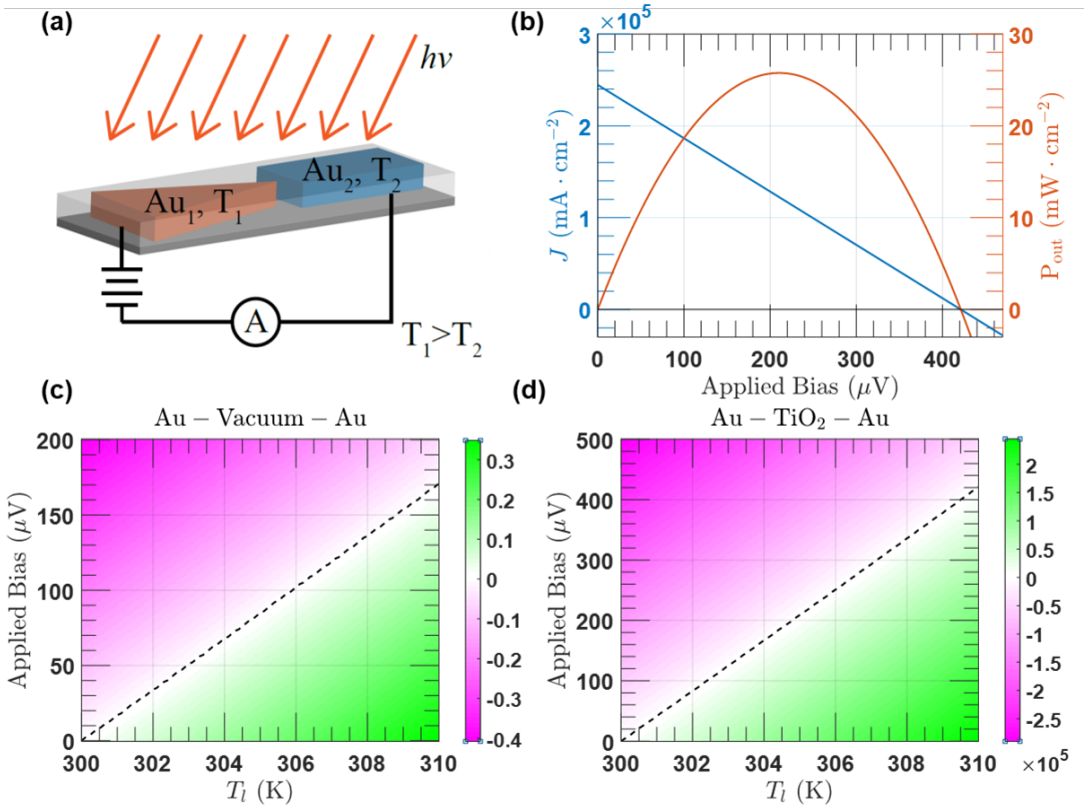

Figure 2.8: (a) Scheme of the envisioned plasmonic tunneling junction subject to a thermal gradient, $\Delta T = T_1 - T_2$. (b)$J-V$ (blue) and $P-V$ (red) curve of the $\mathrm{Au-TiO_2-Au}$ junction when $T_\mathrm{l} = 310\,\mathrm{K}$ and $T_\mathrm{r} = 300\,\mathrm{K}$. $J-V$ map as a function of T_l and applied bias with fixed $T_\mathrm{r} = 300\,\mathrm{K}$ for (c) a $\mathrm{Au-Vacuum-Au}$ junction and (d) a $\mathrm{Au-TiO_2-Au}$ junction. The dashed trace shows the open-circuit voltage at a given T_l and the unit in colorbar is $\mathrm{mA/cm^2}$. Adapted with permission from Wu and Sheldon[9]. Copyright 2018 by ACS Publications.

and good carrier collection are reported when $\mathrm{TiO_2}$ is contacted to plasmonic metals.[96]

Figure 2.8(c, d) shows the current-voltage ($J-V$) characteristics of both modeled plasmonic junction in a temperature range near $300\,\mathrm{K}$. The short-circuit current density increases with larger temperature difference across the junction. More electrons are thermally activated on the hot side into states that have a higher probability of tunneling, so there is a net tunneling current. A current density up to $350\,\mu\mathrm{A/cm^2}$ and an open-circuit voltage of $170\,\mu\mathrm{V}$ for a maximum power density of $0.0015\,\mu\mathrm{W/cm^2}$ is predicted for the $\mathrm{Au-Vacuum-Au}$ tunneling junction. It should be noted that this power density is solely attributed to electron tunneling, since there is negligible thermionic emission in this temperature range. The open-circuit voltage is comparable to the thermoelectric

potential of Au based on the Seebeck coefficient of Au of $6.5\,\mu\mathrm{V/K}$.[97] Although similar in design, the power density provided by this tunneling junction is smaller than typical thermionic emission devices.[98] However, the calculated current density is orders of magnitude larger than comparable thermionic devices operating at such a low temperature range. Typical thermionic devices are operated at much higher temperature above $1000\,\mathrm{K}$, and the emitting metal surface is usually treated with cesium vapor to decrease the work function barrier height to about $1.6\,\mathrm{eV}$.[98] Since the tunneling probability is also limited by the dependence on the barrier height, i.e., the work function of Au in eq 2.4, we also compared these results with a shallower tunnel barrier of $1\,\mathrm{eV}$, defined by the $\mathrm{Au-TiO_2}$ Schottky barrier height (Figure 2.8(d)). A significant enhancement of short-circuit current to $2.446\times10^5\,\mathrm{mA/cm^2}$ is calculated, as well as an increase of the open-circuit voltage to $420\,\mu\mathrm{V}$ with a power density of $25\,\mathrm{mW/cm^2}$ at the maximum temperature gradient ($\Delta T = 10\,\mathrm{K}$), as depicted in Figure 2.8(b). Even for the $\mathrm{Au-TiO_2-Au}$ tunneling junction, such a high current density and power output are solely attributed to electron tunneling, because there is negligible thermionic emission at this temperature.

Upon illumination, direct photoexcitation of a subpopulation of electrons occurs, in addition to the photothermal heating of all electrons analyzed above. The calculated rate of nonthermal carriers is discussed in previous section (Figure 2.5). Due to the quantum confinement effects, nonthermal carriers generated in small gold nanostructures tend to display a wider energy distribution than photoexcited bulk metal, with a significant population of electrons across the range $E_\mathrm{F}\pm h\nu$.[69] We expect that this large non-thermal carrier energy distribution can facilitate a more energetic imbalance in the electron population in one nanoelectrode compared to the other, resulting in larger current densities compared with pure thermal gradients.

To quantify how hot electron generation can enhance unidirectional electron transport, we first analyzed the idealized device geometry depicted in Figure 2.9. This scenario assumes the maximum possible asymmetry of absorption with only one of the gold nanoelectrodes is illuminated. Intuitively, optically induced photothermal heating of the entire electron gas occurs after the nonthermal electrons are excited and then thermalized.[99,100] Therefore, if all non-thermal electrons

are collected via tunneling before relaxation, we would expect no photothermal heating of the metal. However, we anticipate that both mechanisms of electron excitation (thermal and nonthermal) would be present in the steady state for a real device because of imperfect collection of all non-thermal electrons before they relax. The resulting asymmetric steady-state temperature profile is expected to have a complex dependence on the incident optical power, the thermal conductivity of the materials and other heat transfer channels present in the system, in addition to the hot carrier collection efficiency. For simplicity, our calculation analyzed the same temperature gradients studied above (ΔT ranges from 0 to $10\,\mathrm{K}$ near $300\,\mathrm{K}$), and the non-thermal effect of electron photoexcitation is analyzed as an independent perturbation in addition to a temperature gradient that results from asymmetric optical absorption. For comparison, we also analyzed the system performance at an elevated temperature (500 to $510\,\mathrm{K}$) corresponding to temperature gradients achieved in solar concentrator schemes.[101]

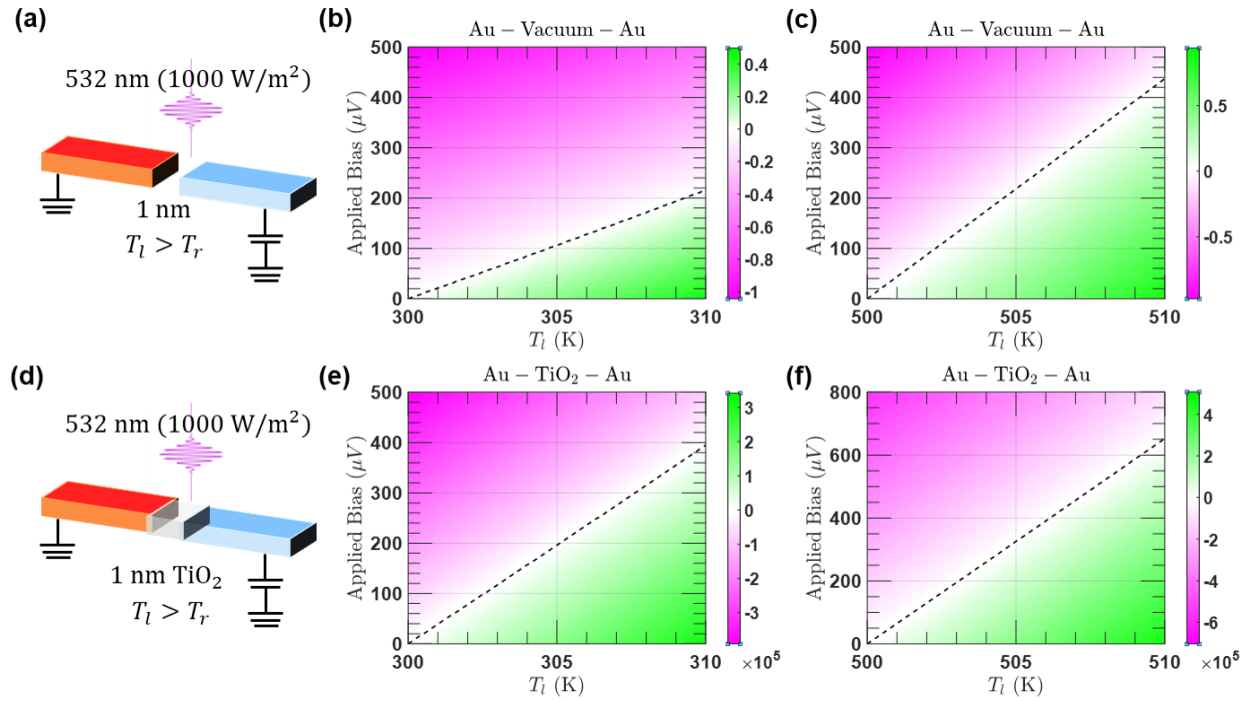

Figure 2.9: Idealized geometry of (a) $\mathrm{Au-Vacuum-Au}$ junction and (d) $\mathrm{Au-TiO_2-Au}$ junction subject to a thermal gradient and imbalanced photoexcitation. $J-V$ map as a function of T_l and applied bias with fixed at (b,e) $T_\mathrm{r} = 300\,\mathrm{K}$ and (c,f) $T_\mathrm{r} = 500\,\mathrm{K}$. The unit in colorbar is $\mathrm{mA/cm^2}$. Adapted with permission from Wu and Sheldon[9]. Copyright 2018 by ACS Publications.

Figure 2.9 shows the $J-V$ profile of $\mathrm{Au-Vacuum-Au}$ and $\mathrm{Au-TiO_2-Au}$ plasmonic junctions at two temperature ranges (300 to $310\,\mathrm{K}$ and 500 to $510\,\mathrm{K}$) when only one gold nanoelectrode is illuminated by $1000\,\mathrm{W/m^2}\,532\,\mathrm{nm}$ monochromatic light. We note that this is a nonideal measurement of the device power conversion efficiency, because it does not account for how much optical energy is required to maintain the thermal gradient. As discussed above, greater current density and open-circuit voltage are observed for a $\mathrm{Au-TiO_2-Au}$ plasmonic junction due to the reduced energy barrier in comparison with an $\mathrm{Au-Vacuum-Au}$ junction. Near room temperature (300 to $310\,\mathrm{K}$), a significantly increased V_{oc} and J_{sc} is predicted for both a $\mathrm{Au-Vacuum-Au}$ and $\mathrm{Au-TiO_2-Au}$ tunneling junction compared with the purely thermally mediated tunneling discussed in Figure 2.8. Furthermore, while the range of ΔT is the same, significantly enhanced J_{sc} and V_{oc} are obtained at elevated temperature ($500\,\mathrm{K}$) compared to room temperature. Specifically, there is a 100% increase of V_{oc} at $500\,\mathrm{K}$ vs $300\,\mathrm{K}$ for an $\mathrm{Au-Vacuum-Au}$ junction (from $220\,\mu\mathrm{V}$ to $440\,\mu\mathrm{V}$) and a 60% increase of V_{oc} for a $\mathrm{Au-TiO_2-Au}$ junction (from $400\,\mu\mathrm{V}$ to $640\,\mu\mathrm{V}$). Thus, electron thermalization interacts cooperatively with non-thermal excitation mechanisms in this device.

In order to bolster our hypothesis that asymmetries in electronic excitation across tunneling gaps can be maintained by tailoring the optical response of each metallic-nanoelectrode, we used full wave optical simulations (FDTD method, Lumerical Inc.) to simulate the local electric field enhancement and the corresponding photoabsorption in more realistic device geometries. Instead of solving for the potential in these structures, the internal electric field is determined numerically, because the relationship between the position and momentum operators allows for a matrix element that depends on the internal electric field $\overrightarrow{E}$ only,

$$\langle \Psi_{\mathrm{f}}(r)|r\overrightarrow{E}|\Psi_{\mathrm{i}}(r)\rangle = \frac{j\hbar\overrightarrow{E}}{m(\varepsilon_{\mathrm{f}}-\varepsilon_{\mathrm{i}})}\langle \Psi_{\mathrm{f}}(r)|\hat{p}|\Psi_{\mathrm{i}}(r)\rangle \qquad (2.9)$$

where j is the imaginary unit, and $\hat{p}$ is the momentum operator. The optical power conversion from the devices was then analyzed using the same procedure as for the idealized geometries

studied above but with the calculated absorption profiles. The modeled devices structures and the corresponding optical absorption spectra are depicted in Figure 2.10. The spatially integrated spectral absorption by each individual electrode is also displayed in order to emphasize which wavelengths of illumination preferentially excite one nanoelectrode more than the other. Since plasmonic nanostructures have significant local electric field enhancement at sharp corners, known as hot spots, a tunnel junction consisting of a $20\,\mathrm{nm}$ thick triangle-shaped gold nanoelectrode ($\mathrm{Au1}$) was selected that exhibits greater electric field concentration at the sharp tip compared with the flat edge of a rectangular counter-electrode ($\mathrm{Au2}$) separated by $1\,\mathrm{nm}$. This design is optimized to promote current flow from the region of high absorption in the sharp tip to regions of low absorption in the rectangular counter-electrode.

Several resonant features are observed in the absorption spectra, with a red-shift and more complex broadening observed when the structure is coated with $\mathrm{TiO_2}$. Our calculations of the optical power conversion efficiency considered excitation wavelengths that maximized the amount of absorption in one electrode compared to the other, in order to understand the device response under conditions when electrons do not absorb light equally. For the $\mathrm{Au-Vacuum-Au}$ junction these wavelengths are $585\,\mathrm{nm}$ and $785\,\mathrm{nm}$, and for the $\mathrm{Au-TiO_2-Au}$ junction these wavelengths are 658 and $707\,\mathrm{nm}$. Figure 2.10(b, f) show the local electric field enhancement at these excitation wavelengths in the region centered on the gap. It should be noted that there is no fundamental reason that the calculations cannot be expanded to analyze gold nanoelectrodes with larger size. However, as discussed in previous section, that the simulation cost would increase significantly with the increasing physical dimensions, because the matrix elements require calculations between all two-state combinations, and the number of states increases tremendously with the volume of the metal. It should also be noted that even though these incident wavelengths were selected because they are absorbed preferentially by one electrode in the junction, we still observed stronger local electric field concentration at the sharp tip of the triangular electrode regardless of the incident wavelength, as would be preferred for broadband optical power conversion. Indeed, current flows from the triangular electrode to the rectangular electrode for all incident wavelengths simulated.

The optical power conversion efficiency was calculated by normalizing the maximum output power by the incident optical power that was absorbed by the entire structure. While stronger electric field enhancement was calculated when the $\mathrm{Au-Vacuum-Au}$ junction is illuminated by $785\,\mathrm{nm}$ compared to $585\,\mathrm{nm}$ monochromatic irradiation, the power conversion efficiency shows little wavelength dependence. The energy barrier for classically injection is large compared with the energy of electrons that absorb either wavelength of light, and hence the probability of tunneling is greater for electrons excited to higher energy states with $585\,\mathrm{nm}$ light. The higher tunneling probability compensates for the lower absorption rate compared with excitation at $785\,\mathrm{nm}$. In contrast the power conversion efficiency calculated for the $\mathrm{Au-TiO_2-Au}$ junction at a wavelength of $658\,\mathrm{nm}$ versus $707\,\mathrm{nm}$ (Figure 2.10(h)) indicates a strong dependence on wavelength. When the $\mathrm{Au-TiO_2-Au}$ junction is illuminated by $707\,\mathrm{nm}$ irradiation, greater efficiency (20.2%) is achieved compared to $658\,\mathrm{nm}$ illumination (16.84%). In this device the barrier height of the $\mathrm{Au-TiO_2-Au}$ junction is reduced to $1\,\mathrm{eV}$, which is smaller than the incident photon energy. Therefore, rather than tunneling, a greater portion of electrons are photoemitted, and the current density more directly indicates the local field enhancement and photoexcitation rate.

In this section, we have developed a theoretical model that accounts for electron tunneling, photoemission, and thermionic emission across tunneling junctions defined by plasmonic metal nanostructures that absorb light asymmetrically. The roles of photothermal heating and non-thermal carrier excitation are analyzed separately, and our results indicate that both effects interact cooperatively to promote an electrical current from the electrode with greater local field concentration to the electrode with less field concentration. When only optically induced thermal gradients are considered, electron tunneling dominates transport across the junction near room temperature. Furthermore, full wave optical simulations of more realistic device geometries show that the direction of the induced current flow is independent of excitation wavelength across the visible spectrum. Up to 20% power conversion efficiency is achieved in a modeled $\mathrm{Au-TiO_2-Au}$ device structure under $707\,\mathrm{nm}$ monochromatic illumination with an intensity of $1000\,\mathrm{W/m^2}$ when the junction is subject to a thermal gradient of $\Delta T = 10\,\mathrm{K}$. We believe these results will inform strategies for

more efficient device implementation of optical power converters based on plasmonic absorption in metals.

2.4 Conclusion

In this chapter, we reviewed a free-electron jellium model that calculate the non-thermal carrier production rate in plasmonic metals. We applied this model to gold nanocubes, where the electronic states are fully quantized, and a more realistic scenatio, a film-like plasmonic structure. We observed the same size-dependence as many reserachers calculated for nanostructures with different shapes, that larger nanoparticles produce less energetic carriers and vice versa. Therefore, smaller nanoparticles are prefered in plasmon-mediated hot carrier devices not only because smaller nanoparticles have greater absorption efficiency but also the non-thermal carriers have greater energy in smaller nanoparticles, thus have better catalytic performance. In addtion, the temperature-dependece of non-thermal carriers is realized, we found that the ratio of high-energy excited carriers and Drude-like carriers decreases with temperature.

To address the challenge that not all excited carriers are collected due to insufficient energy compared to surface potential barrier. We developed a theoretical model which describes the quantum tunneling phenomena of carriers inside a metal. Within the quantum tunneling region, we are able to collect carriers that were otherwise wasted as heat classically. We further envisioned an asymmetric plasmonic tunneling junction to more fully utilize both thermal- and photo- excited plasmonic carriers. The asymmetric tunneling junction concentrates light preferentially on one nanoelectrode than the other, both the uneven photothermal effect and non-thermal carrier generation perturb the electron distribution asymmetrically. A 20% power conversion efficiency is predicted for an asymmetric $\mathrm{Au} - \mathrm{TiO_2} - \mathrm{Au}$ junction under solar flux illumination. Our results provide insights toward plasmonic carrier generation and collection, and shall guide the design of better plasmonic carrier devices.

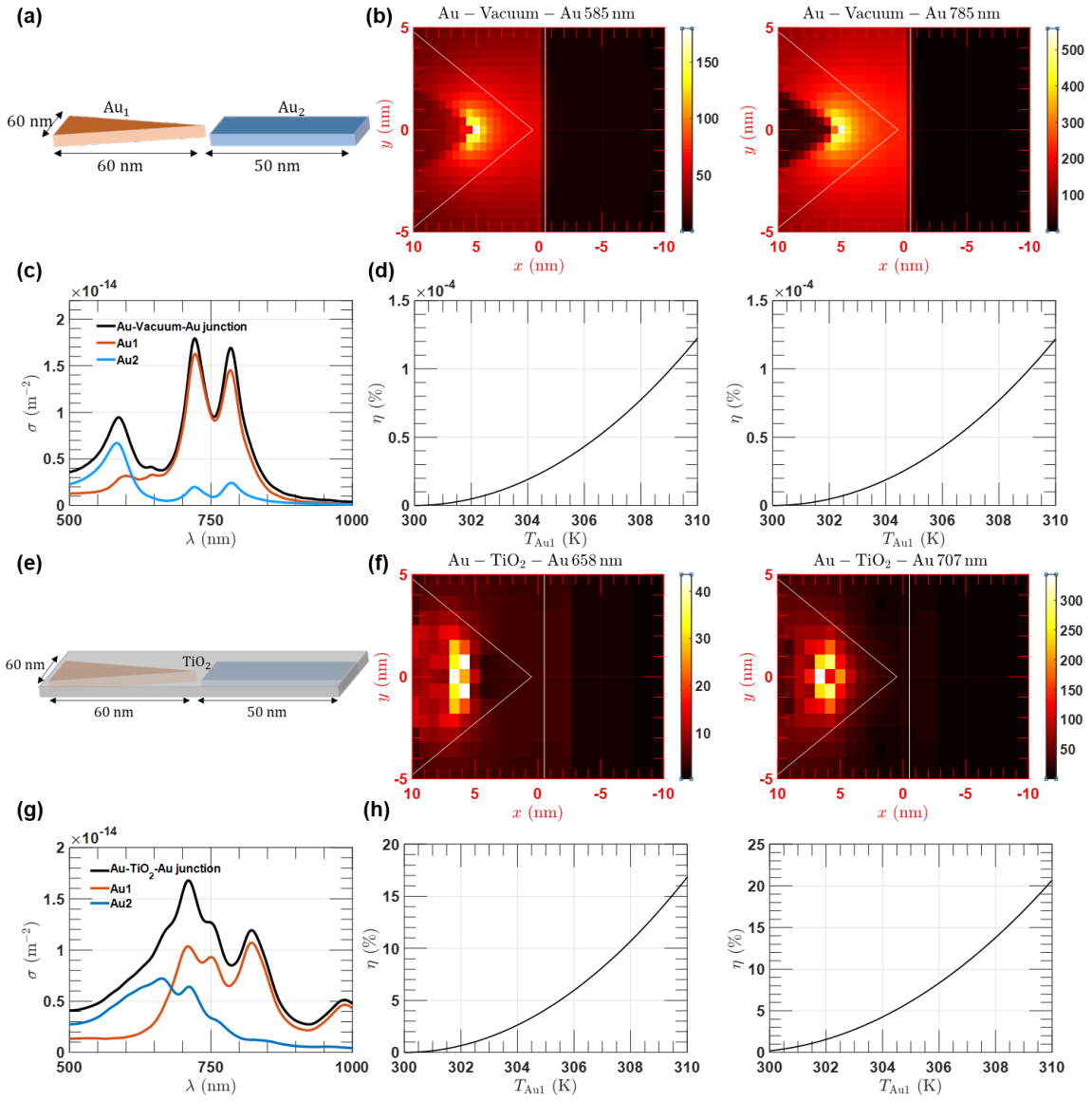

Figure 2.10: (a) Schematic view of a $\mathrm{Au-Vacuum-Au}$ device and (b) the corresponding electric field enhancement map of the $20\,\mathrm{nm} \times 10\,\mathrm{nm}$ junction region for illumination at $585\,\mathrm{nm}$ (left) and $785\,\mathrm{nm}$ (right). (c) Calculated absorption spectrum (black) for the device in (a) with the spatially integrated absorption by electrode $\mathrm{Au1}$ (red) and electrode $\mathrm{Au2}$ (blue). (d) Estimated conversion efficiency for $585\,\mathrm{nm}$ illumination (left) and $785\,\mathrm{nm}$ illumination (right). (e) Schematic view of a $\mathrm{Au-TiO_2-Au}$ device and (f) the corresponding electric field enhancement map of the $20\,\mathrm{nm} \times 10\,\mathrm{nm}$ junction region for illumination at $658\,\mathrm{nm}$ (left) and $707\,\mathrm{nm}$ (right). (g) Calculated absorption spectrum (black) for the device in (e) with the spatially integrated absorption by electrode $\mathrm{Au1}$ (red) and electrode $\mathrm{Au2}$ (blue). (h) Estimated conversion efficiency for $658\,\mathrm{nm}$ illumination (left) and $707\,\mathrm{nm}$ illumination (right). All calculations are for an optical power density of $1000\,\mathrm{W/m^2}$. Adapted with permission from Wu and Sheldon[9]. Copyright 2018 by ACS Publications.

3. RAMAN SCATTERING FROM PLASMONIC METALS AND HOT CARRIER ENERGY DISTRIBUTION UNDER STEADY STATE

3.1 Light Emission from Plasmonic Metals

Emission from plasmonic nanoparticles has been the focus of considerable recent research [10,102] because of its contribution as a broad background to surface-enhanced Raman spectra (SERS) [11,103] and its possible applications in imaging [104] and nanothermometry. [12,105] Compared to semiconducting nanoparticles, light emission following photoexcitation of plasmonic nanostructures is more complex due to ultrafast electron-electron and electron-phonon interactions [58] as well as the involvement of the collective oscillations of conduction band electrons, known as localized surface plasmons. Nanoparticle plasmons significantly enhance the extremely low emission quantum yield of bulk metal (quantum yield $\sim 10^{-10}$) [106,107] and determine their spectral line shape. [108] However, the exact mechanism underlying plasmonic nanoparticle emission remains heavily debated. While the enhancement by surface plasmons is well accepted, the main point of contention is the interpretation of the emission as photoluminescence (PL) versus electronic Raman scattering. *

PL occurs through radiative recombination of hot carriers during their interactions with electrons and phonons. The PL spectrum and intensity depend on the excitation wavelengths and on the localized surface plasmons which act as antennas for radiation into the far-field. [109] Recently, Cai et al. [10] showed through experiments and theory that the emission of gold nanorods (AuNRs) at the plasmon resonance is consistent with a Purcell effect enhanced hot carrier recombination of inter-and intraband transitions (Figure 3.1). The plasmon resonance of the AuNRs increases the photonic density of states (PDOS) [110] and thus enhances the quantum yield (QY) and shapes the emission spectrum.

The second proposed mechanism for plasmonic nanoparticle emission is based on electronic Raman scattering. [11,111] Electronic Raman scattering is the coherent inelastic scattering of light

*Section 3.2 is adapted with permission from Wu, S.; Hogan, N.; Sheldon, M., Hot Electron Emission in Plasmonic Thermionic Converters. *ACS Energy Letters* **2019**, 4 (10), 2508-2513. Copyright 2019 ACS Publications.

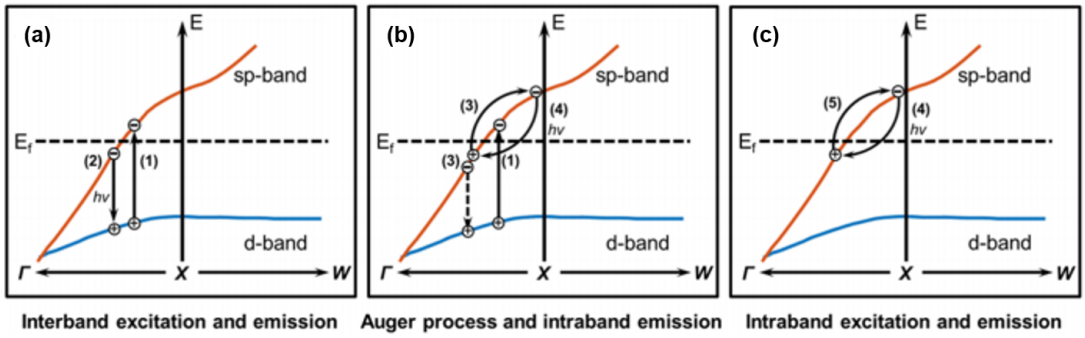

Figure 3.1: PL in AuNRs can originate from three possible sources: (a) interband excitation (1) and interband emission (2); (b) interband excitation (1), Auger process leading to the decay of d-band holes and excitation of sp-band electrons (3) and intraband emission (4); or (b) intraband excitation (5) and intraband emission (4). Adapted with permission from Cai et al.[10]. Copyright 2018 by ACS Publications.

from electrons. In a single scattering event, only one intermediate state is considered and the emission stops after dephasing (Figure 3.4). In contrast, for PL the initially created excited state can undergo momentum and energy changes through electron-electron and electron-phonon scattering before a photon is emitted.[112]

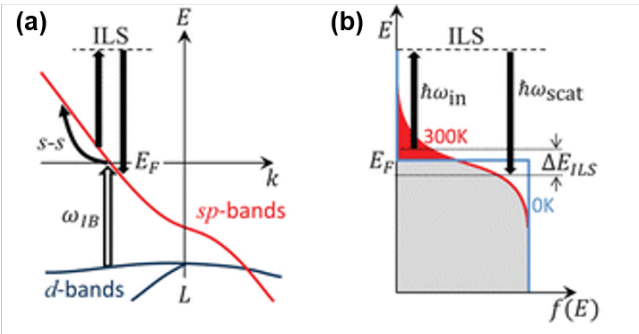

Figure 3.2: (a) Band diagram of Au around the L point, showing absorption from d to s bands only for $\omega > \omega_{\mathrm{IB}}$, intraband scattering ($\mathrm{s}-\mathrm{s}$) and inelastic light scattering (ILS). (b) Origin of anti-Stokes scattering background produced by ILS from the thermally excited electrons above the Fermi level (shaded red). Plasmonically coupled light excites these electrons to a virtual state where they relax down to empty states just below the Fermi energy, emitting blue-shifted (anti-Stokes) light. Adapted with permission from Hugall and Baumberg[11]. Copyright 2015 by ACS Publications.

Regardless of the microscopic mechanism, the spectral-dependent intensity of the anti-Stokes spectrum has been established as an accurate indicator of temperature.[12,105] Recently, Xie and Cahill[12] measures the steady-state Raman spectra of gold nanodisk and they attribute the spectra of inelastically scattered light to Raman scattering by a thermal distribution of electron-hole pairs. Under this picture, the spectral intensity $\mathrm{S}(\Delta\omega)$ (Raman signals per unit integrating time) scales with the electron-hole occupation number (Figure 3.3)

$$n(\Delta\omega) = \frac{1}{\exp(-hc\Delta\omega/k_{\mathrm{B}}T_{\mathrm{Au}}) - 1} \qquad (3.1)$$

where h is Plank's constant, c is the speed of light, $\Delta\omega$ is the wavenumber (negative for anti-Stokes), and T_{Au} is the temperature of Au nanodisk.

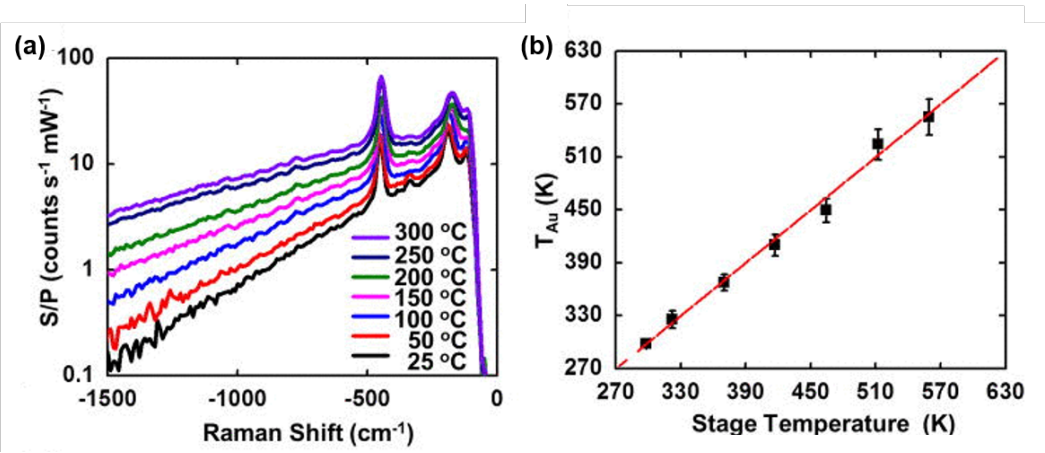

Figure 3.3: (a) Anti-Stokes electronic Raman scattering spectra collected from arrays of nanodisks as a function of substrate temperature. The y-axis is the spectral density of the intensity S of scattered light normalized by the excitation laser power. (b) Comparison between the temperature extracted from the fit and the temperature of the heating stage. Adapted with permission from Xie and Cahill[12]. Copyright 2016 by AIP Publishing.

Figure 3.3(b) shows the temperatures extracted from the fits of the data using eq 3.1 in comparison with the temperature of the heating state. The good agreement validates the approach based on eq 3.1. We shall see in this chapter that the Raman scattering from plasmonic metals tells the

story of hot carrier evolution.

3.2 Anti-Stokes Raman Spectroscopy of Patterned Gold Nanoarrays and Two-Temperature Model

3.2.1 Sample Fabrication

To prepare the nanostructures, a $5\,\mathrm{nm}$ Cr sticking layer followed by a $150\,\mathrm{nm}$ Au thin film were deposited using thermal deposition (Lesker PVD e-beam evaporator) on a commercially available silicon TEM grid with a $50\,\mathrm{nm}$ $\mathrm{Si_3N_4}$ membrane windows (Ted Pella). A layer of PMMA/MMA 9% in ethyl lactate (MicroChem) followed by a layer of 2% PMMA in anisole (MicroChem) were spin coated to form a bilayer resist. Electron beam lithography was performed using a Tescan FE-SEM instrument. A top Au layer was deposited followed by removal of the polymer mask in acetone.

3.2.2 Raman Spectroscopy

Anti-Stokes Raman spectra were collected using a confocal Raman microscope (Witec RA300) with samples in a vacuum heating microscope stage (Linkam TS1500VE) attached to a vacuum pump. Vacuum experiments were performed at a pressure of $0.011\,\mathrm{mbar}$. Samples were illuminated by a $\mathrm{Nd:Yag}$ laser at $532\,\mathrm{nm}$ and focused on the sample using a $20\times$ objective with a 0.4 NA. Reflection spectra were taken by using the same stage setup with a white light source. The measured reflection signal was normalized to the source spectrum to give the reflectance of the surfaces.

3.2.3 Result and Discussion

Top-down lithographic techniques were used to fabricate a $90\,\mu\mathrm{m}$ square array of $225\,\mathrm{nm} \times 225\,\mathrm{nm} \times 100\,\mathrm{nm}$ gold nanocubes at a pitch of $500\,\mathrm{nm}$ on a $150\,\mathrm{nm}$ thick gold film, as displayed in Figure 3.4(b). The scanning electron microscope (SEM) and optical images are displayed in Figure 3.4(a,c). At the excitation wavelength ($532\,\mathrm{nm}$) there is an approximate two-fold increase in absorption compared with a gold thin film (Figure 3.4(d)) leading to increased photo-thermalization localized in the nanocubes.

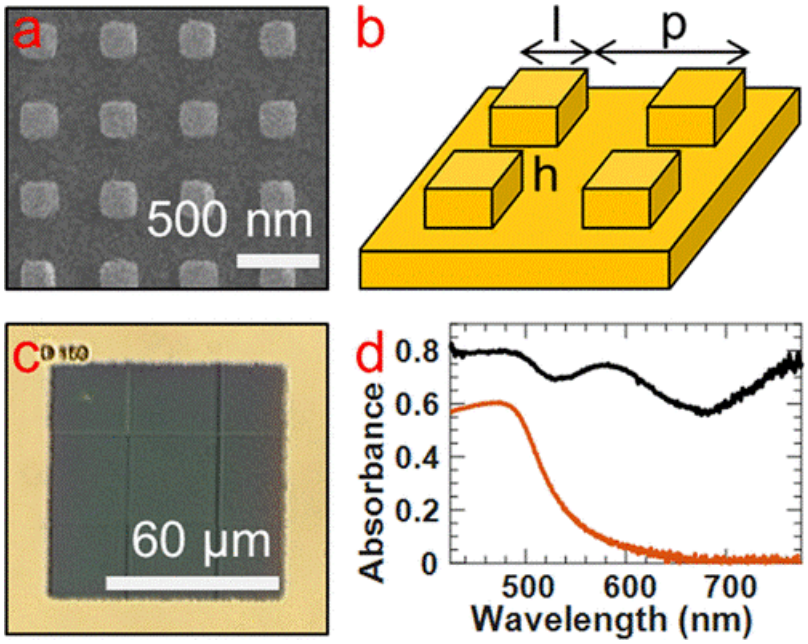

Figure 3.4: (a) SEM image of the fabricated nanostructure. (b) Schematic of the unit cell with $l = 225\,\mathrm{nm}$, $p = 500\,\mathrm{nm}$, and $h = 100\,\mathrm{nm}$ on a $150\,\mathrm{nm}$ thick gold film. (c) Optical image of the fabricated nanostructure. (d) Absorbance of the nanostructure (black) compared with a smooth gold thin film with a thickness of $150\,\mathrm{nm}$ (red). Adapted with permission from Wu et al.[13]. Copyright 2019 by ACS Publications.

Temperature measurements during photothermalization were achieved by collecting anti-Stokes Raman spectra under $532\,\mathrm{nm}$ continuous-wave (CW) laser illumination. A representative anti-Stokes spectrum is shown in Figure 3.5(a). The signal from the nanostructure is ten times larger than that from a gold thin film, comparable to enhancements observed in surface-enhanced Raman studies.[113] Fitting our data to eq 3.1 (Figure 3.5, red dotted) proves inadequate because there is a large signal at high-energy Raman shifts greater than $-2000\,\mathrm{cm}^{-1}$ that is not well described by the Bose-Einstein distribution. However, by adapting the method of Szczerbiski et al.[114] our data are readily described if additional terms are included to account for a subpopulation of hot electrons, χ, with an energy distribution at an elevated temperature, T_e.

$$\mathrm{S}(\Delta\omega) = \mathrm{C} \times \mathrm{D}(\Delta\omega) \times \left(\frac{1-\chi}{\exp(-hc\Delta\omega/k_\mathrm{B}T_\mathrm{l}) - 1} + \frac{\chi}{\exp(-hc\Delta\omega/k_\mathrm{B}T_\mathrm{e}) + 1} \right) \tag{3.2}$$

where C is the scaling factor to account for the experimental collection efficiency that is recalibrated for each measurement. In addition, the signal intensity is proportional to the density of optical states, $\mathrm{D}(\Delta\omega)$, obtained from the reflection spectrum.

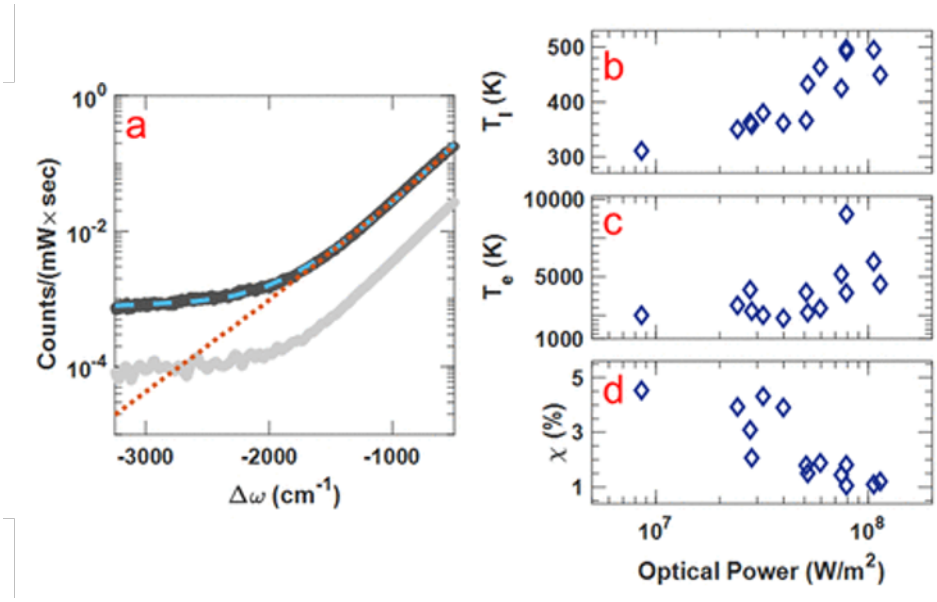

Figure 3.5: (a) Measured anti-Stokes Raman signal from the nanostructure (solid black) and gold film (solid gray) in atmosphere, both collected under $7.3 \times 10^9\,\mathrm{Wm^{-2}}$ 532nm laser excitation. The fit to a one-temperature model (eq 3.1, red dotted line) and a two-temperature model (eq 3.2, blue dashed line) are shown. The one-temperature fit gives $T_\mathrm{l} = 459\,\mathrm{k}$, whereas the two-temperature fit gives $T_\mathrm{l} = 430\,\mathrm{K}$, $T_\mathrm{e} = 10040\,\mathrm{K}$, and $\chi = 0.34\%$. The TTM fit for (b) lattice temperature, (c) electronic temperature and (d) the percentage of hot electrons for the nanostructure under vacuum. Adapted with permission from Wu et al.[13]. Copyright 2019 by ACS Publications.

The magnitude of χ in the steady state depends on both the generation rate of hot electrons due to optical excitation and the relaxation rate as electrons equilibrate to T_l via phonon scattering. Those carriers in thermal equilibrium with the lattice follow Bose-Einstein statistics, whereas the high-energy tail of the Raman signal is described by Fermi-Dirac statistics.[115] The fit to this two-temperature model (TTM) (Figure 3.5(a), blue dashed line) is excellent for all optical powers probed, spanning 10^7 to $10^{11}\,\mathrm{Wm^{-2}}$. However, it should be noted that the hot electron signal is fairly weak compared with the signal from the thermalized electron bath. Eliminating other

sources of error and artifacts such as room lights as well as long integration times is required to obtain a good signal. We also cannot fully discount other small effect contributing to the signal that may result from changes in the optical response with temperature, such as shifts in the plasmon resonances of the nanostructures, due to volume expansion.

The dependence of T_l, T_e, and χ on optical power for the nanostructure was determined by analyzing the Raman spectra using eq 3.2. Samples were measured under vacuum ($0.01\,\mathrm{mbar}$). The fitted data are summarized in Figure 3.5(b-d). Melting and degradation of the samples occurred when the fitted T_l significantly exceeded $\sim 600\,\mathrm{K}$ in vacuum. We observed a monotonic increase in T_e and T_l as the optical power increased, with T_e in excess of T_l by at least an order of magnitude. This trend is expected due to the lower heat capacity of the electron gas,[116] and the values we measure for T_e and T_l are similar to those reported in transient absorption (TA) experiments[111] for comparable optical powers.

A unique capability of our experiments that cannot be readily achieved in pulsed TA studies is the quantification of the size of the hot electron population, χ. An analysis of χ from our fitted spectra therefore provides important new information about how the availability of hot electrons depends on optical power and temperature under CW illumination that is more directly comparable to operating conditions for emerging hot-electron-based technologies. Interestingly in all experiments, we observe a clear inverse correlation between T_e and χ as optical power increases. One may initially expect that increases in optical power would lead to a greater rate of electronic excitation and thus a larger steady-state population of hot electrons. We hypothesize that the opposite behavior is due to the increase in electron-phonon coupling as temperature increases, providing faster relaxation of the hot electrons that overwhelms the increase in the excitation rate. As we shall later see in Chapter 4 that this inversely correlation between T_e and χ is supported by an independent electric current measurement.

3.3 Stokes Raman Scattering and Dephase of Localized Surface Plasmon

The coupling of light to molecular vibrations is strongly modified when they are placed near a plasmonic metal surface, with the appearance of a strong broad continuum background in addition

to the normal surface-enhanced Raman scattering (SERS). Similarly to anti-Stokes scattering, there have been strong debates over the origin of the SERS signal and a variety of mechanisms for this effect have been proposed.[117–120] For instance, Barnett et al.[14] proposed that the origin of this spectrally broad background is due to interaction of molecule on the plasmonic surface and its image molecule as depicted in Figure 3.6. The two molecules (real and its image) interact with the exponentially localized surface plasmon resonance to produce the Raman spectrum. The physical picture can be thought of as two oscillators (vibrating at the frequency of their excited molecular vibrational mode), coupled by the dipole-dipole interaction. Though the image-molecule approach is able to explain the spectral background, there is few connections between the image-molecule model and experimental studies. Furthermore, the image-molecule model predicts a narrow sharp peak associated with a normal SERS line, which is not observed.

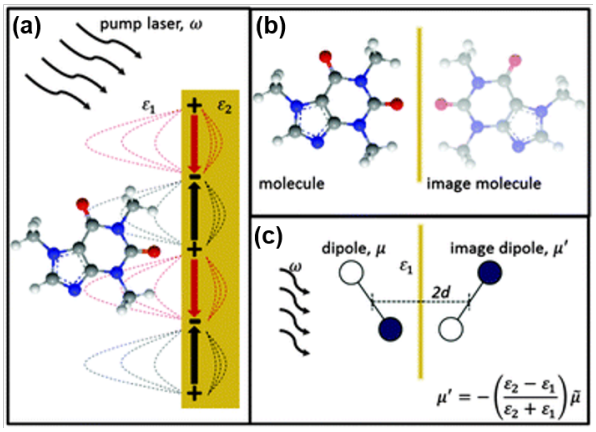

Figure 3.6: Representation of method of images approach with (a) real molecule interacting with a plasmonic metal surface replaced by (b) a real-molecule-image-molecule interaction. (c) Dominant molecular vibrating bond of real and image molecules now represented by dipoles. Real and image dipoles separated by distance, $2d$, and ω is the exciting laser field. Adapted with permission from Barnett et al.[14]. Copyright 2014 by PCCP Owner Societies.

Alternatively, Otto et al.[121] proposed a very simple model allows fitting the background on both Stokes and anti-Stokes side. The model assumes a density of electrons and holes g in a Lorentzian

band

$$g(E) = \frac{1}{\pi} \frac{\gamma}{(E - E_F)^2 + \gamma^2} \qquad (3.3)$$

centered at the Fermi energy E_F, and γ is the width of the Lorentzian. The values of γ can be obtained from least-square fits to the experimental curves. The distribution of electrons and hole is given by the Fermi-Dirac distribution $f(E)$. Then the joint density of states $J(\hbar\omega)$ of electron-hole pairs at an energy of $\hbar\omega$ is given by

$$J(\hbar\omega) = \int g(E) f(E) g(E + \hbar\omega)(1 - f(E + \hbar\omega)) dE \qquad (3.4)$$

Within this model the spectral yield of Raman scattering by electron-hole-pair excitation in the metal is assumed to be proportional to $J(\hbar\omega)$. We note that eq 3.3 and eq 2.1 are both a Lorentzian distribution function, and eq 2.1 is the jellium model described the energy distribution of non-thermal carriers, the γ is then determined by the plasmon dephasing time. We show that the energy distribution directly after the initial excitation can be approximated using a simple Lorentzian distribution (Figure 3.7).

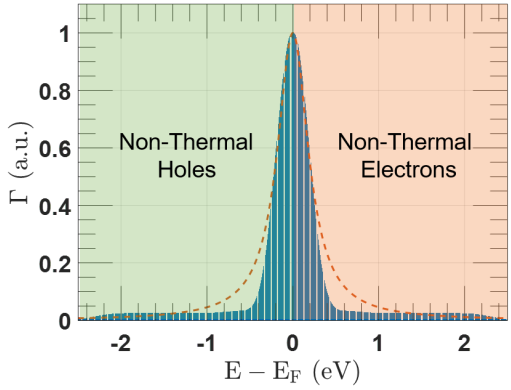

Figure 3.7: Energy distribution of non-thermal carriers calculated using eq 2.1 (blue bar) and a Lorentzian function with width τ^{-1} (red dashed line). The calculation is assumed a 10 nm thickness gold slab at absolute zero.

Since we have shown the energy distribution of non-thermal carriers, $\Gamma(E,\tau)$, can be approximated using a simple Lorentzian function with width controlled by τ^{-1}. We then attribute the electronic Raman scattering to the scattering from non-thermal carriers (Figure 3.8), which gives us the ability to correlate plasmon dephasing information with Raman spectrum (eq 3.5a). It is noted that the proposed model is naturally compatible with our recently developed two-temperature Raman thermometry which assumes only a subpopulation (χ) of hot carriers is excited at T_e (eq 3.5b).

$$J(\hbar\omega) = D\int \Gamma(E,\tau)f(E)\Gamma(E+\hbar\omega,\tau)(1-f(E+\hbar\omega))dE \qquad (3.5a)$$

$$J(\hbar\omega) = D\int \Gamma(E.\tau)[(1-\chi)f(E,T_l)+\chi f(E,T_e)]$$

$$\Gamma(E+\hbar\omega,\tau)(1-[(1-\chi)f(E,T_l)+\chi f(E,T_e)])dE \qquad (3.5b)$$

where $\Gamma(E,\tau)$ is a Lorentzian function describing the energy distribution of non-thermal carriers with width controlled by the plasmon dephasing time τ, and D is the scaling factor accounts for the collection efficiency for our setup.

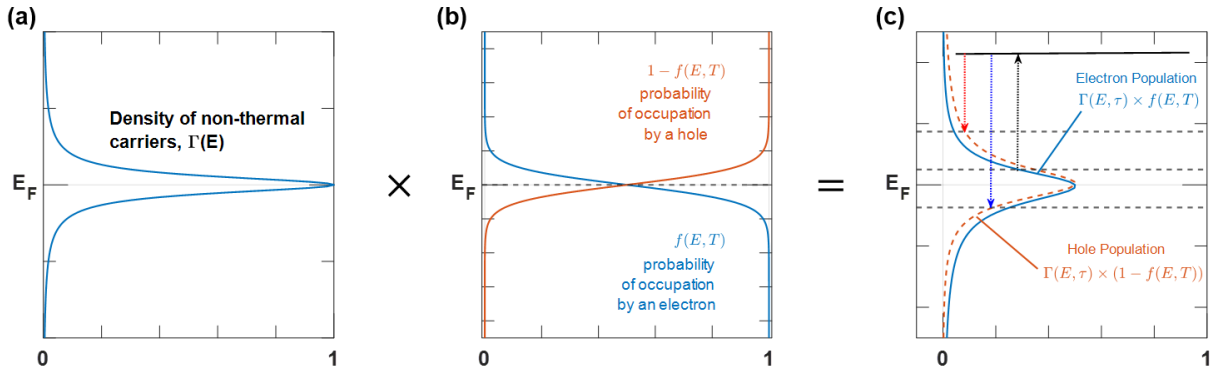

Figure 3.8: Inelastic light scattering from non-thermal carriers. Density of states of the non-thermal carriers in a metallic nanostructure (a), multiplied by the Fermi-Dirac probability of occupation by an electron/hole (blue/red line in b), gives the populations of electrons (blue line in c) and holes (red dashed line in c).

We then show eq 3.5 can be used to explain the experimental measured Raman scattering

from plasmonic nanostructures, and we are able to extract both material temperature and plasmon dephasing time.

To demonstrate the validity of proposed model (eq 3.5), a series of Raman spectra were collected in thermal stage at different temperatures (Figure 3.9). A $532\ \mathrm{nm}$ laser is used to excite the Raman scattering from patterned gold nanostructures with optical power density of $1.27 \times 10^8\ \mathrm{W/m^2}$. In consistent with our previous two-temperature Raman thermometry, two slopes are observed in the anti-Stokes side indicating two temperature present in gold nanostructures. We attributed the first slope ($-700\ \mathrm{cm^{-1}}$ to $-1200\ \mathrm{cm^{-1}}$) to lattice temperature T_l, and the second slope at higher energy ($-1200\ \mathrm{cm^{-1}}$ to $-4000\ \mathrm{cm^{-1}}$) to electronic temperature T_e. Interestingly, the Stokes scattering decreases with temperature while the anti-Stokes scattering rises with temperature. Since the Raman scattering scaled with joint density of states (eq 3.5), the decrease of Stokes scattering indicates the reduced contribution from non-thermal carriers. Additionally, we observed the appearance of a vibrational peak at $1580\ \mathrm{cm^{-1}}$, which is attributed to the G band of graphite-like material, during the course of measurement (heating from $298\ \mathrm{K}$ to $448\ \mathrm{K}$). This is because the presence of a subpopulation of hot carrier at elevated T_e plays an important role in reducing adsorbed carbon-related molecules during the measurement.[122]

Since the subpopulation of T_e is relatively small ($\sim 1\%$) compared to the contribution from T_l, we first used eq 3.5a to fit our Raman spectra (Figure 3.9(b,c)). There are three fitting parameters in eq 3.5a, the scaling factor D, lattice temperature T_l in Fermi-Dirac distribution as well as the plasmon dephasing time, τ. The fitting range is from $-1200\ \mathrm{cm^{-1}}$ to $3000\ \mathrm{cm^{-1}}$ to capture not only the one-temperature slope in Anti-Stokes side but also the broad Stokes background. As shown in Figure 3.9(b,c), the three-variable fitting process yielded good agreement between theory and experiment.

To demonstrate the fitting performance, we compared the fitted temperature with thermal stage temperature as shown in Figure 3.10(a). The fitted lattice temperature (red dots) is consistent with stage temperature (black dashed line) validating our proposed model. The slightly deviation from stage temperature is due to photothermal heating. In addition to lattice temperature, another fea-

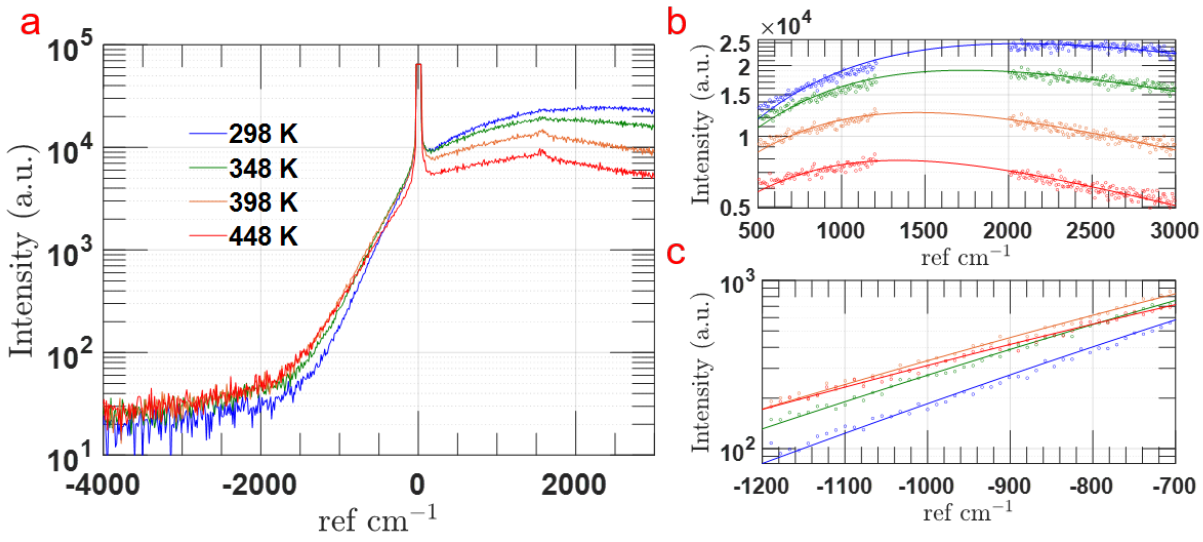

Figure 3.9: (a) Raman spectra of patterned gold nanostructures recorded at different temperature, and experiment (dots) and theory (solid lines) on (b) Stokes side and (c) Anti-Stokes side. To achieve better fitting, the 1200 cm^{-1} to 2000 cm^{-1} containing the vibration peak of carbon-species is neglected in fitting.

ture extracted from fitting is the plasmon dephasing time (Figure 3.10(b)). The extracted plasmon dephasing time, τ, is smaller than 10 fs and is consistent with reported value in ultrafast studies.[123] Furthermore, the monotonically increase of plasmon dephasing time during the course of measurement is possibly due to the formation of graphite-like material on the surface, which modifies the dephase mechanism through chemical interface damping (CID).

Another measurement is conducted to confirm that the change of plasmon dephasing time is not only due to changed temperature but also due to the modified chemical interface. We used another patterned gold nanostructures and recorded the Raman spectra at varied optical power density. Since the subpopulation of hot carriers at T_e is small at steady state as proved in the fitting result in Figure 3.10. We first repeated the temperature-dependence study in the same manner with much lower optical power density (6.4×10^7 $\mathrm{W/m^2}$), and we restricted our scope from -1500 cm^{-1} to 3000 cm^{-1} in order to obtain better resolution in Raman shift. We then analyzed the Raman spectra collected at varied optical power density, and the result of both temperature and power dependence study is shown in Figure 3.11(a,d).

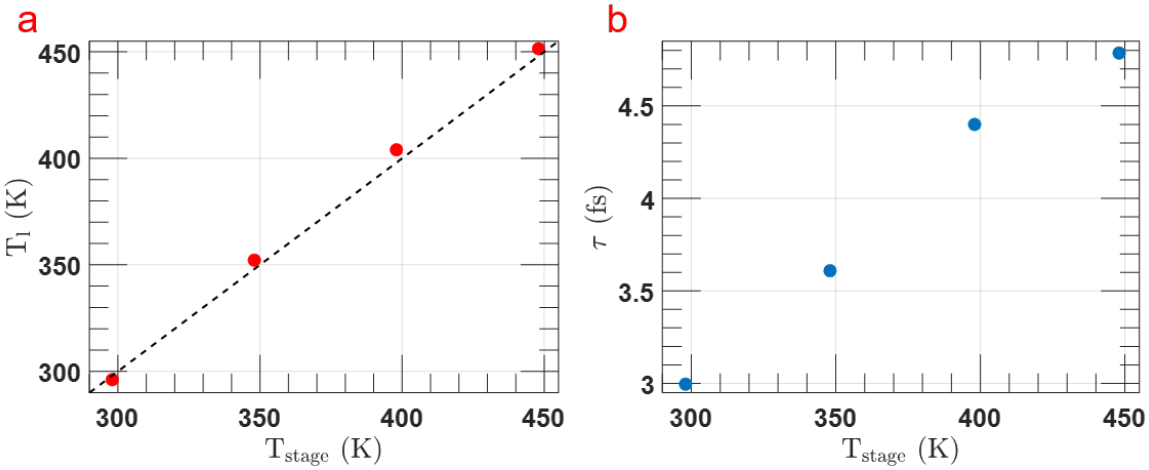

Figure 3.10: (a) Fitted temperature (red dots) and stage temperature (black dashed line), (b) Extracted plasmon dephasing time vs. stage temperature.

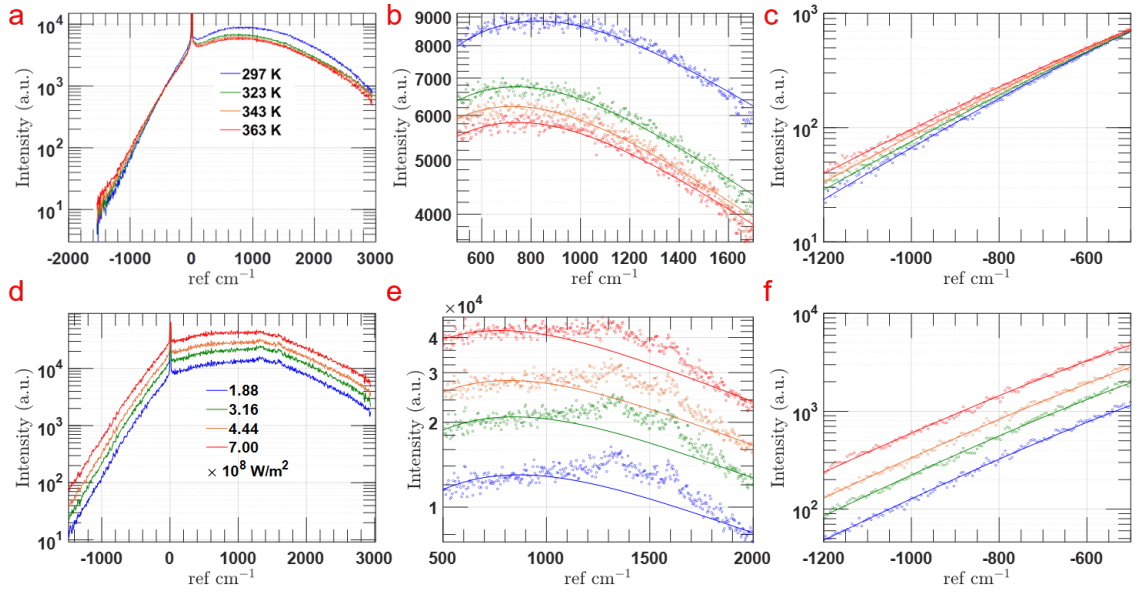

Figure 3.11: (a) Raman spectra of patterned gold nanostructures recorded at different temperature, experiment (dots) and fitted equation (solid line) in (b) Stokes side and (c) Anti-Stokes side, (d) Raman spectra of patterned gold nanostructures recorded at different optical power, experiment (dots) and fitted equation (solid line) in (e) Stokes side and (f) Anti-Stokes side.

Since the optical power used to collect the temperature-dependence Raman spectra (Figure 3.11(a)) is much weaker than the optical power used in Figure 3.11(d), we observed no vibrational

peaks due to formation of carbon species located at $1350\ \mathrm{cm}^{-1}$ (D band) and $1580\ \mathrm{cm}^{-1}$ (G band) as shown in Figure 3.11(b). In contrast, the formation of carbon species in power dependence study (Figure 3.11(e)) indicates the contribution from excited hot carriers, similar behavior is observed in Szczerbiski et al.[114]. Using the same fitting equation, we show a good agreement between theory and experiment (Figure 3.11(b,c,e,f)).

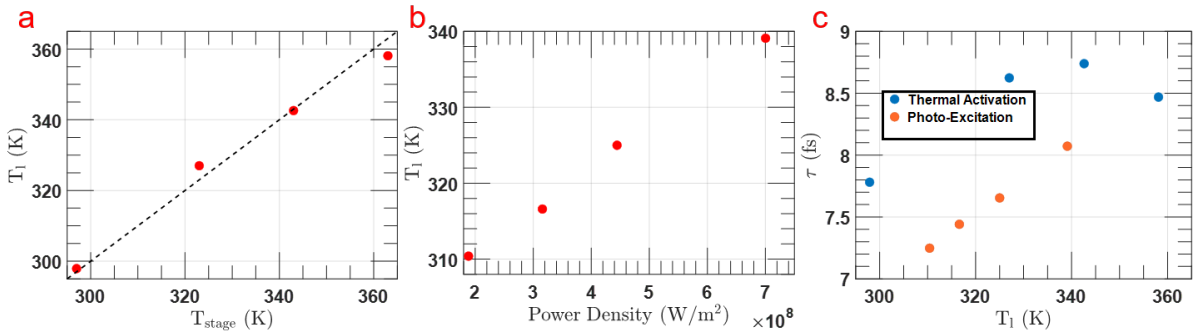

Figure 3.12: (a) Correlation between fitted temperature (red dots) and stage temperature (black solid line), (b) Extracted lattice temperature vs. optical power, (c) Comparison of plasmon dephasing time solely due to thermal activation (blue dots) or due to photo-excitation (red dots).

The fitted result of both temperature and power dependence study is summarized in Figure 3.12. Similar as previously fitted result, the good correlation between fitted temperature (red dots) and stage temperature (black dashed line, Figure 3.12(a)) further validates the model. In addition, we observed a monotonically increased lattice temperature with incident optical power (Figure 3.12(b)) expectedly. The optical power is chosen so that samples are photo-thermal heated to a similar temperature range as in temperature-dependence study. The extracted plasmon dephasing time is depicted in Figure 3.12(c) for both thermal-activation and photo-excitation. Since the contribution of hot carriers is significant in power-dependence study compared to temperature-dependence study, the appearance of D band and G band of carbon species is only observed in power-dependence study (Figure 3.11(e)). The modified surface due to adsorbed carbon species introduced the chemical interface damping, the directly coupling between surface plasmon and

molecular orbitals, which resulted in a reduced plasmon dephasing time.

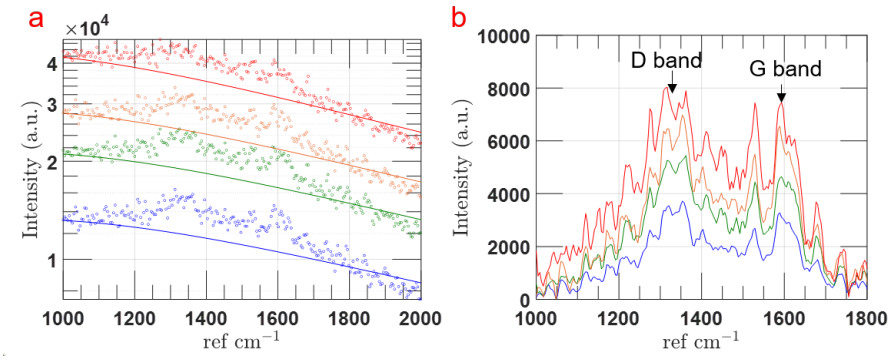

Figure 3.13: (a) Experiments (dots) and theory (solid line) of Raman spectra recorded at different power, the power is increased from blue to red. (b) Background-subtracted vibrational peaks of amorphous carbon species on surface.

Furthermore, the theory we developed is able to not only resolve the plasmon dephasing information at steady state but also subtract the continuum background on Stokes side to reveal the vibrational fingerprint of chemical species, thus is useful in monitoring chemical reactions *in situ* using SERS application. For instance, by subtracting the fitted curve (solid line, Figure 3.13(a)), the vibrational peaks of D and G bands of carbon species is easily resolved (Figure 3.13(b)).

3.4 Conclusion

In this chapter, we discussed the debate over the origin of light emission from plasmonic metals. The anti-Stokes scattering proved unambiguous temperature-dependence and thus has been used as a thermometer to probe local temperature. The deviation from Bose-Einstein statistics at the high-energy anti-Stokes shift is attributed to a separate temperature, electronic temperature T_{e}. Importantly, the improved anti-Stokes Raman thermometry not only probed the electronic temperature but also the subpopulation of hot carriers, χ.

Additionally, we developed a theoretical model which hypothesizes the Raman scattering is from non-thermal carriers. The model is naturally compatible with previously developed two-temperature anti-Stokes Raman thermometry. Both material temperature and surface plasmon de-

phasing information can be extracted from a Raman spectrum using our model. Remarkably, we showed the consistency between extracted lattice temperature and stage temperature. Furthermore, the power-dependence study reveals the potential of using our model to correlate the plasmon dephasing information with chemical species adsorbed on metal surface. We believe these results will inform strategies to monitor chemical reactions using SERS application and improve the performance of plasmon-mediated photocatalytic reactions.

4. HOT ELECTRON EMISSION IN PLASMONIC THERMIONIC CONVERTERS

4.1 Thermionic Emission for Energy-Conversion Processes

Electron emission from a material surface occurs through three main possible processes; photoemission, thermionic emission, and field emission.[15] Photoemission occurs when an electron absorbs photonic energy allowing the electron to emit above the vacuum level. Thermionic emission is a process where thermal energy causes a broadening of the electron distribution such that some higher energy electrons will emit into vacuum. Field emission (quantum tunneling) is a quantum mechanical process in which electrons are able to tunnel through the surface barrier under high electric fields as discussed in Chapter 2. Figure 4.1 depicted a general energy diagram highlighting the three types of electron emission in which ϕ refers to the work function, which is the energy that an electron must gain above the Fermi energy (E_{F}) in order to emit into vacuum. In this chapter, we mainly focus on the thermionic emission from plasmonic nanostructures.*

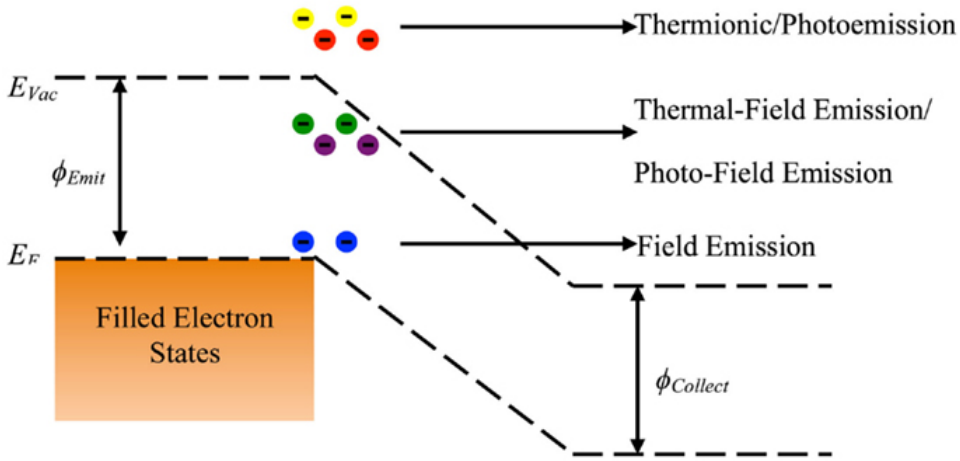

Figure 4.1: Energy diagram for electron emission from metals. Adapted from McCarthy et al.[15].

Research on thermionic emission dates back to 1853, when Becquerel[124] first detected electri-

*Adapted with permission from Wu, S.; Hogan, N.; Sheldon, M., Hot Electron Emission in Plasmonic Thermionic Converters. *ACS Energy Letters* **2019**, 4 (10), 2508-2513. Copyright 2019 ACS Publications.

cal current passing between two platinum wires, one hot and one cold, kept in a variety of gases. Many others contributed to the understanding of thermionic emission in the late nineteenth century, Guthrie [125] published his work on the relationship between heat and static electricity in 1873. Later in the nineteenth century, Angrist [126] investigated sealed devices in which electric current was generated between two electrodes, one hot and one cold, measured utilizing an electrometer. While research on thermionic emission continued through the ensuing decades, many of the significant advances in thermionic emission, dedicated toward energy generation, occurred in the 1950s. In 1956, Murphy and Good Jr [127] published a rigorous study of thermionic and field-emission theory, which includes the well-known Richardson-Dushman equation.

$$J_{\mathrm{T}} = \frac{mek_{\mathrm{B}}^2}{2\pi^2\hbar^3} T_{\mathrm{l}}^2 \exp(\frac{-\phi}{k_{\mathrm{B}} T_{\mathrm{l}}}) \qquad (4.1)$$

where J_{T} is the current density of thermionic emission, m is the electron mass, e is the elementary charge, k_{B} is Boltzmann's constant, $\hbar = h/2\pi$ is reduced Planck's constant, and $\frac{mek_{\mathrm{B}}^2}{2\pi^2\hbar^3}$ is commonly noted as Richardson's constant to simplify calculation. The full derivation of eq 4.1 is shown in appendix, and we shall see that the Richardson-Dushman equation can be derived the same manner as the quantum tunneling model established in Chapter 2.

Figure 4.2 depicted how thermionic emission current density J_{T} responses to temperature and the work function, ϕ, of a material. For most plasmonic metals, the work function is around $5\,\mathrm{eV}$. For example, the work functions of gold and silver are $5.1\,\mathrm{eV}$ [128] and $4.7\,\mathrm{eV}$, [129] respectively. Therefore, in order to extract substantial thermionic emission current from plasmonic nanostructures, a high temperature $\sim 2000\,\mathrm{K}$ is required. However, such a high temperature is not practical for most metals, as the melting point is typically around $1200\,\mathrm{K}$. [130] Therefore, strategy to reduce work function of the material is commonly applied. For instance, Cesium vapor is usually used in the practical thermionic emission devices, [131] not only because Cs has low electron affinity and is able to reduce the work function, but also Cs can effectively remove the space charge effect during electron emission. [131]

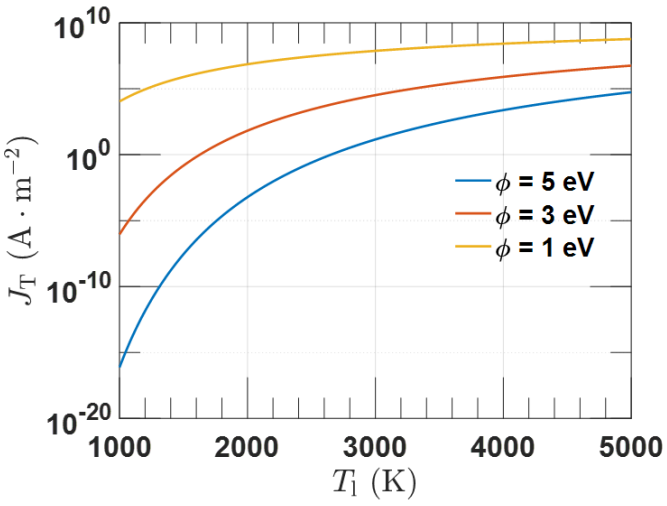

Figure 4.2: Relationship between thermionic emission current density J_{T} and temperature as a function of work function ϕ.

During the electron emission process, we usually have more than one mechanism occurs. For example, Schwede et al.[16] innovated a photo-enhanced thermionic emission (PETE) mechanism as depicted in Figure 4.3. Within the PETE scheme, the incident photons are more utilized as the heat produced by imperfect absorption can further redistribute carriers and facilitate emission.

Inspired by the PETE mechanism as well as our preliminary Raman study (Chapter 3) that the subpopulation of hot carriers is non-trivial and the electronic temperature is sufficient to promote thermionic emission from patterned gold nanostructures.

4.2 Thermionic Emission from Patterned Gold Nanostructures

4.2.1 Thermionic Emission Device and Electrical Measurement

For the measurement of the hot electron thermionic emission current density, a pair of parallel electrodes composed of nanostructured gold patterns and an ITO glass slide was constructed (Figure 4.4(a)). A $200\,\mu\mathrm{m}$ spacer separating the two electrodes was made of Kapton tap (attached to ITO glass) and copper tape (attached to the substrate of gold nanostructures) to ensure good electrical contact. The assembled electrode were placed in the same thermal stage (Linkam TS1500VE) used in Raman study to measure the thermionic emission current under vacuum ($< 10^{-5}\,\mathrm{torr}$).

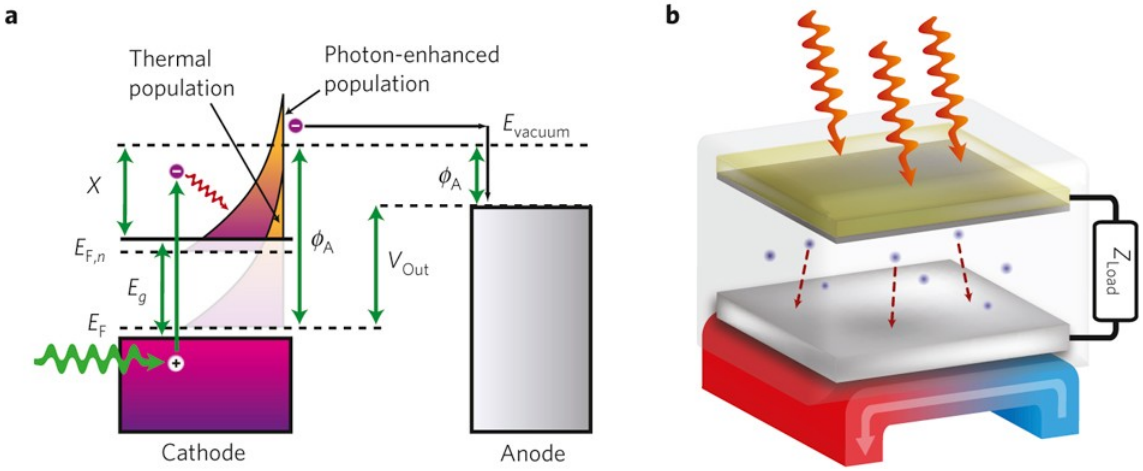

Figure 4.3: (a) Energy diagram of the PETE process. Photoexcitation increases the conduction-band population, leading to larger thermionic currents and enabling the device to harvest both photon and heat energy. (b) One possible implementation of a parallel-plate PETE converter. Photons impinge on a nanostructured cathode and excite electrons, which then emit into vacuum and are collected by an anode. Unused heat from the PETE cycle is used to drive a thermal engine. Adapted with permission from Schwede et al. [16]. Copyright 2010 by Springer Nature.

The electrodes were connected to a source measure unit (Keithley 2450) in order to measure the current at varying bias voltage. The light from a CW diode laser emitting at $532\,\mathrm{nm}$ was used for the photoexcitation, which was focused on the gold nanostructures through a $50\times$ objective to a focus spot on the sample with a beam diameter of $\sim 5.6\,\mu\mathrm{m}$. The thermionic emission current was measured with a lock-in amplifier (Stanford Research Systems, SR830) by chopping the excitation light at $47\,\mathrm{Hz}$. For each power density used, the bias voltage was swept from $-0.2\,\mathrm{V}$ (accelerating bias) to $1\,\mathrm{V}$ (retarding bias).

4.2.2 Result and Discussion

To demonstrate that the hot electrons excited at steady state can perform work, we constructed a thermionic power converter using the same nanostructure in Raman study (Chapter 3) as an emitter with an indium tin oxide (ITO) counter-electrode as a collector (Figure 4.4(a)). The current density, J, was measured via a lock-in amplification scheme from parallel electrodes separated by $200\,\mu\mathrm{m}$ during $532\,\mathrm{nm}$ CW illumination under vacuum ($0.01\,\mathrm{mbar}$). The power-generation region of the current-voltage ($J-V$) response is depicted in Figure 4.4(c). The open-circuit voltage (V_{oc})

reported here represents the retarding bias at which the current density reaches the noise level for the lock-in amplifier (Figure 4.4(b)). The downward curvature of the $J-V$ response indicates the presence of space charge effects during the measurement.[132]

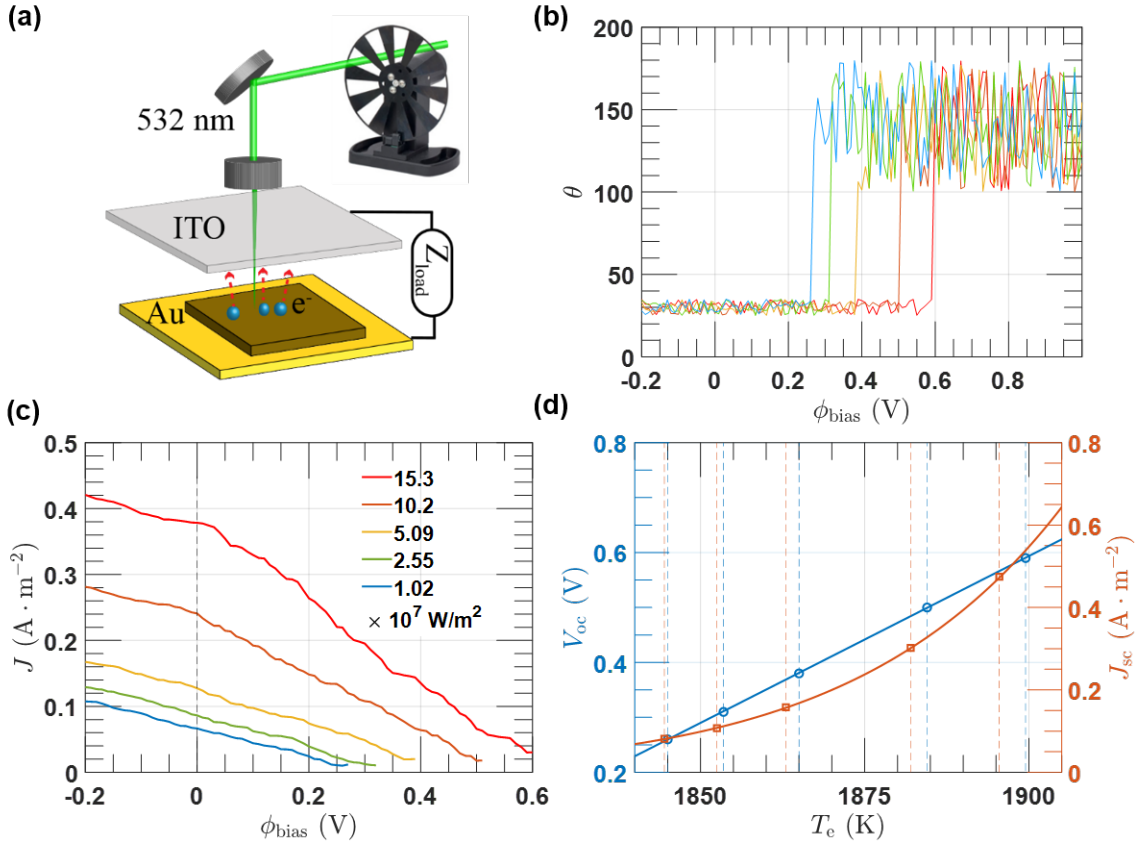

Figure 4.4: (a) Schematic of thermionic emission measurement. (b) Lock-in phase vs. applying bias, the abrupt 'jump' indicates the open-circuit voltage V_{oc}. (c) $J-V$ response measured at different optical powers. (d) Measured J_{sc} (square) and V_{oc} (circle) versus the calculated temperature according to a one-temperature model. The vertical dashed lines indicate the discrepancies in calculated temperature based on J_{sc} (red) or V_{oc} (blue). Adapted with permission from Wu et al.[13]. Copyright 2019 by ACS Publications.

The thermionic emission current density is conventionally described using Richardson-Dushman equation (eq 4.1), which we adapted to accommodate the two-temperature model. Because only a fraction of hot electrons, χ, at temperature T_{e} provide a non-negligible contribution to the

thermionic current,

$$J = \chi A T_{\mathrm{e}}^{2} \mathrm{e}^{-(\phi+\phi_{\mathrm{bias}})/k_{\mathrm{B}}T_{\mathrm{e}}} \qquad (4.2)$$

where $A = 1.2017 \times 10^{7}\ \mathrm{Am^{-2}K^{-2}}$ is the Richardson's constant, $\phi = 5.1\,\mathrm{eV}$ is the work function of gold,[128] ϕ_{bias} is the external potential with the positive sign indicating a retarding bias. If we analyze our data assuming a one-temperature model, then the short-circuit current at zero bias, J_{sc}, and the V_{oc} measured from the $J-V$ response are inconsistent with a unique extracted temperature (Figure 4.4(d)). However, for each optical power probed there is a unique combination of T_{e} and χ that can be input into eq 4.2 to accurately reproduce both the experimentally measured J_{sc} and V_{oc} as summarized in Figure 4.5.

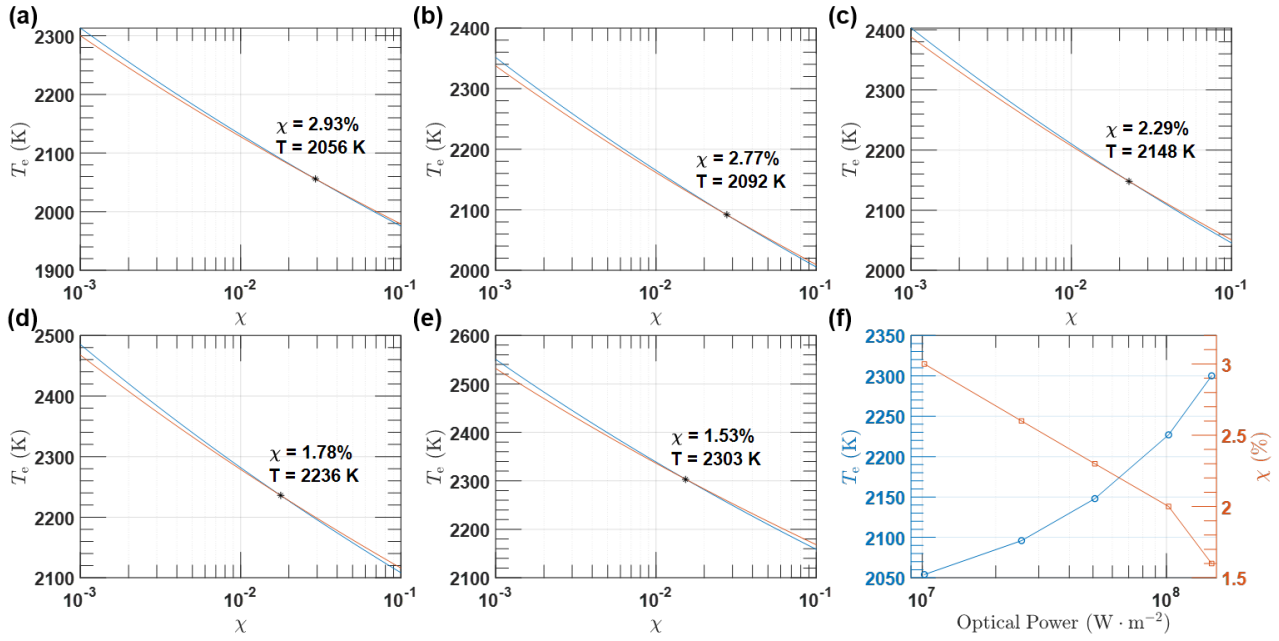

Figure 4.5: (a)-(e) Determination of electronic temperature and hot electron population using eq 4.2 (blue lines and red lines are iso-lines of J_{sc} and V_{oc} respectively). (f) Extracted electronic temperature (circle) and percentage of hot electrons χ (square) according to the two-temperature model of eq 4.2. Adapted with permission from Wu et al.[13]. Copyright 2019 by ACS Publications.

We find that T_{e} monotonically increased with optical power, with the same inverse relationship between χ and T_{e} measured in the Raman study. We note that the relationship between T_{e}

and χ may be different at even lower optical power regimes depending on the full temperature dependence of the electron-phonon coupling. Furthermore, the magnitude of χ is consistent with the Raman fitting under the same optical powers, although the extracted T_{e} based on the device response is somewhat lower. Several factors could give rise to this discrepancy, and we hypothesize that the largest source of error may be due to the more complex geometry of the space charge for electrons emitted by the nanostructure surface in comparison with the parallel plate geometry assumed in Langmuir's space charge theory.[132] In particular, the sharp corners of the nanostructure may generate a significantly larger fraction of vacuum-emitted electrons if emission is more likely where the optical field is locally concentrated. The result would be a greater space charge field near corners compared with a smooth surface. As an important point of comparison, we observed no measurable current under any optical power when a gold thin film was used as the emitter. This difference is likely due to a three-fold increase, at a minimum, in suitable escape cones for hot electrons in the nanocubes and highlights how momentum constrains are relaxed in the plasmonic nanostructure. Whereas we expect that the size of the nanostructures may play a crucial role in the generation rate and efficiency of hot electron emission, based on recent computational studies, we expect that the dynamics of the hot electrons for both the nanostructures and the thin film are dominated by surface scattering processes.

To demonstrate the potential of this strategy for solar power conversion, an additional sample was prepared that minimized losses due to conduction. The nanostructure was fabricated on a $50\,\mathrm{nm}$ thick $\mathrm{Si_3N_4}$ membrane. Focused ion beam etching was used to perforate the membrane and thermally isolate a $6 \times 6\,\mu\mathrm{m}$ section of the array (Figure 4.6(a)). In vacuum, the device achieved optical power conversion efficiency between 10^{-8} and $10^{-7}\%$ under 4×10^6 to $2.1 \times 10^7\,\mathrm{W \cdot m^{-2}}$ (Figure 4.6(c)). This optical power range is comparable to that employed in solar-thermal conversion schemes, where solar concentration factors are commonly between $1500\times$ and $4000\times$. Whereas the sample showed no evidence of thermal degradation, the seemingly low efficiency is due to the large work function of gold, $\phi = 5.1\,\mathrm{eV}$. It is common practice during thermionic device operation to include rarified Cs metal vapor to both decrease ϕ via surface adsorption and minimize

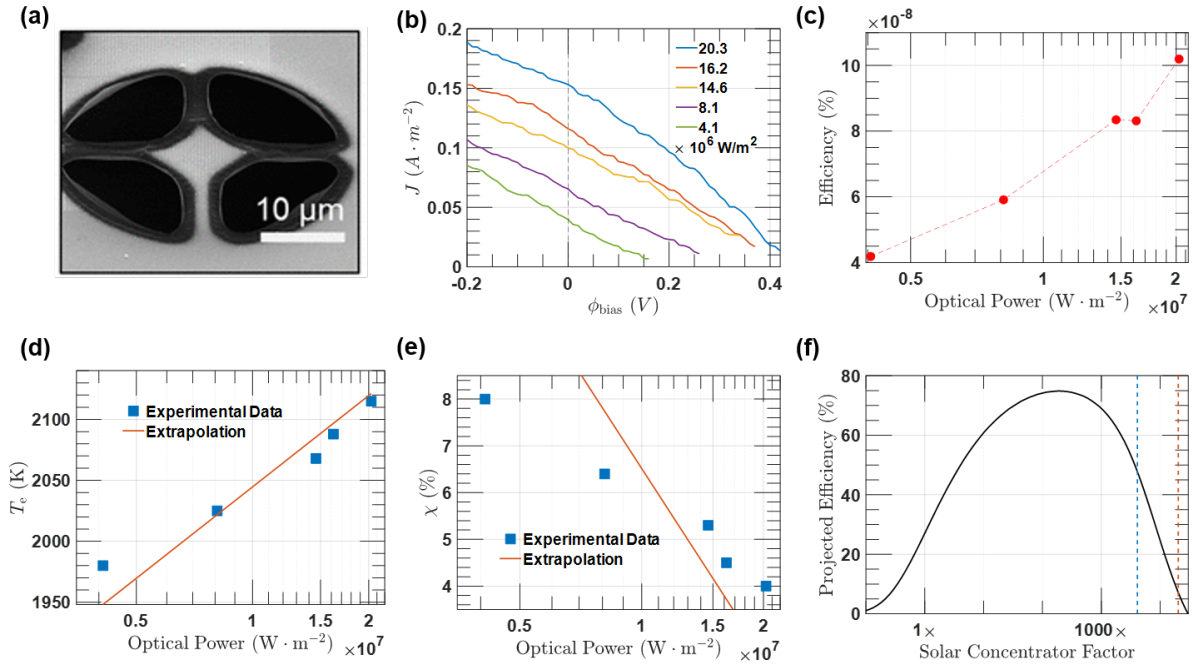

Figure 4.6: (a) SEM image of a thermally isolated gold nanostructure. (b) $J - V$ response of thermally-isolated gold nanostructures. (c) Measured optical power conversion efficiency. (d) Experimentally determined T_e vs. optical power and the extrapolation (red trace), ensuring zero incident power gives $T_e = 300\,\mathrm{K}$. (e) Experimentally determined χ vs. optical power and extrapolation (red trace) ensuring that zero incident optical power gives $\chi = 100\%$ and (f) Projected optical power conversion as a function of solar concentration factor, assuming a decreased work function, $\phi = 1.6$ eV. The blue and red vertical dashed lines denote the range of low and high optical powers, respectively, probed experimentally in panels b and c. Adapted with permission from Wu et al.[13]. Copyright 2019 by ACS Publications.

space charge effects. Gold surfaces with submonolayer cesium have a reported work function of $\phi = 1.6\,\mathrm{eV}$.[131] At low current density, the emitted electrons do not remove enough energy from the system to significantly perturb the electronic and lattice temperature, similar to a theoretical scenario in which no current is emitted and all optical power goes to photothermalization. Thus the $J - V$ response (Figure 4.6(b)) we measured provides a calibration that relates both the electronic temperature and the population of hot electrons at a given incident optical power (Figure 4.6(d,e)). Assuming that the presence of Cs does not significantly alter the plasmonic response of the absorber when the decreased work function is present, a maximum conversion efficiency of 74.9% is predicted to occur at $190\times$ solar concentration based on the trade-off between T_e and χ as

shown in Figure 4.6(f). If practically achievable, such high efficiency for collecting hot electrons would significantly decrease the optical energy that is available to promote heating of the lattice through electron-phonon coupling, further promoting the stability of the emitter. For comparison, state-of-the-art solar-thermal conversion strategies commonly achieve $\sim 30\%$ efficiency at lattice temperature greater than $1000\,\mathrm{K}$.[133]

4.3 Conclusion

In this chapter, three distinct mechanisms are identified: photoemission, thermionic emission and field emission (quantum tunneling). And we thoroughly discussed thermionic emission from plasmonic metals. This is inspired by the electronic temperature T_e and the subpopulation of hot carriers χ from previous Raman study. We constructed the thermionic power converter based on patterned gold nanostructures to demonstrate the potential of this strategy for solar power conversion.

The electrical measurements have demonstrated a new optoelectronic power conversion mechanism that uses plasmonic nanostructures to decouple electronic temperature and lattice temperature during the steady-state optical illumination of a thermionic emitter. Our results show an inverse relationship between the temperature and the population of the hot electron gas. When integrated into thermionic devices, the plasmonic cathodes provide optical power conversion efficiency consistent with the electronic temperature while maintaining significantly lower lattice temperatures. Thus we demonstrated how this mechanism can overcome challenges related to thermal stability that have historically limited the use of thermionic devices for solar-thermal energy conversion. We believe the remarkable tailorability of plasmonic nanostructures may allow further opportunities for very efficient solar energy conversion based on this strategy.

5. SUMMARY AND OUTLOOK

5.1 Summary

In this work, the dynamics of plasmon-mediated hot carriers have been explored. More importantly, energy distribution of hot carriers at steady state, which is more suitable in a practical scenario, is examined using variety methods. Many theoretical frameworks are proposed in this work, providing essential insight toward designing better plasmon-mediated hot carrier devices.

In Chapter 2, we studied the first stage after the dephase of localized surface plasmon, the non-thermal carriers. A free-electron jellium model accounting for the energy distribution of non-thermal carriers is reviewed. We further expanded the jellium model to a cube-shape nanosystem and a more practical scenario, e.g. plasmonic quantum-well. We observed a size-dependence of energy distribution that smaller nanoparticles generates more non-thermal carriers at higher energy state, which is consistent with many studies focused on different nanosystem. Furthermore, we envisioned an asymmetric plasmonic tunnel junction which employs quantum tunneling phenomenon in order to address the injection-barrier limitation. We derived a theoretical model describing the tunneling of non-thermal carriers from plasmonic metal. The optical power conversion efficiency within the tunneling scheme is analyzed and a 20% power conversion efficiency is predicted for an asymmetric $\mathrm{Au} - \mathrm{TiO_2} - \mathrm{Au}$ junction under solar flux illumination.

We further illustrated how the Raman measurement at steady state is able to reveal the energy distribution of hot carriers in Chapter 3. Patterned gold nanostructures are fabricated using electron-beam lithography, and the anti-Stokes Raman signal, though the origin is still under debate, is exploited to probe the local temperature of a material. The anti-Stokes Raman signal of a plasmonic metal, however, is not adequately described using a one-temperature model. The anti-Stokes scattering deviates from Bose-Einstein distribution at high energy Raman shift and we attributed the second slope as the energy distribution of hot carriers described by electronic temperature T_{e}. Furthermore, we are able to extract the subpopulation of hot carriers χ from anti-Stokes

scattering and a inverse relationship between T_{e} and χ is observed. Additionally, we hypothesized that the Stokes scattering scales with the size of non-thermal carriers. Preliminary studies bolster our hypothesis and a good agreement between theory and experiment is established.

An independent thermionic emission measurement is conducted to demonstrate the possibility to achieve optical power conversion using a novel hot-carrier-based solar-thermal technology as discussed in Chapter 4. The hot carriers with energy distribution described by T_{e} have sufficient energy to overcome the work function, and are thermally emitted. The $J - V$ response proves the presence of these high energy hot carriers. Furthermore, the subpopulation of hot carriers χ is proven essential to explain experimental determined J_{sc} and V_{oc}, and we observed the same inverse relationship between T_{e} and χ as determined in Raman study. We also predicted a significantly increased power conversion efficiency (74.9%) if a rarified Cs vapor is introduced in our thermionic emission device. The decoupling of electronic temperature and lattice temperature revitalized the thermionic emission power converter as it overcomes the thermal stability challenges.

5.2 Outlook

The Raman thermometry and thermionic emission experiments studied in this work are milestones in understanding the energy distribution of hot carriers at steady state. Many important physical parameters can be extracted from this work, such as electronic temperature T_{e}, subpopulation of hot carriers χ, as well as the plasmon dephasing time from Stokes Raman scattering. The full analysis of Raman spectra of plasmonic metals can be directly applied in surface-enhanced Raman spectroscopy (SERS) to probe the chemical reactions *in situ* and the connection between photocatalytic performance and plasmon dephase mechanism is able to guide the design of better plasmon-mediated hot carrier devices.

In terms of photocatalysis using plasmonic metals, it is crucial to distinguish the indirect carrier injection and the direct coupling between surface plasmon and molecular orbitals (chemical interface damping) as different optimization strategies are required for distinct mechanisms. Therefore, a variety of photocatalytic reactions can be examined using the analysis established in this work as the indirect carrier injection happens during the thermalization of hot carriers.

REFERENCES

[1] Hartland, G. V. *Chemical Reviews* **2011**, *111*, 3858–3887.

[2] Engheta, N. *Science* **2007**, *317*, 1698.

[3] Clavero, C. *Nature Photonics* **2014**, *8*, 95–103.

[4] Prineha, N.; Ravishankar, S.; Harry, A. A. *Nanophotonics* **2016**, *5*, 96–111.

[5] Leenheer, A. J.; Narang, P.; Lewis, N. S.; Atwater, H. A. *Journal of Applied Physics* **2014**, *115*, 134301.

[6] Linic, S.; Aslam, U.; Boerigter, C.; Morabito, M. *Nature Materials* **2015**, *14*, 567–576.

[7] Manjavacas, A.; Liu, J. G.; Kulkarni, V.; Nordlander, P. *ACS Nano* **2014**, *8*, 7630–7638.

[8] Hartland, G. V.; Besteiro, L. V.; Johns, P.; Govorov, A. O. *ACS Energy Letters* **2017**, *2*, 1641–1653.

[9] Wu, S.; Sheldon, M. T. *ACS Photonics* **2018**, *5*, 2516–2523.

[10] Cai, Y.-Y.; Liu, J. G.; Tauzin, L. J.; Huang, D.; Sung, E.; Zhang, H.; Joplin, A.; Chang, W.-S.; Nordlander, P.; Link, S. *ACS Nano* **2018**, *12*, 976–985.

[11] Hugall, J. T.; Baumberg, J. J. *Nano Letters* **2015**, *15*, 2600–2604.

[12] Xie, X.; Cahill, D. G. *Applied Physics Letters* **2016**, *109*, 183104.

[13] Wu, S.; Hogan, N.; Sheldon, M. *ACS Energy Letters* **2019**, *4*, 2508–2513.

[14] Barnett, S. M.; Harris, N.; Baumberg, J. J. *Physical Chemistry Chemical Physics* **2014**, *16*, 6544–6549.

[15] McCarthy, P. T.; Reifenberger, R. G.; Fisher, T. S. *Frontiers in Energy Research* **2014**, *2*.

[16] Schwede, J. W.; Bargatin, I.; Riley, D. C.; Hardin, B. E.; Rosenthal, S. J.; Sun, Y.; Schmitt, F.; Pianetta, P.; Howe, R. T.; Shen, Z.-X.; Melosh, N. A. *Nature Materials* **2010**, *9*, 762–767.

[17] Novotny, L.; Hecht, B. *Principles of Nano-Optics*; Cambridge University Press: Cambridge, 2006.

[18] Halas, N. J.; Lal, S.; Chang, W.-S.; Link, S.; Nordlander, P. *Chemical Reviews* **2011**, *111*,

3913–3961.

[19] Alvarez-Puebla, R.; Liz-Marzán, L. M.; García de Abajo, F. J. *The Journal of Physical Chemistry Letters* **2010**, *1*, 2428–2434.

[20] Li, W.; Valentine, J. *Nano Letters* **2014**, *14*, 3510–3514.

[21] Li, W.; Coppens, Z. J.; Besteiro, L. V.; Wang, W.; Govorov, A. O.; Valentine, J. *Nature Communications* **2015**, *6*, 8379.

[22] Lal, S.; Clare, S. E.; Halas, N. J. *Accounts of Chemical Research* **2008**, *41*, 1842–1851.

[23] Ayala-Orozco, C. et al. *ACS Nano* **2014**, *8*, 6372–6381.

[24] Atwater, H. A.; Polman, A. *Nature Materials* **2010**, *9*, 205–213.

[25] Link, S.; El-Sayed, M. A. *The Journal of Physical Chemistry B* **1999**, *103*, 8410–8426.

[26] Evanoff, D. D.; Chumanov, G. *The Journal of Physical Chemistry B* **2004**, *108*, 13957–13962.

[27] Langhammer, C.; Kasemo, B.; Zori, I. *The Journal of Chemical Physics* **2007**, *126*, 194702.

[28] Petek, H. *The Journal of Chemical Physics* **2012**, *137*, 091704.

[29] Kale, M. J.; Avanesian, T.; Christopher, P. *ACS Catalysis* **2014**, *4*, 116–128.

[30] Wu, K.; Chen, J.; McBride, J. R.; Lian, T. *Science* **2015**, *349*, 632.

[31] Boerigter, C.; Campana, R.; Morabito, M.; Linic, S. *Nature Communications* **2016**, *7*, 10545.

[32] Boerigter, C.; Aslam, U.; Linic, S. *ACS Nano* **2016**, *10*, 6108–6115.

[33] Tan, S.; Argondizzo, A.; Ren, J.; Liu, L.; Zhao, J.; Petek, H. *Nature Photonics* **2017**, *11*, 806–812.

[34] Moon, S. W.; Tsalu, P. V.; Ha, J. W. *Physical Chemistry Chemical Physics* **2018**, *20*, 22197–22202.

[35] Foerster, B.; Joplin, A.; Kaefer, K.; Celiksoy, S.; Link, S.; Sönnichsen, C. *ACS Nano* **2017**, *11*, 2886–2893.

[36] Kumar, P. V.; Rossi, T. P.; Marti-Dafcik, D.; Reichmuth, D.; Kuisma, M.; Erhart, P.; Puska, M. J.; Norris, D. J. *ACS Nano* **2019**, *13*, 3188–3195.

[37] Zhang, Y.; Nelson, T.; Tretiak, S.; Guo, H.; Schatz, G. C. *ACS Nano* **2018**, *12*, 8415–8422.

[38] Wu, K.; Rodríguez-Córdoba, W. E.; Yang, Y.; Lian, T. *Nano Letters* **2013**, *13*, 5255–5263.

[39] Wu, X.; Thrall, E. S.; Liu, H.; Steigerwald, M.; Brus, L. *The Journal of Physical Chemistry C* **2010**, *114*, 12896–12899.

[40] Mukherjee, S.; Libisch, F.; Large, N.; Neumann, O.; Brown, L. V.; Cheng, J.; Lassiter, J. B.; Carter, E. A.; Nordlander, P.; Halas, N. J. *Nano Letters* **2013**, *13*, 240–247.

[41] Mukherjee, S.; Zhou, L.; Goodman, A. M.; Large, N.; Ayala-Orozco, C.; Zhang, Y.; Nordlander, P.; Halas, N. J. *Journal of the American Chemical Society* **2014**, *136*, 64–67.

[42] Gomes Silva, C.; Juárez, R.; Marino, T.; Molinari, R.; García, H. *Journal of the American Chemical Society* **2011**, *133*, 595–602.

[43] Lee, J.; Mubeen, S.; Ji, X.; Stucky, G. D.; Moskovits, M. *Nano Letters* **2012**, *12*, 5014–5019.

[44] Thomann, I.; Pinaud, B. A.; Chen, Z.; Clemens, B. M.; Jaramillo, T. F.; Brongersma, M. L. *Nano Letters* **2011**, *11*, 3440–3446.

[45] Chen, H. M.; Chen, C. K.; Chen, C.-J.; Cheng, L.-C.; Wu, P. C.; Cheng, B. H.; Ho, Y. Z.; Tseng, M. L.; Hsu, Y.-Y.; Chan, T.-S.; Lee, J.-F.; Liu, R.-S.; Tsai, D. P. *ACS Nano* **2012**, *6*, 7362–7372.

[46] Zhou, L.; Swearer, D. F.; Zhang, C.; Robatjazi, H.; Zhao, H.; Henderson, L.; Dong, L.; Christopher, P.; Carter, E. A.; Nordlander, P.; Halas, N. J. *Science* **2018**, *362*, 69.

[47] Linic, S.; Christopher, P.; Ingram, D. B. *Nature Materials* **2011**, *10*, 911–921.

[48] Baffou, G.; Quidant, R. *Chemical Society Reviews* **2014**, *43*, 3898–3907.

[49] Seemala, B.; Therrien, A. J.; Lou, M.; Li, K.; Finzel, J. P.; Qi, J.; Nordlander, P.; Christopher, P. *ACS Energy Letters* **2019**, *4*, 1803–1809.

[50] Lee, Y. K.; Jung, C. H.; Park, J.; Seo, H.; Somorjai, G. A.; Park, J. Y. *Nano Letters* **2011**, *11*, 4251–4255.

[51] García de Arquer, F. P.; Mihi, A.; Kufer, D.; Konstantatos, G. *ACS Nano* **2013**, *7*, 3581–3588.

[52] Atar, F. B.; Battal, E.; Aygun, L. E.; Daglar, B.; Bayindir, M.; Okyay, A. K. *Optics Express*

2013, *21*, 7196–7201.

[53] Knight, M. W.; Sobhani, H.; Nordlander, P.; Halas, N. J. *Science* **2011**, *332*, 702.

[54] Chalabi, H.; Schoen, D.; Brongersma, M. L. *Nano Letters* **2014**, *14*, 1374–1380.

[55] Chen, H.; Su, L.; Jiang, M.; Fang, X. *Advanced Functional Materials* **2017**, *27*, 1704181.

[56] Furube, A.; Hashimoto, S. *NPG Asia Materials* **2017**, *9*, e454–e454.

[57] Khurgin, J. B. *Nanophotonics* **2019**, *0*.

[58] Liu, J. G.; Zhang, H.; Link, S.; Nordlander, P. *ACS Photonics* **2018**, *5*, 2584–2595.

[59] Ashcroft, N. W.; Mermin, N. D., et al. Solid state physics [by] Neil W. Ashcroft [and] N. David Mermin. 1976.

[60] Kittel, C.; McEuen, P.; McEuen, P. *Introduction to solid state physics*; Wiley New York, 1996; Vol. 8.

[61] Johnson, P. B.; Christy, R. W. *Phys. Rev. B* **1972**, *6*, 4370–4379.

[62] Alvarez, M. M.; Khoury, J. T.; Schaaff, T. G.; Shafigullin, M. N.; Vezmar, I.; Whetten, R. L. *The Journal of Physical Chemistry B* **1997**, *101*, 3706–3712.

[63] Kreibig, U.; Vollmer, M. *Optical properties of metal clusters*; Springer Science & Business Media, 2013; Vol. 25.

[64] Ehrenreich, H.; Philipp, H. R. *Phys. Rev.* **1962**, *128*, 1622–1629.

[65] Sönnichsen, C.; Franzl, T.; Wilk, T.; von Plessen, G.; Feldmann, J.; Wilson, O.; Mulvaney, P. *Phys. Rev. Lett.* **2002**, *88*, 077402.

[66] Mubeen, S.; Lee, J.; Singh, N.; Krämer, S.; Stucky, G. D.; Moskovits, M. *Nature Nanotechnology* **2013**, *8*, 247–251.

[67] Robatjazi, H.; Bahauddin, S. M.; Doiron, C.; Thomann, I. *Nano Letters* **2015**, *15*, 6155–6161.

[68] Linic, S.; Christopher, P.; Xin, H.; Marimuthu, A. *Accounts of Chemical Research* **2013**, *46*, 1890–1899.

[69] Govorov, A. O.; Zhang, H.; Gunko, Y. K. *The Journal of Physical Chemistry C* **2013**, *117*, 16616–16631.

[70] Zhang, Y.; Yam, C.; Schatz, G. C. *The Journal of Physical Chemistry Letters* **2016**, *7*, 1852–1858.

[71] Wei, Q.; Wu, S.; Sun, Y. *Advanced Materials* **2018**, *30*, 1802082.

[72] Harutyunyan, H.; Martinson, A. B. F.; Rosenmann, D.; Khorashad, L. K.; Besteiro, L. V.; Govorov, A. O.; Wiederrecht, G. P. *Nature Nanotechnology* **2015**, *10*, 770–774.

[73] Eesley, G. L. *Physical Review Letters* **1983**, *51*, 2140–2143.

[74] Brorson, S. D.; Fujimoto, J. G.; Ippen, E. P. *Physical Review Letters* **1987**, *59*, 1962–1965.

[75] Fowler, R. H. *Physical Review* **1931**, *38*, 45–56.

[76] Takahashi, Y.; Tatsuma, T. *Applied Physics Letters* **2011**, *99*, 182110.

[77] Knight, M. W.; Wang, Y.; Urban, A. S.; Sobhani, A.; Zheng, B. Y.; Nordlander, P.; Halas, N. J. *Nano Letters* **2013**, *13*, 1687–1692.

[78] Peters, D. W. *Proceedings of the IEEE* **1967**, *55*, 704–705.

[79] Sobhani, A.; Knight, M. W.; Wang, Y.; Zheng, B.; King, N. S.; Brown, L. V.; Fang, Z.; Nordlander, P.; Halas, N. J. *Nature Communications* **2013**, *4*, 1643.

[80] Menzel, D.; Gomer, R. *The Journal of Chemical Physics* **1964**, *41*, 3311–3328.

[81] Denzler, D. N.; Frischkorn, C.; Hess, C.; Wolf, M.; Ertl, G. *Phys Rev Lett* **2003**, *91*, 226102.

[82] Moskovits, M. *Nature Nanotechnology* **2015**, *10*, 6–8.

[83] Olsen, T.; Gavnholt, J.; Schiøtz, J. *Physical Review B* **2009**, *79*, 035403.

[84] Olsen, T.; Schiøtz, J. *Physical Review Letters* **2009**, *103*, 238301.

[85] Buntin, S. A.; Richter, L. J.; Cavanagh, R. R.; King, D. S. *Physical Review Letters* **1988**, *61*, 1321–1324.

[86] Busch, D. G.; Ho, W. *Physical Review Letters* **1996**, *77*, 1338–1341.

[87] Frischkorn, C.; Wolf, M. *Chemical Reviews* **2006**, *106*, 4207–4233.

[88] Messiah, A.; Schiff, L. I. *Quantum mechanics*; McGraw-Hill College, 1968; Vol. 643.

[89] Govorov, A. O.; Zhang, H. *The Journal of Physical Chemistry C* **2015**, *119*, 6181–6194.

[90] Kumarasinghe, C. S.; Premaratne, M.; Bao, Q.; Agrawal, G. P. *Scientific Reports* **2015**, *5*, 12140.

[91] Kong, X.-T.; Wang, Z.; Govorov, A. O. *Advanced Optical Materials* **2017**, *5*.

[92] Reddy, H.; Wang, K.; Kudyshev, Z.; Zhu, L.; Yan, S.; Vezzoli, A.; Higgins, S. J.; Gavini, V.; Boltasseva, A.; Reddy, P.; Shalaev, V. M.; Meyhofer, E. *Science* **2020**, *369*, 423.

[93] Lee, Y. K.; Park, J.; Park, J. Y. *The Journal of Physical Chemistry C* **2012**, *116*, 18591–18596.

[94] Cui, L.; Jeong, W.; Fernández-Hurtado, V.; Feist, J.; García-Vidal, F. J.; Cuevas, J. C.; Meyhofer, E.; Reddy, P. *Nature Communications* **2017**, *8*, 14479.

[95] St-Gelais, R.; Zhu, L.; Fan, S.; Lipson, M. *Nature Nanotechnology* **2016**, *11*, 515–519.

[96] Fang, Y.; Jiao, Y.; Xiong, K.; Ogier, R.; Yang, Z.-J.; Gao, S.; Dahlin, A. B.; Käll, M. *Nano Letters* **2015**, *15*, 4059–4065.

[97] Zolotavin, P.; Evans, C. I.; Natelson, D. *Nanoscale* **2017**, *9*, 9160–9166.

[98] Svensson, R.; Holmlid, L. *Surface Science* **1992**, *269-270*, 695–699.

[99] Moskovits, M. *Science* **2011**, *332*, 676.

[100] Ferry, V. E.; Munday, J. N.; Atwater, H. A. *Advanced Materials* **2010**, *22*, 4794–4808.

[101] Chirumamilla, M.; Roberts, A. S.; Ding, F.; Wang, D.; Kristensen, P. K.; Bozhevolnyi, S. I.; Pedersen, K. *Optical Materials Express* **2016**, *6*, 2704–2714.

[102] Cheng, Y.; Lu, G.; He, Y.; Shen, H.; Zhao, J.; Xia, K.; Gong, Q. *Nanoscale* **2016**, *8*, 2188–2194.

[103] Lin, K.-Q.; Yi, J.; Zhong, J.-H.; Hu, S.; Liu, B.-J.; Liu, J.-Y.; Zong, C.; Lei, Z.-C.; Wang, X.; Aizpurua, J.; Esteban, R.; Ren, B. *Nature Communications* **2017**, *8*, 14891.

[104] Carattino, A.; Keizer, V. I. P.; Schaaf, M. J. M.; Orrit, M. *Biophysical Journal* **2016**, *111*, 2492–2499.

[105] Carattino, A.; Caldarola, M.; Orrit, M. *Nano Letters* **2018**, *18*, 874–880.

[106] Mooradian, A. *Physical Review Letters* **1969**, *22*, 185–187.

[107] Mohamed, M. B.; Volkov, V.; Link, S.; El-Sayed, M. A. *Chemical Physics Letters* **2000**, *317*, 517–523.

[108] Hu, H.; Duan, H.; Yang, J. K. W.; Shen, Z. X. *ACS Nano* **2012**, *6*, 10147–10155.

[109] Dulkeith, E.; Niedereichholz, T.; Klar, T. A.; Feldmann, J.; von Plessen, G.; Gittins, D. I.; Mayya, K. S.; Caruso, F. *Physical Review B* **2004**, *70*, 205424.

[110] Losquin, A.; Kociak, M. *ACS Photonics* **2015**, *2*, 1619–1627.

[111] Huang, J.; Wang, W.; Murphy, C. J.; Cahill, D. G. *Proceedings of the National Academy of Sciences of the United States of America* **2014**, *111*, 906–911.

[112] Weiner, J. S.; Yu, P. Y. *Solid State Communications* **1984**, *50*, 493–496.

[113] Cialla, D.; März, A.; Böhme, R.; Theil, F.; Weber, K.; Schmitt, M.; Popp, J. *Analytical and Bioanalytical Chemistry* **2012**, *403*, 27–54.

[114] Szczerbiski, J.; Gyr, L.; Kaeslin, J.; Zenobi, R. *Nano Letters* **2018**, *18*, 6740–6749.

[115] Singh, N. *International journal of modern physics b* **2010**, *24*, 1141–1158.

[116] Jiang, L.; Tsai, H.-L. *Journal of Heat Transfer* **2005**, *127*, 1167–1173.

[117] Bagchi, A.; Barrera, R. G.; Dasgupta, B. B. *Phys. Rev. Lett.* **1980**, *44*, 1475–1478.

[118] Burstein, E.; Chen, Y. J.; Chen, C. Y.; Lundquist, S.; Tosatti, E. *Solid State Communications* **1979**, *29*, 567–570.

[119] Gersten, J. I.; Birke, R. L.; Lombardi, J. R. *Phys. Rev. Lett.* **1979**, *43*, 147–150.

[120] Weber, W. H.; Ford, G. W. *Phys. Rev. Lett.* **1980**, *44*, 1774–1777.

[121] Otto, A.; Akemann, W.; Pucci, A. *Israel Journal of Chemistry* **2006**, *46*, 307–315.

[122] Veres, M.; Füle, M.; Tóth, S.; Koós, M.; Pócsik, I. *Diamond and Related Materials* **2004**, *13*, 1412–1415.

[123] Li, Y.; Sun, Q.; Zu, S.; Shi, X.; Liu, Y.; Hu, X.; Ueno, K.; Gong, Q.; Misawa, H. *Phys. Rev. Lett.* **2020**, *124*, 163901.

[124] Becquerel, M. E. *The London, Edinburgh, and Dublin Philosophical Magazine and Journal of Science* **1853**, *6*, 456–457.

[125] Guthrie, F. *The London, Edinburgh, and Dublin Philosophical Magazine and Journal of Science* **1873**, *46*, 257–266.

[126] Angrist, S. W. **1976**,

[127] Murphy, E. L.; Good Jr, R. *Physical review* **1956**, *102*, 1464.

[128] Sachtler, W. M. H.; Dorgelo, G. J. H.; Holscher, A. A. *Surface Science* **1966**, *5*, 221–229.

[129] Dweydari, A. W.; Mee, C. H. B. *physica status solidi (a)* **1975**, *27*, 223–230.

[130] Gao, F.; Gu, Z. *Handbook of nanoparticles. Cham: Springer. https://doi. org/10.1007/978-3-319-15338-4_6* **2016**,

[131] LaRue, J. L.; White, J. D.; Nahler, N. H.; Liu, Z.; Sun, Y.; Pianetta, P. A.; Auerbach, D. J.; Wodtke, A. M. *The Journal of Chemical Physics* **2008**, *129*, 024709.

[132] Hatsopoulos, G. N.; Gyftopoulos, E. P. **1973**,

[133] Siva Reddy, V.; Kaushik, S. C.; Ranjan, K. R.; Tyagi, S. K. *Renewable and Sustainable Energy Reviews* **2013**, *27*, 258–273.

APPENDIX A

FREE ELECTRON JELLIUM MODEL EXPANSION

The probability per unit time of exciting a hot electron in state f can be calculated using Fermi's golden rule (eq 2.1)

$$\Gamma_{\mathrm{e}}(\varepsilon_{\mathrm{f}},\omega)=\frac{4}{\tau}f(\varepsilon_{\mathrm{i}})[1-f(\varepsilon_{\mathrm{f}})]\{\frac{|M_{\mathrm{fi}}(\omega)|^2}{(\hbar\omega-\varepsilon_{\mathrm{f}}+\varepsilon_{\mathrm{i}})^2+\hbar^2\tau^{-2}}+\frac{|M^*_{\mathrm{if}}(\omega)|^2}{(\hbar\omega+\varepsilon_{\mathrm{f}}-\varepsilon_{\mathrm{i}})^2+\hbar^2\tau^{-2}}\} \qquad (A.1)$$

where f is the Fermi-Dirac distribution function, in which for simplicity we assume zero temperature, $M_{\mathrm{fi}}=\int \mathrm{d}rV(r,\omega)\rho_{\mathrm{fi}}(r)$ is the transition matrix element, and we have included a factor of 2 to account for the spin. $\rho_{\mathrm{fi}}(r)=e\Psi^*_{\mathrm{f}}(r)\Psi_i(r)$ where e is the elementary charge.

The wavefunction and corresponding energy for electron in a 3D box is given in eq 2.2a and eq 2.2b.

$$\Psi(x,y,z)=(\frac{2^3}{L_{\mathrm{x}}L_{\mathrm{y}}L_{\mathrm{z}}})^{1/2}\sin(\frac{\pi n_{\mathrm{x}}x}{L_{\mathrm{x}}})\sin(\frac{\pi n_{\mathrm{y}}y}{L_{\mathrm{y}}})\sin(\frac{\pi n_{\mathrm{z}}z}{L_{\mathrm{z}}})=\psi_{n_{\mathrm{x}}}(x)\psi_{n_{\mathrm{y}}}(y)\psi_{n_{\mathrm{z}}}(z) \qquad (A.2)$$

$$E(n_{\mathrm{x}},n_{\mathrm{y}},n_{\mathrm{z}})=\frac{\hbar^2\pi^2}{2m}(\frac{n^2_{\mathrm{x}}}{L^2_{\mathrm{x}}}+\frac{n^2_{\mathrm{y}}}{L^2_{\mathrm{y}}}+\frac{n^2_{\mathrm{z}}}{L^2_{\mathrm{z}}}) \qquad (A.3)$$

potential inside a nanocube

If the dimensions of the cube are small compared to the wavelength of the incident radiation, we can assume that the incident electric field is uniform and does not vary spatially inside the nanocube. The internal potential V can then be found by $\overrightarrow{E}(\omega)=-\nabla V(r,\omega)$. Or $V=r\overrightarrow{E}$.

transition matrix element

The transition matrix is $M_{\mathrm{fi}}=\int \mathrm{d}rV(r,\omega)\rho_{\mathrm{fi}}(r)$, another form is $\langle\Psi^*_{\mathrm{f}}|eV(r)|\Psi_{\mathrm{i}}\rangle=e\overrightarrow{E}\langle\Psi^*_{\mathrm{f}}|r|\Psi_{\mathrm{i}}\rangle$. By using the quantum mechanical relationship between the position operator and the momentum

operator $\hat{p} = -j\hbar\nabla$, which is defined as

$$\langle \Psi_{\mathrm{f}}^{*}|r|\Psi_{\mathrm{i}}\rangle = \frac{j\hbar}{m(\varepsilon_{\mathrm{f}} - \varepsilon_{\mathrm{i}})}\langle \Psi_{\mathrm{f}}^{*}|\hat{p}|\Psi_{\mathrm{i}}\rangle \qquad (A.4)$$

The transition matrix element is therefore

$$\langle \Psi_{\mathrm{f}}^{*}|eV(r)|\Psi_{\mathrm{i}}\rangle = e\overrightarrow{E}\langle \Psi_{\mathrm{f}}^{*}|r|\Psi_{\mathrm{i}}\rangle = e\overrightarrow{E}\frac{j\hbar}{m(\varepsilon_{\mathrm{f}} - \varepsilon_{\mathrm{i}})}\langle \Psi_{\mathrm{f}}^{*}|\hat{p}|\Psi_{\mathrm{i}}\rangle$$

$$= e\overrightarrow{E}\frac{j\hbar}{m(\varepsilon_{\mathrm{f}} - \varepsilon_{\mathrm{i}})}\int \Psi_{\mathrm{f}}^{*}(r)(-j\hbar)(\nabla\Psi_{\mathrm{i}}(r))\mathrm{d}\tau = \frac{e\overrightarrow{E}\hbar^{2}}{m(\varepsilon_{\mathrm{f}} - \varepsilon_{\mathrm{i}})}\int \Psi_{\mathrm{f}}^{*}(r)\nabla\Psi_{\mathrm{i}}(r)\mathrm{d}\tau \qquad (A.5)$$

We assume the electric field perturbation is along the x direction, therefore we have

$$\nabla\Psi_{\mathrm{i}}(r) = (\hat{x}\frac{\partial}{\partial x} + \hat{y}\frac{\partial}{\partial y} + \hat{z}\frac{\partial}{\partial z})\psi_{\mathrm{n_{x,i}}}(x)\psi_{\mathrm{n_{y,i}}}(y)\psi_{\mathrm{n_{z,i}}}(z) = (\frac{\partial}{\partial x}\psi_{n_{\mathrm{x,i}}}(x))\psi_{\mathrm{n_{y,i}}}(y)\psi_{\mathrm{n_{z,i}}}(z) \qquad (A.6)$$

The derivative of the x direction component of the wave function is calculated as

$$\frac{\partial}{\partial x}\psi_{\mathrm{n_{x,i}}}(x) = \frac{\partial}{\partial x}[\sqrt{\frac{2}{L_{\mathrm{x}}}}\sin(\frac{\pi n_{\mathrm{x,i}}x}{L_{\mathrm{x}}})] = \sqrt{\frac{2}{L_{\mathrm{x}}}}\frac{\pi n_{\mathrm{x,i}}}{L_{\mathrm{x}}}\cos(\frac{\pi n_{\mathrm{x,i}}x}{L_{\mathrm{x}}}) \qquad (A.7)$$

Substitute eq A.7 in eq A.6, we have

$$\langle \Psi_{\mathrm{f}}^{*}|eV(r)|\Psi_{\mathrm{i}}\rangle = \frac{e\overrightarrow{E}\hbar^{2}}{m(\varepsilon_{\mathrm{f}} - \varepsilon_{\mathrm{i}})}\int \Psi_{\mathrm{f}}^{*}(r)\nabla\Psi_{\mathrm{i}}(r)d\tau$$

$$= \frac{e\overrightarrow{E}\hbar^{2}}{m(\varepsilon_{\mathrm{f}} - \varepsilon_{\mathrm{i}})}\int [\psi_{n_{\mathrm{x,f}}}^{*}(x)\psi_{n_{\mathrm{y,f}}}^{*}(y)\psi_{n_{\mathrm{z,f}}}^{*}(z)(\frac{\partial}{\partial x}\psi_{\mathrm{n_{x,i}}}(x))\psi_{\mathrm{n_{y,i}}}(y)\psi_{\mathrm{n_{z,i}}}(z)]\mathrm{d}\tau \qquad (A.8)$$

Due to the orthonormal nature of the wave function, eq A.8 can be simplified as

$$\langle \Psi_{\mathrm{f}}^{*}|eV(r)|\Psi_{\mathrm{i}}\rangle = \frac{e\overrightarrow{E}\hbar^{2}}{m(\varepsilon_{\mathrm{f}} - \varepsilon_{\mathrm{i}})}\delta_{\mathrm{n_{y,i},x_{y,f}}}\delta_{\mathrm{n_{z,i},x_{z,f}}}\int_{0}^{L_{\mathrm{x}}}\frac{2\pi n_{\mathrm{x,i}}}{L_{\mathrm{x}}^{2}}\sin(\frac{\pi n_{\mathrm{x,f}}x}{L_{\mathrm{x}}})\cos(\frac{\pi n_{\mathrm{x,i}}x}{L_{\mathrm{x}}})\mathrm{d}x \qquad (A.9)$$

Since

$$\sin(x)\cos(y) = \frac{1}{2}[\sin(x+y) + \sin(x-y)]$$

Therefore

$$\int_0^{L_x} \frac{2\pi n_{x,i}}{L_x^2} \sin(\frac{\pi n_{x,f} x}{L_x}) \cos(\frac{\pi n_{x,i} x}{L_x}) \mathrm{d}x = \frac{2\pi n_{x,i}}{L_x^2} \int_0^{L_x} \sin(\frac{\pi n_{x,f} x}{L_x}) \cos(\frac{\pi n_{x,i} x}{L_x}) dx$$

$$= \frac{2\pi n_{x,i}}{L_x^2} \int_0^{L_x} \frac{1}{2}[\sin(\frac{\pi(n_{x,f} + n_{x,i})x}{L_x}) + \sin(\frac{\pi(n_{x,f} - n_{x,i})x}{L_x})] dx$$

$$= \frac{n_{x,i}}{L_x}[\frac{1}{(n_{x,f} + n_{x,i})}(1 - \cos(\pi(n_{x,f} + n_{x,i}))) + \frac{1}{(n_{x,f} - n_{x,i})}(1 - \cos(\pi(n_{x,f} - n_{x,i})))]$$

Since when transition occurs, $n_{y,i} = n_{y,f}$ and $n_{z,i} = n_{z,f}$, then $\varepsilon_f - \varepsilon_i = \frac{\hbar^2\pi^2}{2mL_x^2}(n_{x,f}^2 - n_{x,i}^2)$, the transition matrix element from eq A.9 is then

$$\langle \Psi_f^* | eV(r) | \Psi_i \rangle = \frac{2n_{x,i} L_x \overrightarrow{E}}{\pi^2(n_{x,f}^2 - n_{x,i}^2)} \delta_{n_{y,i}, x_{y,f}} \delta_{n_{z,i}, x_{z,f}}$$

$$[\frac{1}{(n_{x,f} + n_{x,i})}(1 - \cos(\pi(n_{x,f} + n_{x,i}))) + \frac{1}{(n_{x,f} - n_{x,i})}(1 - \cos(\pi(n_{x,f} - n_{x,i})))] \qquad \text{(A.10)}$$

eq A.10 is exactly the eq 2.3. We note that the selection rule is that $\Delta n_x = n_{x,f} - n_{x,i}$ must be an odd number.

APPENDIX B

DERIVATION OF RICHARDSON DUSHMAN EQUATION

We hereby derive the Richardson Dushman equation (eq 4.1) from the theoretical framework we established in Chapter 2.

We also start from the electron distribution in a metal (eq 2.5)

$$n(v)\mathrm{d}v_\mathrm{x}\mathrm{d}v_\mathrm{y}\mathrm{d}v_\mathrm{z} = \frac{2m^3}{h^3} f(E)\mathrm{d}v_\mathrm{x}\mathrm{d}v_\mathrm{y}\mathrm{d}v_\mathrm{z} \qquad \text{(A.11)}$$

Here, n is the electron density, v is electron velocity, v_x, v_y, v_z are electron velocity in the x, y, z directions, respectively, m is electron mass, h is Planck's constant, and $f(E)$ is the Fermi-Dirac distribution function at energy E.

For simplicity, we consider electron transport in the x direction and we rewrite eq $\mathrm{A}.11$ in terms on v_x:

$$n(v_\mathrm{x}) = \frac{2m^3}{h^3} \int \int_{-\infty}^{\infty} f(E)\mathrm{d}v_\mathrm{y}\mathrm{d}v_\mathrm{z} = \frac{2\pi m^2}{h^3} \int_0^{\infty} f(E)\mathrm{d}E_\mathrm{r} \qquad \text{(A.12)}$$

where $v_\mathrm{r}^2 = v_\mathrm{y}^2 + v_\mathrm{z}^2$, $E_\mathrm{x} = \frac{1}{2}mv_\mathrm{x}^2$ and $E_\mathrm{r} = E - E_\mathrm{x} = \frac{mv_\mathrm{r}^2}{2}$.

The electron flux, $N_{\mathrm{l}\to\mathrm{r}}$, from left to right, can be calculated by integrating the product of eq 2.6 with electron velocity v_x and emission probability $\mathrm{P}(E)$ for all possible electron energies.

$$N_{l\to r} = \int_0^{\infty} v_\mathrm{x} n(v_\mathrm{x})\mathrm{P}(E_\mathrm{x})\mathrm{d}v_\mathrm{x} = \frac{1}{m}\int_0^{\infty} n(v_\mathrm{x})\mathrm{P}(E_\mathrm{x})\mathrm{d}E_\mathrm{x}$$

$$= \frac{2\pi m}{h^3} \int_0^{\infty} \Big(\int_{E_\mathrm{x}}^{\infty} f(E)dE \Big) P(E_\mathrm{x})\mathrm{d}E_\mathrm{x} \qquad \text{(A.13)}$$

Assume the left electrode is the emitter while the right electrode is the collector. Then the current density J for a thermionic emission is contributed solely from electron emission from left to right. Since only electrons have sufficient energy compared to workfunction ϕ are thermally

emitted and the transition probability is unity $P(E_{\mathrm{x}}) = 1$, eq $\mathrm{A}.13$ becomes

$$N_{\mathrm{l}\to\mathrm{r}} = \frac{2\pi m}{h^3}\int_{\phi+E_{\mathrm{F}}}^{\infty}\Big(\int_{E_{\mathrm{x}}}^{\infty} f(E)\mathrm{d}E\Big)\mathrm{d}E_x = \frac{2\pi m}{h^3}\int_{\phi+E_{\mathrm{F}}}^{\infty}\Big(\int_{E_{\mathrm{x}}}^{\infty}\frac{1}{\mathrm{e}^{(E-E_{\mathrm{F}})/k_{\mathrm{B}}T}+1}\mathrm{d}E\Big)\mathrm{d}E_{\mathrm{x}} \qquad (\mathrm{A}.14)$$

Since temperature T is extremely high ($\sim$ $1200\,\mathrm{K}$) for thermionic emission to occur, the 1 in Fermi-Dirac distribution may be dropped. Therefore

$$N_{\mathrm{l}\to\mathrm{r}} = \frac{2\pi m}{h^3}\int_{\phi+E_{\mathrm{F}}}^{\infty}\Big(\int_{E_{\mathrm{x}}}^{\infty}\frac{1}{\mathrm{e}^{(E-E_{\mathrm{F}})/k_{\mathrm{B}}T}}\mathrm{d}E\Big)\mathrm{d}E_{\mathrm{x}} = -k_{\mathrm{B}}T\frac{2\pi m}{h^3}\int_{\phi+E_{\mathrm{F}}}^{\infty}\frac{1}{\mathrm{e}^{(E_{\mathrm{x}}-E_{\mathrm{F}})/k_{\mathrm{B}}T}}\mathrm{d}E_{\mathrm{x}}$$

$$= \frac{2\pi m}{h^3}k_{\mathrm{B}}^2T^2\mathrm{e}^{-\phi/k_{\mathrm{B}}T} \qquad (\mathrm{A}.15)$$

To get the emission current density J, we simply multiply eq $\mathrm{A}.15$ by the elementary charge e.

$$J = \frac{2\pi me}{h^3}k_{\mathrm{B}}^2T^2\mathrm{e}^{-\phi/k_{\mathrm{B}}T} \qquad (\mathrm{A}.16)$$

Note that eq $\mathrm{A}.16$ is exactly the Richardson Dushman equation (eq 4.1).

APPENDIX C

MATLAB CODE IN CALCULATION

Non-thermal carriers generation in a gold slab at absolute zero

The non-thermal carriers generation rate in a 5 nm gold slab is shown in Figure C.1.

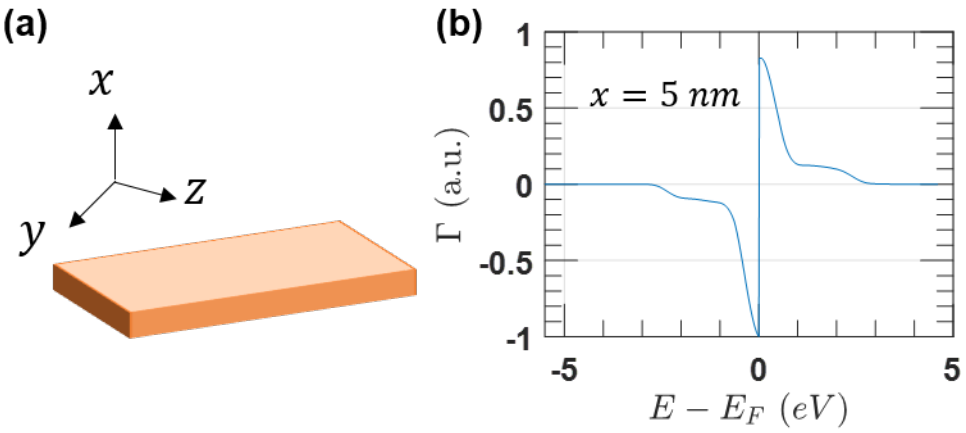

Figure C.1: (a) Schematic of gold slab, only x axis is restricted, (b) Non-thermal carrier generation at absolute zero. The electric field of incident photons is along the x axis.

The following code is used to reproduce Figure C.1(b).

```
%%
% Contributor: Shengxiang Wu

%% clear workspace and close current figures
clear all
close all

```

```
8
9  %% define physical constant
10 electron_charge =  1.602 .* 10 .^ (-19);
11 electron_mass = 9.1094 .* 10 .^ (-31);
12 % reduced Planck's constant, h_bar
13 h_bar = 1.0546 .* 10 .^ (-34);
14 % Fermi energy of gold, E_Fermi
15 E_Fermi = 5.5 * electron_charge;
16 % Incident photon energy, E_photon
17 E_photon = 2.3 * electron_charge;
18
19 %% Parameters
20 % dimension in x axis, Lx
21 Lx = 10 * 10 ^ -9;
22 % Energy step, E_step, the smaller step, the preciser result
23 E_step = h_bar ^ 2 * pi ^ 2 ./ (2 * electron_mass * Lx ^ 2);
24 % Plasmon dephasing time, tao
25 tao = 10 * 10 ^ -15;
26 %%
27 % possible energy of final states at absolute zero
28 E_f = linspace(E_Fermi + E_step, E_Fermi + E_photon * 2, (E_Fermi
       + E_photon * 2 - E_Fermi - E_step) / E_step + 1);
29 % possible energy of initial states at absolute zero
30 E_i = linspace(0, E_Fermi, E_Fermi / E_step + 1);
31 %%
32 % generation rate for initial states
33 Gamma_i = zeros(length(E_i), 1);
```

```
% generation rate for final states
Gamma_f = zeros(length(E_f), 1);

%% Calculation
for index_f = 1:length(E_f)
    for index_i = 1:length(E_i)
        E_yz = linspace(0, E_i(index_i) - E_step, (E_i(index_i) -
            E_step) / E_step + 1);
        for index = 1:length(E_yz)
            n_xi = floor(((E_i(index_i) - E_yz(index)) ./ E_step)
                .^ 0.5);
            n_xf = floor(((E_f(index_f) - E_yz(index)) ./ E_step)
                .^ 0.5);
            % selection rule is that the change of nx must be odd
                number
            if mod(abs(n_xi - n_xf), 2) ~= 0
                M = n_xi * Lx ./ (n_xf .^ 2 - n_xi .^ 2) .* ((1 -
                    cos(pi * (n_xf + n_xi))) ./ (n_xf + n_xi) +
                   (1 - cos(pi * (n_xf - n_xi))) ./ (n_xf - n_xi)
                   );
                Gamma = 4 ./ tao .* ((M .^ 2) ./ ((E_photon -
                   E_step .* (n_xf .^ 2 - n_xi .^ 2)) .^ 2 +
                   h_bar ^ 2 * tao ^ -2) + (M .^ 2) ./ ((E_photon
                    + E_step .* (n_xf .^ 2 - n_xi .^ 2)) .^ 2 +
                   h_bar ^ 2 * tao ^ -2));
                Gamma_i(index_i) = Gamma_i(index_i) - Gamma;
                Gamma_f(index_f) = Gamma_f(index_f) + Gamma;
```

```
            end
        end
    end
end
%% plot energy distribution of non-thermal carriers
hot_energy = [E_i, E_f];
hot_gamma = [Gamma_i; Gamma_f];
figure
plot((hot_energy - E_Fermi) / electron_charge, hot_gamma / max(
    abs(hot_gamma)))

grid on
set(gcf, 'Units', 'Inches', 'Position', [0, 0, 4, 3])
set(gca,'FontSize',16)
set(gca,'FontWeight','bold')
set(gca,'XMinorTick','on')
set(gca,'YMinorTick','on')
set(gca,'TickLength',[0.08, 0.12])
xlabel('$E-E_F$ ($eV$)', 'Interpreter', 'Latex', 'FontWeight', '
    bold')
ylabel('$\Gamma$ (a.u.)', 'Interpreter', 'Latex', 'FontWeight', '
    bold')
box on
```

Non-thermal carriers generation in a gold slab at finite temperature

The non-thermal carriers generation rate in a 5 nm gold slab at 300 K and 500 K is shown in Figure C.2.

The following code is used to reproduce Figure C.2.

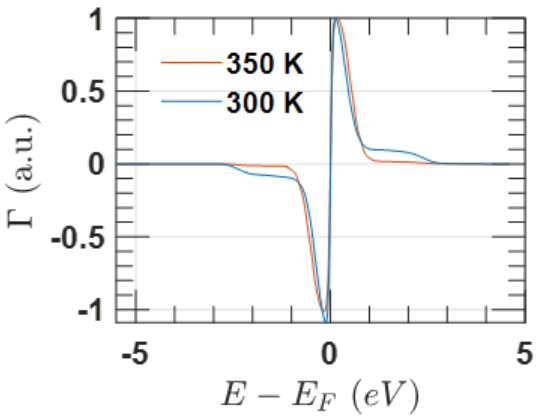

Figure C.2: Non-thermal carrier generation at 300 K (blue) and 350 K (red).

```
%%
% Contributor: Shengxiang Wu

%% clear workspace and close current figures
clear all
close all

%% define physical constant
electron_charge =  1.602 .* 10 .^ (-19);
electron_mass = 9.1094 .* 10 .^ (-31);
% reduced Planck's constant, h_bar
h_bar = 1.0546 .* 10 .^ (-34);
% Fermi energy of gold, E_Fermi
E_Fermi = 5.5 * electron_charge;
% Incident photon energy, E_photon
E_photon = 2.3 * electron_charge;
% Boltzmann constant
```

```
18 kb = 1.38064852 .* 10 .^ -23;
19
20 %% Parameters
21 % Dimension in x axis, Lx
22 Lx = 5 * 10 ^ -9;
23 % Energy step, E_step, the smaller step, the preciser result
24 E_step = h_bar ^ 2 * pi ^ 2 ./ (2 * electron_mass * Lx ^ 2);
25 % Plasmon dephasing time, tao
26 tao = 10 * 10 ^ -15;
27 % System temperature, T
28 Tl = 300;
29
30 %%
31 % possible energy of initial and final states, E_i and E_f
32 Energy = linspace(0, 5.5 + 2.3 * 2, (5.5 + 2 * 2.3) / 0.01 +1) *
      electron_charge;
33 E_i = Energy;
34 E_f = Energy;
35 %%
36 % generation rate for initial states
37 Gamma_i = zeros(length(E_i), 1);
38 % generation rate for final states
39 Gamma_f = zeros(length(E_f), 1);
40
41 %% Calculation
42 for index_f = 1:length(E_f)
43     for index_i = 1:length(E_i)
```

```
44          E_yz = linspace(E_step, E_i(index_i) - E_step, (E_i(
               index_i) - 2 * E_step) / E_step + 1);
45          for index = 1:length(E_yz)
46              n_xi = floor(((E_i(index_i) - E_yz(index)) ./ E_step)
                    .^ 0.5);
47              n_xf = floor(((E_f(index_f) - E_yz(index)) ./ E_step)
                    .^ 0.5);
48              F_fl = (exp((E_f(index_f) - E_Fermi) ./ (kb .* Tl)) +
                    1) .^ -1;
49              F_il = (exp((E_i(index_i) - E_Fermi) ./ (kb .* Tl)) +
                    1) .^ -1;
50              % selection rule is that the change of nx must be odd
                    number
51              if mod(abs(n_xi - n_xf), 2) ~= 0
52                  M = n_xi * Lx ./ (n_xf .^ 2 - n_xi .^ 2) .* ((1 -
                        cos(pi * (n_xf + n_xi))) ./ (n_xf + n_xi) +
                       (1 - cos(pi * (n_xf - n_xi))) ./ (n_xf - n_xi)
                       );
53                  Gamma_l = 4 ./ tao .* (F_il) .* (1 - F_fl) .* ((M
                        .^ 2) ./ ((E_photon - E_step .* (n_xf .^ 2 -
                       n_xi .^ 2)) .^ 2 + h_bar ^ 2 * tao ^ -2) + (M
                       .^ 2) ./ ((E_photon + E_step .* (n_xf .^ 2 -
                       n_xi .^ 2)) .^ 2 + h_bar ^ 2 * tao ^ -2));
54                  Gamma_i(index_i) = Gamma_i(index_i) - Gamma_l;
55                  Gamma_f(index_f) = Gamma_f(index_f) + Gamma_l;
56              end
57          end
```

```
    end
end
%% plot energy distribution of non-thermal carriers
figure
hot_energy = Energy;
hot_gamma = Gamma_i + Gamma_f;
plot((hot_energy - E_Fermi) / electron_charge, hot_gamma / max(
    hot_gamma))
grid on
set(gcf, 'Units', 'Inches', 'Position', [0, 0, 4, 3])
set(gca,'FontSize',16)
set(gca,'FontWeight','bold')
set(gca,'XMinorTick','on')
set(gca,'YMinorTick','on')
set(gca,'TickLength',[0.08, 0.12])
xlabel('$E-E_F$ ($eV$)', 'Interpreter', 'Latex', 'FontWeight', '
    bold')
ylabel('$\Gamma$ (a.u.)', 'Interpreter', 'Latex', 'FontWeight', '
    bold')
box on
```

Anti-Stokes Raman spectrum generated using two-temperature model

In order to fit an Anti-Stokes Raman spectrum, we use MATLAB curve fitting tool. Simply type 'cftool' in MATLAB command line to activate it. To use curve fitting tool, we first need to create a function which receives input (Raman shift, lattice temperature, sub-population of hot carriers, electronic temperature and scaling factor) and output the Raman spectrum.

The function we created for Anti-Stokes Raman spectra is shown below:

```
function y = Raman_fit_TTM(x, a, b, c, d)
    %% Contributor: Shengxiang Wu

    %% Input variables
    % x is only for raman shift on anti-Stokes side
    % a is lattice temperature Tl
    % b is hot carrier population, chi
    % c is the electronic temperature, Te
    % d is scaling factor

    %% define physical constant
    % reduced planck constant, h_bar
    h_bar = 1.0546 .* 10 .^ -34;
    % speed of light, c_light
    c_light = 299792458;
    % Boltzmann constant, kb
    kb = 1.3807 .* 10 .^ -23;

    %% parameters input
    Tl = a;
    chi = b;
    Te = c;
    D = d;

    %%
    raman_energy = - x .* 100 .* c_light .* h_bar .* 2 .* pi;
    y = 1e4 .* D .* (chi .* (exp(raman_energy ./ (kb .* Te)) +1)
```

```
        .^ -1 + (1 - chi) .* (exp(raman_energy ./ (kb .* Tl)) - 1)
         .^ -1);
end
```

An example of using this function is shown in Figure C.3 with the MATLAB code to generate it.

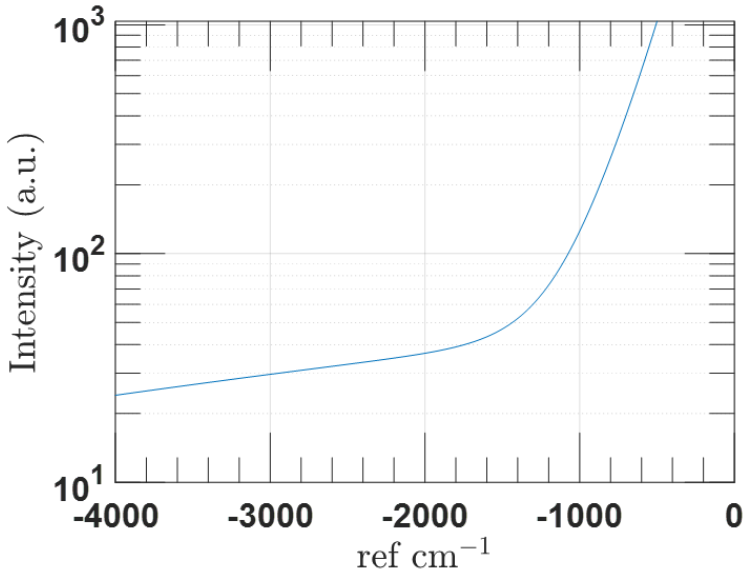

Figure C.3: Anti-Stokes Raman spectrum. $T_\mathrm{l} = 300$ K, $\chi = 1\%$, $T_\mathrm{e} = 5000$ K.

```
%% This script is used to plot an Anti-Stokes Raman using TTM
   parameters
% Contributor: Shengxiang Wu

%% Clear workspace and close current figures
clear all
close all
```

```
7
8  %% set Raman shift, from -4000 cm-1 to -500 cm-1
9  Raman_shift = linspace(-4000, -500, 3501);
10
11 %% Calculate Raman intensity assuming Tl = 300 K, chi = 0.01, Te
       = 5000 K
12 Tl = 300;
13 chi = 0.01;
14 Te = 5000;
15 Raman_intensity = Raman_fit_TTM(Raman_shift, Tl, chi, Te, 1);
16
17 % Plot Raman spectrum
18 plot(Raman_shift, Raman_intensity)
19 grid on
20 set(gcf, 'Units', 'Inches', 'Position', [0, 0, 8, 6])
21 set(gca,'FontSize',24, 'FontWeight','bold')
22 xlabel('ref $\mathrm{cm^{-1}}$', 'Interpreter', 'Latex', '
       FontWeight', 'bold')
23 ylabel('Intensity (a.u.)', 'Interpreter', 'Latex', 'FontWeight',
       'bold')
24 set(gca,'XMinorTick','on')
25 set(gca,'YMinorTick','on')
26 set(gca,'TickLength',[0.08, 0.12])
27 set(gca, 'YScale', 'log')
```

Full range Raman spectrum generated using eq 3.5b

Similarly, in order to fit the full range Raman spectrum, we first create a function based on eq 3.5b. The function is shown below:

```
function y = Raman_fit_full_range(x, a, b, c, d, e)
    %% Contributor: Shengxiang Wu

    %% Input variables
    % x: Raman shift
    % a: lattice temperature
    % b: chi, subpopulation of hot carriers
    % c: electronic temperature
    % d: scaling factor
    % e: Plasmon dephasing time, in fs

    %% define physical constants
    % electron charge
    electron_charge = 1.6022 .* 10 .^ -19;
    % reduced planck constant, h_bar
    h_bar = 1.0546 .* 10 .^ -34;
    % speed of light, c_light
    c_light = 299792458;
    % Boltzmann constant, kb
    kb = 1.3807 .* 10 .^ -23;

    %% parameters input
    Tl = a;
    chi = b;
    Te = c;
    D = d;
    tao_fit = e * 10 ^ -15;
```

```
28
29      %% Calculation
30      % convert Raman shift to energy
31      Energy = x .* c_light .* h_bar .* 2 .* pi .* 100;
32      % inelastic scattered energy
33      delta_E = linspace(-5, 5, 5001) .* electron_charge;
34      % joint density of states, Raman signal is proportional to
           joint
35      % density of states
36      j_DOS = zeros(length(Energy), 1);
37      for index = 1:length(Energy)
38          Fermi_i = (1 - chi) .* (exp(delta_E ./ (kb .* Tl)) + 1)
               .^ -1 + chi .* (exp(delta_E ./ (kb .* Te)) + 1) .^ -1;
39          Loren_i_pre = tao_fit ^ -1 .* (delta_E .^ 2 + (tao_fit ^
               -1 * h_bar) ^ 2) .^ -1;
40          % Normalization, you can choose dont do normalization,
               only affect
41          % the scaling factor
42          Loren_i = Loren_i_pre ./ max(Loren_i_pre);
43          Fermi_f = (1 - chi) .* (exp((delta_E + Energy(index)) ./
               (kb .* Tl)) + 1) .^ -1 + chi .* (exp((delta_E + Energy
               (index)) ./ (kb .* Te)) + 1) .^ -1;
44          Loren_f_pre = tao_fit ^ -1 .* ((delta_E + Energy(index))
               .^ 2 + (tao_fit ^ -1 * h_bar) ^ 2) .^ -1;
45          Loren_f = Loren_f_pre ./ max(Loren_f_pre);
46          myfun = Fermi_i .* Loren_i .* (1 - Fermi_f) .* Loren_f;
47          j_DOS(index) = trapz(delta_E, myfun);
```

```
48      end
49      % 1e24 is arbitray, just to make the scaling factor not crazy
            big
50      y = 1e24 .* D .* j_DOS;
51  end
```

For instance, Figure C.4 shows the calculated Raman spectrum assuming $T_\mathrm{l} = 300$ K, $\chi = 1\%$, $T_\mathrm{e} = 5000$ K and $\tau = 10$ fs.

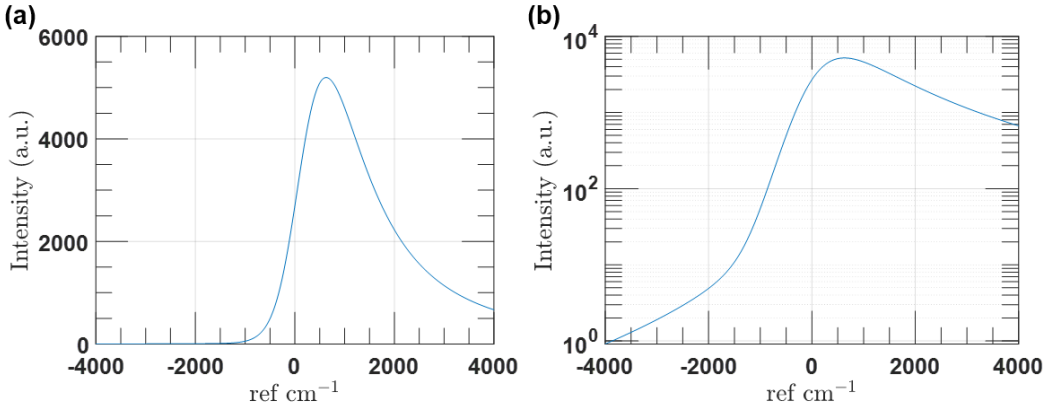

Figure C.4: Anti-Stokes Raman spectrum. $T_\mathrm{l} = 300$ K, $\chi = 1\%$, $T_\mathrm{e} = 5000$ K and $\tau = 10$ fs.

The code to generate Figure C.4 is shown below:

```
1  %% This script is used to plot a Raman spectrum using eq 3.5
2  % Contributor: Shengxiang Wu
3
4  %% Clear workspace and close current figures
5  clear all
6  close all
7
```

```
%% set Raman shift, from -4000 cm-1 to -500 cm-1
Raman_shift = linspace(-4000, 4000, 8001);

%% Calculate Raman intensity assuming Tl = 300 K, chi = 0.01, Te
   = 5000 K, and plasmon dephasing time of 10 fs
Tl = 300;
chi = 0.01;
Te = 5000;
tau = 10;
Raman_intensity = Raman_fit_full_range(Raman_shift, Tl, chi, Te,
   1, tau);

% Plot Raman spectrum
plot(Raman_shift, Raman_intensity)
grid on
set(gcf, 'Units', 'Inches', 'Position', [0, 0, 8, 6])
set(gca,'FontSize',24, 'FontWeight','bold')
xlabel('ref $\mathrm{cm^{-1}}$', 'Interpreter', 'Latex', '
   FontWeight', 'bold')
ylabel('Intensity (a.u.)', 'Interpreter', 'Latex', 'FontWeight',
   'bold')
set(gca,'XMinorTick','on')
set(gca,'YMinorTick','on')
set(gca,'TickLength',[0.08, 0.12])
```